

Study of the ${}^6\text{Li} + \alpha$ resonant reaction in inverse kinematics using ACTAR TPC

Jannes DAEMEN

Promotor: Prof. Dr. R. Raabe
Begeleider: F. Renzi

Proefschrift ingediend tot het
 behalen van de graad van
 Master of Science in de Fysica

Academiejaar 2015-2016

Contents

1	Nuclear cluster physics and physics case	1
1.1	The basics of nuclear physics	1
1.1.1	The nuclear shell model	3
1.1.2	The shell model for deformed nuclei	5
1.1.3	Experimental observables in nuclear physics	7
1.2	Clustering in nuclei	11
1.2.1	Basics of cluster formation	11
1.2.2	Mean field theories	16
1.2.3	Advanced theories	20
1.3	The cluster structure of ^{10}B	24
1.3.1	Theoretical studies of ^{10}B	25
1.3.2	Rotational band structure of ^{10}B	27
1.3.3	Experimental proposal	28
2	Experimental setup	31
2.1	The ALTO facility	31
2.1.1	The Bacchus spectrometer	31
2.2	The ^6Li beam	32
2.3	The ACTAR TPC demonstrator	34
2.3.1	Generalities	34
2.3.2	The gas medium	36
2.3.3	The auxiliary detectors	38
2.3.4	MICROMEGAS	40
2.3.5	Calibration source	41
2.4	GET electronics	41
3	Nuclear reaction theory	44
3.1	Terminology	44
3.2	Basic formalisms	47
3.2.1	Nuclear scattering theory	47
3.2.2	Resonances of the compound nucleus	51
3.3	Kinematics of nuclear reactions	55
3.3.1	Two-body kinematics	55
3.3.2	The Kinematics of the $^6\text{Li} + \alpha$ reaction	58

4 Data analysis	62
4.1 Calibration of the detector components	62
4.1.1 The DSSDs	62
4.1.2 The Maya detectors	64
4.1.3 Alignment of the padplane	64
4.2 Treatment of the particle tracks	66
4.2.1 Fitting of the tracks	66
4.2.2 Determination of the vertex position	68
4.3 Particle identification	70
4.3.1 The DSSDs	71
4.3.2 The Maya detectors	73
4.4 Reconstruction of the kinematics	74
4.5 Excitation spectrum of ${}^6\text{Li}$	77
4.5.1 The 11.5 MeV beam energy	77
4.5.2 The 16.5 MeV beam energy	80
4.6 The excitation spectrum of ${}^{10}\text{B}$	81
4.6.1 The 11.5 MeV beam energy	82
4.6.2 The 16.5 MeV beam energy	85
5 Conclusion	89
A Spectra of the other beam energies	91
A.1 The ${}^6\text{Li}$ excitation spectra	91
A.2 The ${}^{10}\text{B}$ excitation spectra	93

Chapter 1

Nuclear cluster physics and physics case

1.1 The basics of nuclear physics

The goal of physics as a scientific domain is to study the laws of nature. Various sub-domains exist which specialize themselves in one specific part of nature. One of these subdomains is Nuclear physics. Nuclear physics studies the core of the atom. This core is called the *nucleus*. The nucleus of an atom consists of one or more smaller constituents, the *nucleons*. Two species exist, the *proton* and the *neutron*. The main difference between these species is their charge. The protons are positively charged, whereas the neutrons have no charge. Typically the nucleus is symbolically represented as ${}_N^AX_Z$. In this notation X denotes a specific atom species, Z and N the amount of protons and neutrons of which the nucleus is composed respectively and $A = Z + N$ the atomic number. Often, only A is indicated as the amount of protons is the same for each type of atom. The atom has to be electrically neutral, so Z simply equals the amount of electrons of the atom. The amount of neutrons can vary however and nuclei with the same Z but different N values are called *isotopes*.

There are four fundamental forces present in nature. These are the *gravitational*, *electromagnetic*, *weak* and *strong force*. Due to the electromagnetic force, the protons tend to repel each other because they are identically positively charged. It is the strong force which saves the nucleus from simply falling apart. This force only becomes relevant at the femtometer ($1 \text{ fm} = 10^{-15} \text{ m}$) scale. At these distances, the interaction between the nucleons becomes strongly attractive and dominates the repulsive electromagnetic force. At even shorter distances, the strong force also becomes repulsive. This way, the size of the nucleus is typically of the order of a few femtometers. Such a potential also implies that the volume of the nucleus and its binding energy (see section 1.1.3) are roughly proportional to the number of nucleons. This property is also known as the *saturation property* of the nuclear force. Note that such a property is also present in atomic physics. In a diatomic molecule, bonds are formed by exchanging electrons between the two atoms. The force which binds the atoms together is therefore called an *exchange force*. If one would try to push the atoms closer to each other, an strongly repulsive force would be experienced due to the overlap of filled electron orbitals. This similarity is one of the reasons why the nuclear force can also be interpreted as being an exchange force.

In the formation of the nucleus, the neutrons are needed so that the net force becomes

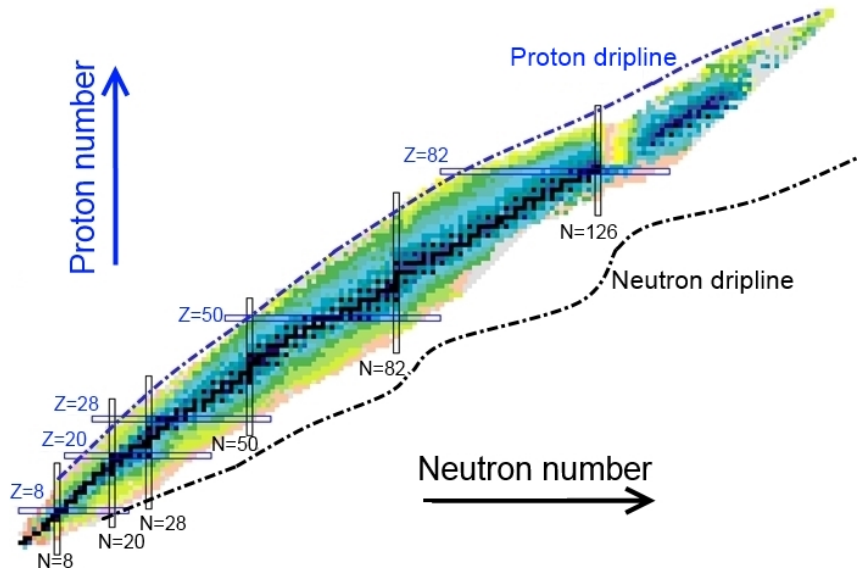


Figure 1.1: The nuclear chart. The magic numbers are indicated (see Section 1.1.1). The proton and neutron driplines are also indicated.

sufficiently attractive. For this reason, the amount of neutrons tends increase as the nucleus becomes heavier.

Similar to the table of Mendeleev in the case of atoms, the (known) nuclei are collected in what is called the *nuclear chart*. The chart can be seen in Figure 1.1. In the vertical direction the proton number increases, in the horizontal direction the neutron number increases. By now about 3000 nuclei are known to exist [1]. They have either been found in nature or have at some point been synthesized in the lab. Via theoretical models, it has been predicted that there should exist about 7000 bound nuclei. The black squares indicate the non-radioactive, *stable* nuclei. Of the known nuclei, only 288 are stable and together, they form the *valley of stability* along the nuclear chart [1]. All other nuclei are *unstable*. Nuclei found far from the valley of stability can be classified generally as *exotic* nuclei. These nuclei will decay so that a energetically more favorable nucleus is formed. This can happen multiple times, until the valley of stability is reached. Various decay mechanisms exist such as α decay in which an α particle¹ and β decay², electron capture, etc [2]. The decay of a nucleus is characterized by a specific *lifetime*. This is the time after which one can expect the nucleus to be decayed. On Figure 1.1, the proton and neutron *driplines* are also indicated. These lines indicate the boundary up to which the nuclei can be considered to be bound systems. This means that if an extra proton or neutron was to be added (for each dripline respectively), this nucleon would immediately be reemitted.

¹The α particle is another name for the most common isotope of Helium, namely ${}^4\text{He}$.

² β decay is governed by the weak force. In this type of decay an electron or positron is emitted (the β^\mp particle). In order to have charge conservation, a neutron is converted to a proton in case of β^- decay and vice versa in case of β^+ decay.

1.1.1 The nuclear shell model

The nucleus is a quantum mechanical system of many particles. In quantum mechanics, systems are represented by their wavefunction Φ . This wavefunction contains most of the physical properties of the system. In order calculate this wavefunction, one has to solve the Schrödinger equation $H\Phi = E\Phi$ where E is the eigenvalue related to Φ and has the interpretation of the energy of the system. H is the Hamiltonian of the nuclear system with A nucleons. In the non-relativistic case the Hamiltonian is given by [3]

$$H = \sum_{i=1}^A \frac{\mathbf{p}_i^2}{2m_i} + \sum_{i>j=1}^A V_{ij}(\mathbf{r}_i - \mathbf{r}_j) \quad (1.1)$$

where \mathbf{p}_i and m_i are the momentum operator and mass for the i th nucleon such that the first set of terms has the interpretation of the kinetic energy. V_{ij} represents the interaction between nucleon i and j on position \mathbf{r}_i and \mathbf{r}_j . Higher order contributions such as a three-body force can improve the description of this Hamiltonian [4]. Unfortunately, no complete theoretical description exist to fully explain the interaction terms V_{ij} . Hence, it is not possible to actually calculate Φ and E . In a simplified approach to the problem, one can assume that all nucleons do not interact and simply move in a potential which is due to all other nucleons. This type of potential is called a *mean field potential*. The Hamiltonian can be rewritten as follows [3]

$$H = \sum_{i=1}^A \left[\frac{\mathbf{p}_i^2}{2m_i} + U_i(\mathbf{r}) \right] + \sum_{i>j=1}^A V_{ij}(\mathbf{r}_i - \mathbf{r}_j) - \sum_{i=1}^A U_i(\mathbf{r}) = H_0 + H_{res}, \quad (1.2)$$

where $H_0 = \sum_{i=1}^A \left[\frac{\mathbf{p}_i^2}{2m_i} + U_i(\mathbf{r}) \right]$ is the mean field Hamiltonian and $U(\mathbf{r})$ the mean field potential. H_{res} can be considered as a correction. It is evident that as long this correction is small, the mean field approximation is adequate. In what follows H_{res} will be neglected.

This leaves to find an appropriate form for the mean field potential. One of the most successful models for this is due to Goeppert-Mayer, Wigner, Jensen en Haxel and is called the *nuclear shell model* [5, 6]. In fact, the model is based on ideas originating from atomic physics. In atomic physics one models the electrons as if they move in fixed atomic orbitals. This is often referred to as the *atomic shell model*. The nuclear shell model starts from the same general idea. The difference is that in this model the nucleons move in fixed orbitals. In this framework the mean field potential becomes [7]

$$U(\mathbf{r}) = \frac{m\omega^2 \mathbf{r}^2}{2} + D(\mathbf{l}^2 - \langle N | \mathbf{l}^2 | N \rangle) + C\mathbf{l} \cdot \mathbf{s}. \quad (1.3)$$

The first term represents the harmonic oscillator potential where ω is the angular frequency of the oscillator and is directly related to the the energy levels of the harmonic oscillator³. The second term provides a correction to this potential related to the orbital angular momentum \mathbf{l} of the nucleon. D is a constant which differs for each nucleus, but tends to become larger for heavier systems. $\langle N | \mathbf{l}^2 | N \rangle$ represents an averaging with respect to the N th shell of the harmonic oscillator⁴. The third term is called the spin-orbit

³Similar to what was presented above the Schrödinger equation $H\psi = E\psi$ can be solved to find the wavefunctions ψ_n and energy levels E_n . The energy levels are then given by $E_n = \hbar\omega(n + 3/2)$ [8]

⁴This correction can be left out, but then different parameters for each shell are needed. Using the same parameters for each shell results in a general decompression of the level scheme [7, 9].

coupling and is interpreted as an interaction between the orbital and spin angular momenta \mathbf{l} and \mathbf{s} of the nucleon. C is once again a constant and characterizes the strength of the interaction. Note that an additional Coulomb potential has to be introduced in Equation (1.3) in the case of protons to take into account its charge.

Now the Schrödinger equation $H_0\Phi = E\Phi$ can be solved. A representation of the energy scheme resulting from such a calculation can be seen in Figure 1.2. The level scheme on the left is the result of a calculation in which only the harmonic oscillator term of Equation (1.3) is considered. The numbers in between the levels indicate how many nucleons can populate the levels up to that point if one was to fill the levels one by one, always considering the lowest energy levels. When spin is considered, the degeneracy of these levels is equal to $(n + 1)(n + 2)$. The middle scheme introduces the orbital angular momentum term $\sim \mathbf{l}^2$ and lifts the degeneracy to some degree. The last scheme introduces the spin orbit term. It can be seen that the spin-orbit contribution splits each level characterized by the angular momentum quantum number l into two new levels. These levels are characterized by a new quantum number j . This quantum number is related to the total angular momentum $\mathbf{j} = \mathbf{l} + \mathbf{s}$. Most often the spectroscopic notation Nl_j is used to label the levels⁵. Each of these levels is still degenerate by $2j + 1$. As can be seen on the right part of the figure, the level scheme is reordered in such a way that one can distinguish energy gaps. Similar as in the atomic shell model, these gaps can be interpreted as major shell closures. There are shell closures if N or Z are equal to 2, 8, 20, 28, 50, 82, 128, ... These numbers are also referred to as the *magic numbers* [2]. Several experiments have shown that additional stability is gained for nuclei for which N or Z is equal to a magic number. Evidence of this can for example be found in an increase of the two-neutron and proton energies [2]. The nucleus is doubly magic if both N and Z are equal to a magic number. Note however that it has been shown that these magic numbers might only hold for nuclei close to the valley of stability. For nuclei far from stability, additional effects such as the tensor component of the nuclear force shift the orbitals such that new magic numbers are produced [10]. These additional components are included in H_{res} from Equation (1.1) [3]. An example of a nucleus which shows this behavior is ⁵⁴Ca. This nucleus has an additional magic number which is 34 [11].

As a last remark it must be stated that while the mean field proposed in Equation (1.3) provides a basic understanding of some of the observed nuclear properties, the use of a harmonic oscillator is not the most accurate one. Another commonly used mean field potential is the Woods-Saxon potential. This potential is given by [9]

$$U(r)_{WS} = V(r) + V_{LS}, \quad (1.4)$$

where

$$V(r) = -\frac{V_0}{1 + \exp[(r - R)/a]} \text{ and } V_{LS} \propto \frac{1}{r} \frac{\partial V_{SO}(r)}{\partial r} \mathbf{l} \cdot \mathbf{s}. \quad (1.5)$$

V_0 , R and a can be interpreted as the potential depth, nuclear radius and diffuseness depth respectively. V_{SO} is a function and is often chosen to be equal to $V(r)$. Note that this time the term proportional to \mathbf{l}^2 is absent. The effect of this term is nicely reproduced by $V(r)$.

⁵In this notation the letters s, p, d, f, \dots are used for $l = 0, l = 1, l = 2, l = 3, \dots$ respectively. j is given by $l \pm \frac{1}{2}$.

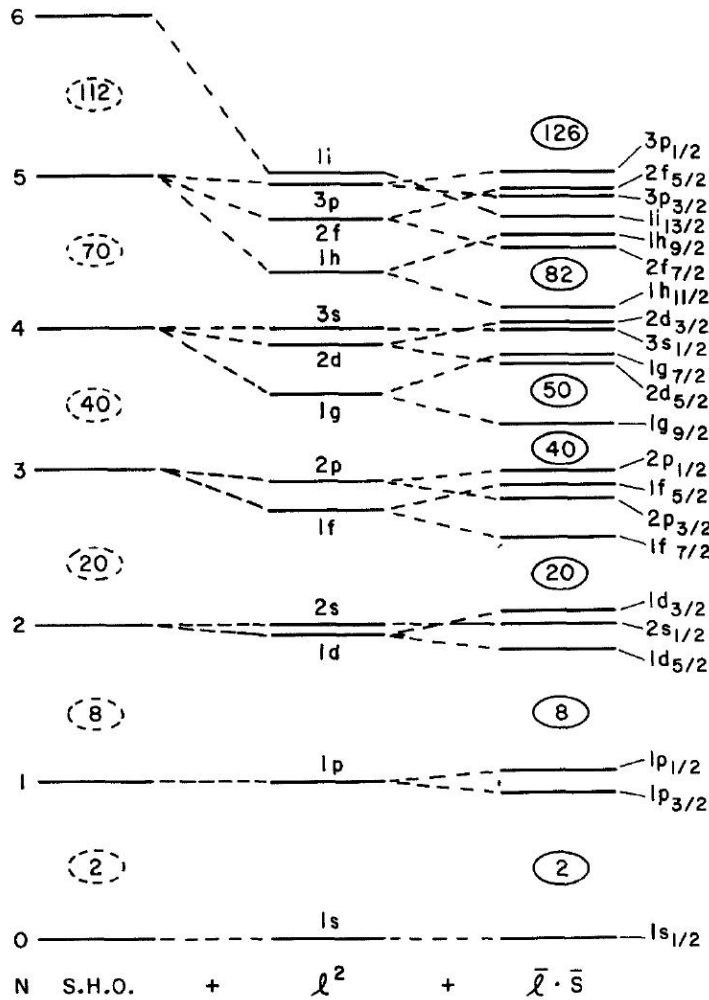


Figure 1.2: Representation of the orbitals of the nuclear shell model. If a simple harmonic oscillator (S.H.O.) is considered, one finds the left energy scheme with equal spaced energy gaps. The middle scheme results when one also considers the ℓ^2 term due to the angular momentum of the nucleons. The right scheme incorporates a spin-orbit coupling term $\sim \mathbf{l} \cdot \mathbf{s}$. This last scheme reproduces the correct magic numbers. Figure adapted from Reference [12].

1.1.2 The shell model for deformed nuclei

Often nuclei are pictured as spheres where in which the nucleons are closely packed together. In the laboratory frame this is true. In this frame, the nucleus exhibits macroscopic motions such as translation and rotation. It is in this frame the nuclear shell model is considered. To gain more physical insight however, it can be useful to describe nuclei in their intrinsic frame of reference [13]. In this frame, the there is a breaking of the rotational symmetry and the rotational quantum number j of the nucleons is no longer a good quantum number. Practically this means that in some cases, a deformation of the nucleus becomes apparent [2].

To describe this deformation, one has to adapt the potential of Equation (1.3) to allow for such a deformation. This was first done by Nilsson [14]. In carthesian coordinates,

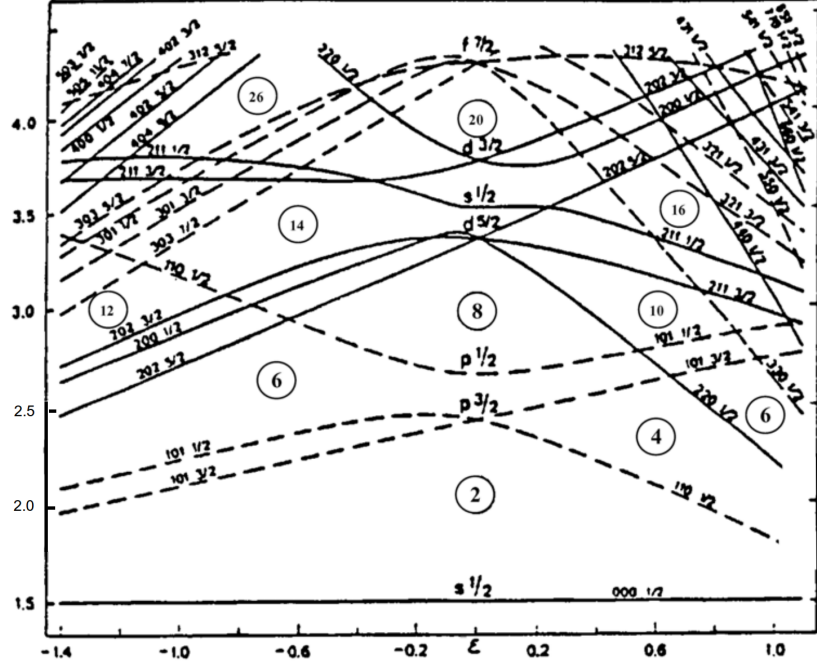


Figure 1.3: Example of the level scheme for deformed nuclei. It can be seen that the energy levels change as a function of β . Full lines indicate states with positive parity, dashed line indicate states with negative parity. The circles indicate the predicted magic numbers. The Nilsson quantum numbers $Nn_z\Lambda\Omega$ are also indicated. Adapted from [15].

one has [7]

$$U(x, y, z) = \frac{m}{2}[\omega_{\perp}^2(x^2 + y^2) + \omega_z^2 z^2] + D\mathbf{l}^2 + C\mathbf{l} \cdot \mathbf{s}, \quad (1.6)$$

where

$$\omega_{\perp}^2 = \omega_0^2 \left(1 + \left(\frac{4\pi}{5}\right)^{-\frac{1}{2}} \beta\right) \quad (1.7a)$$

and

$$\omega_z^2 = \omega_0^2 \left(1 - 2\left(\frac{4\pi}{5}\right)^{-\frac{1}{2}} \beta\right). \quad (1.7b)$$

In these equations β is the deformation parameter and is defined as [2]

$$\beta = \frac{4}{3} \sqrt{\frac{\pi}{5}} \frac{\Delta R}{R_{av}}, \quad (1.8)$$

where ΔR is the difference of between the semimajor and semiminor axes of the ellipse one would get if one considers the cross sectional area of the nucleus. This choice originates from a spherical modeling of the nucleus and assuming that there is conservation of volume when the deformation starts [2]. The use of a new potential modifies the level scheme. An example of this can be seen in Figure 1.3.

Sometimes another parameter, ε , is used. ε is the elongation and is defined as [7, 9]

$$\varepsilon = 3\left(\frac{4\pi}{5}\right)^{-\frac{1}{2}} \beta. \quad (1.9)$$

From this it is also evident that $\varepsilon = (\omega_{\perp} - \omega_z)/\omega_0$. When $\varepsilon > 0$ the nucleus is said to be *prolate*, if $\varepsilon < 0$, the nucleus is *oblate*. A prolate nucleus can intuitively be pictured as if

it has been stretched from two opposite sides. This way a shape similar to that of a rugby ball is formed. Oblate nuclei can be pictured as if the nucleus has been squished together from two sides. This way, the nucleus has a shape similar to that of a disk. Recently, more exotic shapes of the nucleus have been observed. An example of this is the pear shaped nucleus ^{224}Ra [16].

The modification of the potential obviously has its impact on the single particle energy levels as shown in Figure 1.2. As an additional feature, there will be another lifting of the degeneracy and new quantum numbers to label these states must be used, Ω and Λ . Ω can approximately be interpreted as the projection of the angular momentum \mathbf{j} onto the symmetry axis. The same interpretation applies for Λ for the orbital angular momentum \mathbf{l} . However, as mentioned before, \mathbf{j} is no longer a good quantum number. In reality the wavefunction $\psi(\Omega)$ will be a linear combination of Nl_j states [2, 9]. In practice, states of the Nilsson scheme are labeled as $Nn_z\Lambda\Omega$.

1.1.3 Experimental observables in nuclear physics

Binding and separation energy of the nucleus

An important question in nuclear physics is which nuclei can exist and which ones are stable. Important parameters that determine this are the *binding* and *separation energies* of the nucleus. The nuclei can be bound systems due to the attractive part of the strong force. So when nucleons are brought together at the length scale where the strong force becomes attractive, there will be a minimization of the energy and the nucleus is formed. The binding energy is then exactly the amount of energy that is needed to compensate for the attractive potential and disassemble the nucleus into its separate nucleons. In most cases, adding an additional nucleon will increase the binding energy. For this reason, often the binding energy per nucleon is plotted in graphs instead. Such a plot is given in Figure 1.4. It can be seen that initially there is a steep rise in binding energy. At around $A = 55$, the binding energy per nucleon starts to decrease. The amount of binding energy per nucleon gives an idea of how stable a nucleus is. It should be noted however that while the binding energy does decrease at some point, this decrease is slow. So to a rough approximation, the binding energy can be considered to be constant in this region. As mentioned earlier, this can be explained via a potential which is attractive at short distances but repulsive at larger distances.

A simple model that describes this kind of graph is the *semi-empirical mass formula*. This formula allows to calculate the binding energy BE as follows:

$$BE = a_{vol}A - a_{surf}A^{2/3} - a_{Coul}Z(Z-1)A^{-1/3} - a_{asym}\frac{(N-Z)^2}{A} + a_{sym}. \quad (1.10)$$

In this equation a_{vol} , a_{surf} , a_{Coul} , a_{asym} are coefficients related to the volume, surface, Coulomb and asymmetry terms. a_{sym} is an additional parameter related to the pairing of nuclei. This parameter takes on the value $+\delta$, $-\delta$ or 0 in the case one has even-even (N and Z are even), odd-odd or odd-A nuclei respectively. The values of the coefficients and pairing parameter haven been found by fitting the equation to a graph such as in Figure 1.4. Further explanation on how to interpret the several terms in the formula can be found basic textbooks such as Reference [2].

Closely related to the binding energy is the separation energy. This can be defined for a single nucleon, for example the proton separation energy. In this case, the separation

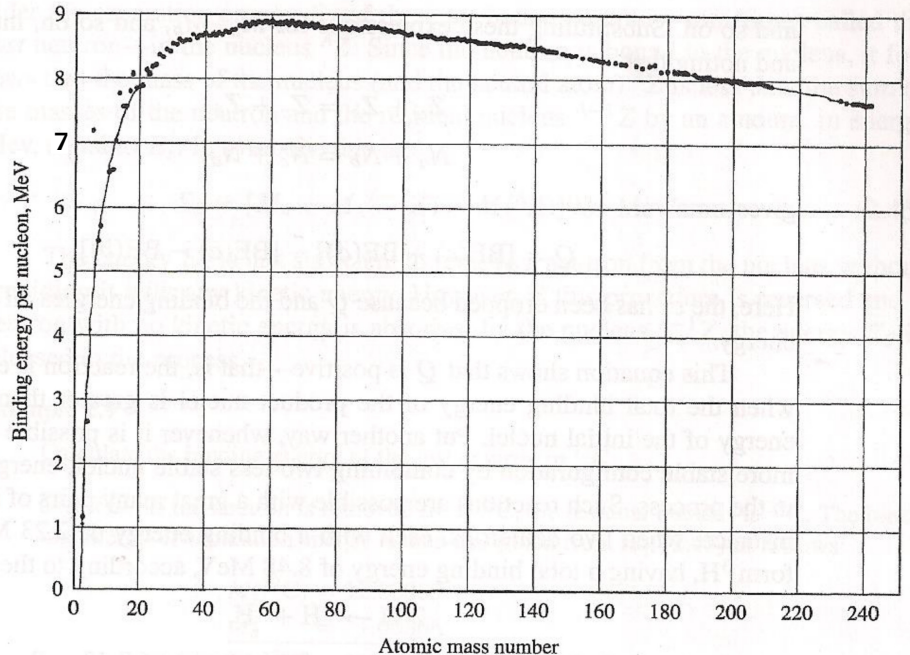


Figure 1.4: The binding energy per nucleon versus nucleon number A . Figure from Reference [17].

energy S_p is just the difference in binding energy between the nucleus with and without the proton, i.e.:

$$S_p = BE(^Z_A X_N) - BE(^{Z-1}_{A-1} X_N). \quad (1.11)$$

Similarly, this can be defined for the proton separation energy S_n . One can go even further with defining multiple particle separation energies such as the two-proton separation energy S_{2p} and the α particle separation energy S_α . These separation energies are defined in a similar way as S_p in Equation (1.11). Physically one can interpret these energies as follows. Suppose a nuclei is brought into an excited state (see also in the next paragraph) which has a higher energy than S_p . This means that there is enough energy in the system to make the least bound proton, unbound. Then, the proton will simply be emitted as a free particle. Similar reasonings apply to other particles and their separation energies.

Energy levels and rotational bands

The shell model discussed in Section 1.1.1 already showed to exhibit discrete energy levels for the nucleons. This property will carry on once the nucleus as a whole is considered. The lowest energy level is called the *ground state* of the nucleus. When the nucleus attains a higher energy state, the nucleus is said to be *excited*.

To each energy level one can assign a characteristic spin and parity, often written as I^π where I denotes the total angular momentum and π the parity. I is also called the nuclear spin. The parity is a quantity related to the orbital angular momentum l of the energy level and is defined as

$$\pi = (-1)^l, \quad (1.12)$$

such that π equals +1 if l is even and -1 if l is odd. The spin-parity assignments of the excitation levels can either be explained through a specific configuration of the nucleons

in the shells or via the collective motion of the nucleus.

In the former case, one should consider the nucleus as being composed of a fixed core with a closed shell configuration together with a set of valence particles and holes⁶. The nucleons in the core tend to pair up such that $j_{core} = 0$ [7]. This means that I is completely determined by adding up the angular momentum of the individual valence particles and holes⁷. For very high excitation states this picture is too simplistic and one must allow for the breakup of nucleon pairs such that more configurations become available. For nuclei which have a large deformation, the Nilsson model as presented in Section 1.1.2 must be considered. As explained, this model has its own set of angular momentum quantum numbers. Note also that the energies of each excited state is less well reproduced via the nuclear shell model. This is due to the residual interactions (see Equation (1.1)) between the valence nucleons. To get accurate results, these interactions must be treated appropriately. An introduction on how to do this can for example be found in Reference [3].

Two types of collective motion exist, rotations and vibrations of the nucleus. Only the former will be considered here, more information on the latter can be found in Reference [7]. Rotations will only be important when deformed nuclei are considered. An additional term is needed for the Hamiltonian [9]

$$H_{rot} = \frac{\mathbf{R}^2}{2\vartheta}, \quad (1.13)$$

where \mathbf{R} is the collective angular momentum and ϑ the moment of inertia. \mathbf{R} is parallel to the axis of rotation. In the case of pure collective rotation, there is no angular momentum contribution of nuclear origin. Then the nuclear spin $\mathbf{I} = \mathbf{R}$. It is then expected that for each integer⁸ value of $I = R$ a new state exist with an energy

$$E_I = \frac{\hbar^2}{2\vartheta} I(I + 1). \quad (1.14)$$

These states are build upon a state which does not exhibit any rotation. Together, this collection of states is called a *rotational band*. It is clear that measuring the energies of this band provides a value of ϑ . From its classical interpretation it is understood that ϑ gives an idea of the degree of deformation of the nucleus [2, 15].

In general, the nucleons can couple to a non-zero total spin \mathbf{j} . Then the nuclear spin of the rotational band states result from a couple between \mathbf{j} and \mathbf{R} such that $\mathbf{I} = \mathbf{j} + \mathbf{R}$. Remember however that in the case of a deformed nucleus, only the projection of \mathbf{j} , namely Ω is a good quantum number. Then by taking the z -axis as the symmetry axis of the axially symmetric nucleus and assuming that \mathbf{R} is perpendicular to this axis, Equation

⁶Holes are just the absence of nucleons in the core. There exists a symmetry between particles and holes such that holes can essentially be treated the same way.

⁷Note however that when multiple valence particles or holes occupy the same state, they can not have the same z-projection of j . This is due to the Pauli principle which states that fermions (nucleons are fermions) must have different quantum numbers within a system. For example, when two neutrons occupy a $f_{7/2}$ shell, their spin projections must for example be $\frac{7}{2}$ and $\frac{5}{2}$.

⁸An important exception is the case of even-even nuclei. These nuclei always have a groundstate with $I^\pi = 0^+$. Because of the symmetries in the system, only even integer values can exist [2].

(1.13) can be worked out to be

$$\begin{aligned} H_{rot} &= \frac{1}{2\vartheta}[(I_x - j_x)^2 + (I_y - j_y)^2] \\ &= \frac{1}{2\vartheta}[I^2 - I_z^2 + (j_x^2 + j_y^2) - (I_+j_- + I_-j_+)], \end{aligned} \quad (1.15)$$

where $I_{\pm} = I_x \pm iI_y$ (and similar for j_{\pm})⁹. The term proportional to $(I_+j_- + I_-j_+)$ is known as the Coriolis term. Once again, a new rotational state is formed for each integer value of R such that I takes on the values $|\Omega|, |\Omega|+1, |\Omega|+2, \dots$ ¹⁰. It can be shown that this leads to the following energy contributions

$$E_{I\Omega} = \frac{\hbar^2}{2\vartheta} \left[I(I+1) - \Omega^2 + \delta_{\Omega,1/2} a (-1)^{I+\frac{1}{2}} (I + \frac{1}{2}) \right], \quad (1.16)$$

where δ is a Krönicker delta and a is the decoupling parameter. a is different for each rotational band. Important here is due to the Krönicker delta, the Coriolis term is only present when $\Omega = \frac{1}{2}$. This is essentially due to the presence of the j_{\pm} operators when working out the matrix elements of H_{rot} which lead to the energies in Equation (1.16).

Decay widths

When the nucleus is found in an excited state, this is energetically not the most favorable situation. After some time, the nucleus will decay and in some cases it has multiple ways to do so. One way to do so is via the emission of a photon of appropriate energy. When the nucleus is found in an excited state which is higher in energy than the separation energy for nucleon or particle emission, the nucleus will also have the possibility to emit the particle for which the separation energy is reached. In such cases there will be a competition between the multiple types of decay.

Because the excited state has a lifetime, the state will also have a spread in its energy. This is due to Heisenberg's uncertainty principle. This principle states the following:

$$\Delta E \Delta t \geq \frac{\hbar}{2}, \quad (1.17)$$

such that if lifetime Δt becomes very small, the spread in the energy level ΔE becomes very large. When multiple types of decay are present, each of those will have its own lifetime, and hence its own width. These widths are called the *partial widths* Γ_i of the state where i denotes the possible decay modes. The total width Γ is then defined as

$$\Gamma = \sum_i \Gamma_i. \quad (1.18)$$

One can also find the relative probability of the decay processes. Suppose there are n possible types of decay, then the relative probability of the i th process is given by:

$$B_i = \frac{\Gamma_i}{\Gamma}. \quad (1.19)$$

These relative probabilities are called the *Branching ratios* of the decay modes.

⁹ I_{\pm} are known as ladder operators. When acting on a state $|I\rangle$ with angular momentum I , they raise(+) or lower(-) I by 1 unit. So $I_{\pm}|I\rangle = |I \pm 1\rangle$

¹⁰Note that $|\Omega|$ is used instead of Ω . This is because Ω and $-\Omega$ lead to degenerate states.

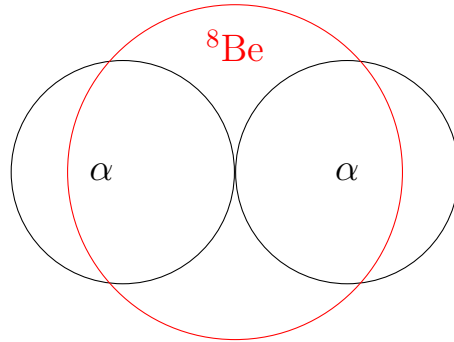


Figure 1.5: A schematic example of what the formation of α -clusters would mean in light nuclei. Here the example of ${}^8\text{Be}$ is used, which is indicated in red. The two α -clusters are indicated in black. From this schematic one can intuitively expect that the clustered configuration will induce a deformation of the nucleus.

1.2 Clustering in nuclei

As briefly mentioned in Section 1.1.2, some nuclei exhibit a specific kind of deformation under the form of *clustering*. This means that the nucleus precipitates into smaller sub-parts of several nucleons. The basic incentive for a nucleus to form cluster structures is the minimization of the energy of the system. This behavior is found in several areas of physics and it is thus not surprising that a similar mechanism exists in nuclear physics. The prediction of cluster formation is nevertheless a difficult problem as there is a complex interaction at play between the nucleons, governed by the strong force and additionally the Coulomb force in the case of protons.

1.2.1 Basics of cluster formation

It is known that the ${}^4\text{He}$ nucleus (α particle) is a strongly bound system. This can for example be seen from Figure 1.4 which shows that the binding energy per nucleon for ${}^4\text{He}$ is roughly 7 MeV. This is much higher than its neighboring nuclei. Moreover, the first excited state of ${}^4\text{He}$ has an energy of 20.21 MeV [18]. These two facts make the α particle a good candidate to be the basic constituents of the clusters. The high binding energy makes the formation of the clusters energetically more likely and the high excitation energy makes the particles rather inert. Because of this, the cluster nature of clustered states is easier maintained [15, 19]. A schematic, intuitive representation of how a nucleus could look like when clustering with α particles occurs can be seen in Figure 1.5 for a relatively light nucleus. For heavier systems, the α particles might arrange themselves into a configuration which resembles that of a crystal [15].

The idea of a nucleus which is composed of α particles has been reviewed by Hafstad and Teller [20]. In their treatment, models for three types of nuclei are considered, the $4n$ -type and the $4n \pm 1$ -type nuclei.

$4n$ -type nuclei

These nuclei consist of $2n$ neutrons and $2n$ protons which are considered to form n α particles. Furthermore, these nuclei are considered to be saturated. In such a model, the α particles will bind together into a larger nucleus via an α - α potential. This potential

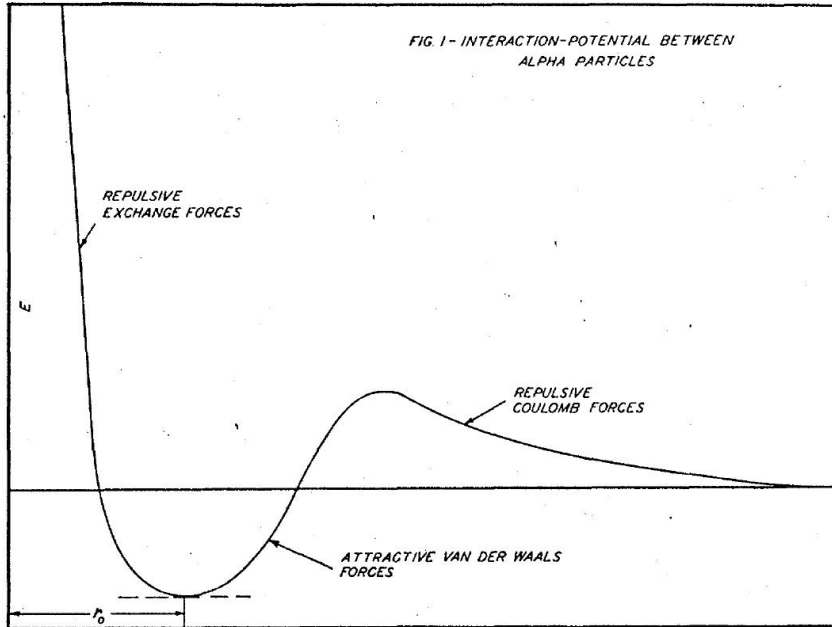


Figure 1.6: The proposed α - α potential by Hafstad and Teller [20].

can be seen in Figure 1.6 and is similar in form as the nuclear potential. The potential is repulsive at very short distances such the α particles stay separated. At somewhat larger distances the potential becomes attractive. Once more, this formation of such a potential can be interpreted as being due to an exchange force. Following this reasoning, one could say that bonds will be created between the α particle constituents. Each bond then corresponds to a certain amount of energy such that a linear relation can be found between the number of bonds and the total binding energy of the constituents. This model was compared with experiment for nuclei up to ^{32}S and showed quite good agreement for all nuclei except ^8Be and ^{20}N . According to the model, a 2α particle binding energy of 2.58 MeV is expected for ^8Be whereas experimentally it was determined that ^8Be is unbound by 0.0918 MeV[21].

An important question is whether a model in which the $4n$ nuclei are separated into n α particles is always applicable. It is for example known that the ground state of ^8Be possesses a clear cluster structure whereas the groundstate ^{16}O exhibits a structure which corresponds to a double closed shell[22]. An even more complex example is the ^{12}C nucleus for which the groundstates seems to behave as an admixture of the closed $p_{3/2}$ configuration and a triple α core, although the cluster structure is still strongly suppressed[23]. Of these three nuclei, only ^8Be is unbound for α particle emission. This fact has leads to the conclusion that the α particle lose their character as constituents if the nucleus is strongly bound and compact. Once the nucleus becomes less compact, i.e. the nucleus is less bound, the nucleons tend to cluster into α particles again. One can thus expect that only certain states will exhibit a cluster structure. Moreover, the lowest lying state with this behavior is expected to have an energy close the the *cluster decay threshold*. This threshold is equal to the binding energy gained (or lost if it is negative) when a nucleus is formed from several cluster components. For example, the cluster decay threshold for a nucleus which has a cluster structure of a heavy core and an α particle, is equal to the α particle separation energy S_α . This fact was first recognized

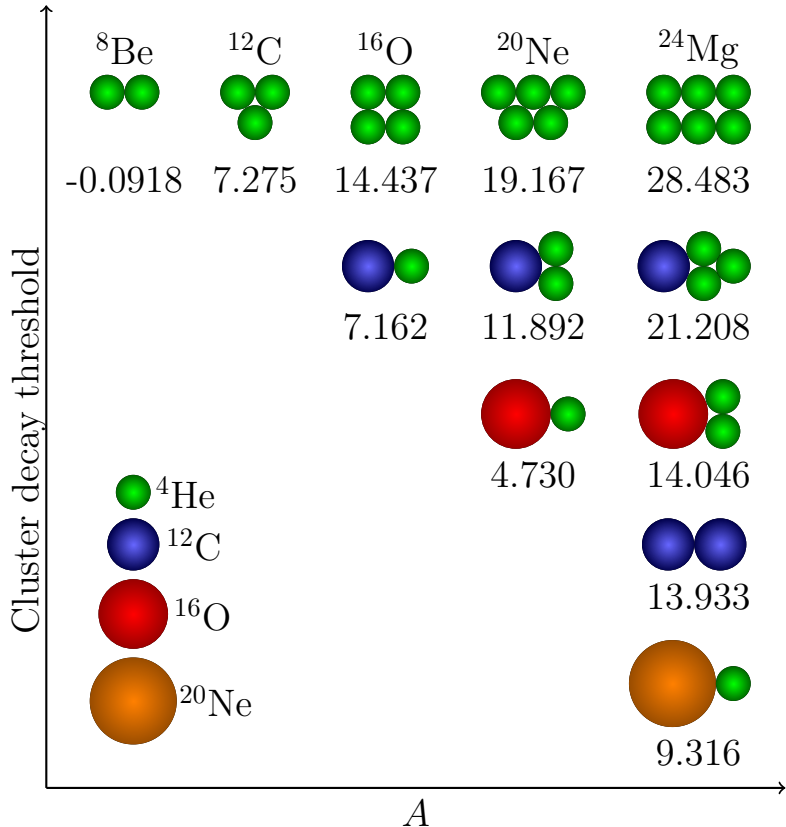


Figure 1.7: Example of an Ikeda diagram for $4n$ type nuclei up to ^{24}Mg . The numbers indicated below schematic cluster structures indicate the cluster decay threshold. The values are in MeV. Note that the configuration of the constituents should only be regarded as schematic. In reality the constituents might arrange themselves differently. The decay thresholds have been calculated from values found in References [21, 25–27].

by Ikeda *et al.*[24]. To get an idea at what energies cluster structures can be expected, this information is often summarized in an Ikeda diagram. An example of such a diagram for $4n$ -type nuclei up to $A = 24$ can be seen in Figure 1.7.

$4n + 1$ -type nuclei

The principles discussed in the previous paragraph can be extended to $4n + 1$ type nuclei. In the framework of clustering, these nuclei can be considered to be composed of $4n$ α particles and one additional nucleon. Hafstad and Teller also provided a first model to treat this type of nuclei [20]. An extension of this model will be discussed in Section 1.2.2.

The additional nucleon will provide a contribution to the binding energy via an interaction in which the neutron is exchanged between the α cores. For this reason this type of interaction is called an *exchange* interaction. When the additional nucleon is a proton, the Coulomb force must also be considered. The exchange interaction is analogous to what happens in covalent molecules. In this type of systems, the atoms can be considered as the cores of the system. The valence electrons reside in orbitals around the atoms. When these orbitals overlap, there is an exchange of the valence electrons between the atomic cores. Head-on overlaps are called σ -bonds and the overlap parallel orbitals are

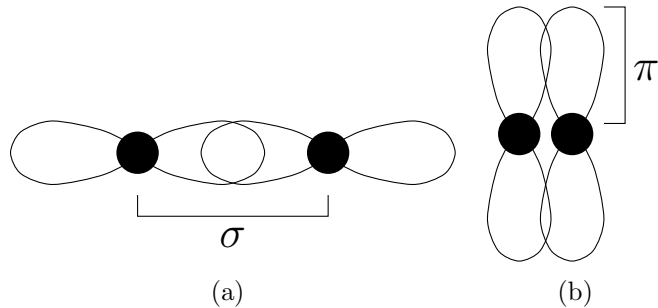


Figure 1.8: Schematic drawings of the formation of a (a) σ orbital and (b) π orbital . The α cores are indicated by the black dots. The valence nucleon is forced in between the α nuclei in the case of a σ orbital, whereas the nucleon is more likely to be found near the sides of the α nuclei in case of a π orbital.

called π -bonds. The latter type of bond is usually weaker. Through this analogy, the additional nucleon is also expected to reside in orbitals for which σ - or π -bonds are formed. Furthermore, the additional nucleons are referred to as valence nucleons and the cluster system as a whole as nuclear molecules. In the case of a σ -bond, the valence nucleon is expected to be found in between the two α cores. In the case of a π -bond, the nucleon is expected to be found next to the two cores. A schematic representation of the two types of bonds is given in Figure 1.8(b).

Similar as for the $4n$ type nuclei, the threshold energies of the cluster structures can be summarized in Ikeda diagram. An example of such an extended diagram for nuclei with A up to 27 can be seen in Figure 1.9. The threshold energies can be found in a similar way as before.

Gas-like clusters

Up to now it was assumed that the α particles and valence nucleons arrange themselves in crystalline or molecular configurations for $4n$ - and $4n + 1$ -type nuclei. While this picture is certainly valid for some nuclei, this does not have to be the case. Another possibility is a *gas-like* cluster structure [15, 30].

The classic example for this type of structure is the 0_2^+ Hoyle state¹¹ at 7.65 MeV [25]. Initially a chain-like structure was proposed by Morinaga [32]. There are problems with this interpretation however as the energy band structure that would correspond to such a deformation cannot be linked to any known experimental energy states. Moreover, the measured α decay width is larger than expected in such a configuration [30]. Microscopic calculations (see also Section 1.2.3) have been performed and one of the major results is that a large extension of the nuclear radius is predicted. This invites the interpretation of a dilute, gas-like configuration.

An important other effect comes into play in this type of configuration. α particles are in principle bosonic entities and the Pauli principle is not applicable. However, when the α particles are very close to one another, the internal fermionic degrees of freedom can not be neglected. This influences the occupation of the energy levels by the individual

¹¹This state is named after Fred Hoyle who proposed the existence of this state together with a clear 3α configuration to account for certain astrophysical processes [31].

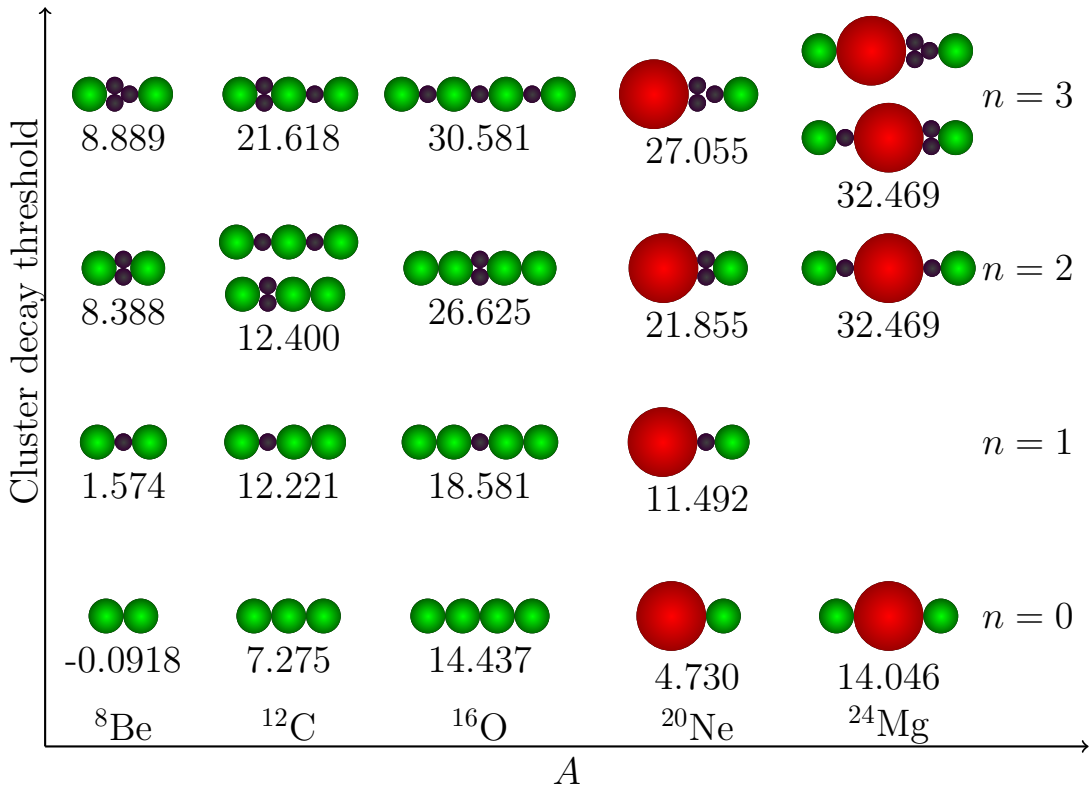


Figure 1.9: An example of an extended Ikeda diagram for some nuclei up to ^{27}Mg . The color scheme used is the same as in Figure 1.7. The neutrons are indicated in purple and the number of valence neutrons is indicated on the right. Once more, the configurations are only meant to be schematic and not necessarily realistic. Only the relative position of the neutron is important. Note that for some of these nuclei more configurations with different core nuclei are possible. The energies can be found or calculated from values from References [21, 25–27] and NNDC [28]. The figure is adapted from Reference [29].

nucleons. When a gas-like structure is present, the α particles are sufficiently separated such that fermionic degrees of freedom no longer play a role. This implies that the α particles can attain the lowest possible energy state in the mean field potential. Hence, the system resembles a Bose-Einstein condensate [15, 30].

The formation of the gas-like structure can be understood via the *Orthogonality Condition Model (OCM)* [33]. Essential to this model is that the wavefunction of an excited state should be orthogonal to the wavefunction of the groundstate. The results of such a modeling are most easily understood through the example of ^{12}C [30]. Through application of the orthogonality condition, it can be shown that the relative wavefunction for a 2α system has a small amplitude at small inter- α distances because the attractive interaction can not compensate for the kinetic contribution. This is consistent with the cluster model of ^8Be . However, once a third α particle is introduced, the interaction between the two initial α particles becomes stronger. This results in a larger amplitude at smaller distances and thus a more compact nucleus. This behavior corresponds to the ground state of ^{12}C . A representation of the α - α relative wavefunction can be seen in Figure 1.10. Now the Hoyle state must be considered. The orthogonality condition must be imposed and the result is a relative wavefunction which once more corresponds to a repulsion of

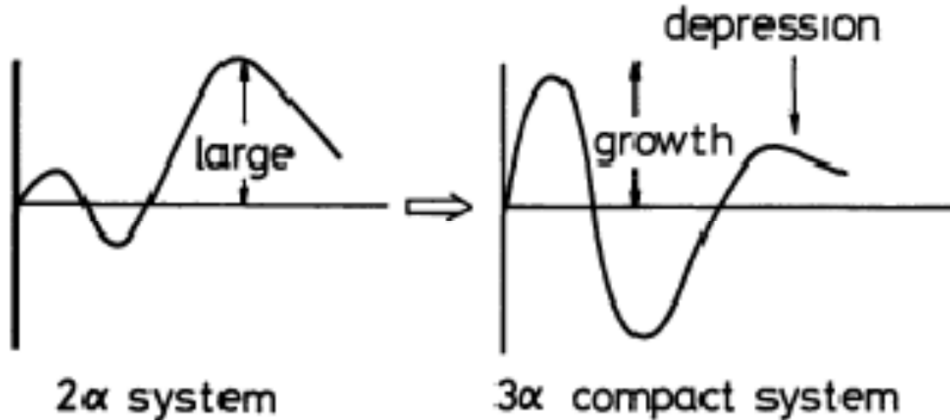


Figure 1.10: Representation of the α - α relative wavefunctions. The left figure corresponds to a 2α system, the right figure to a 3α system. From [30].

the two initial α particles. This way, one acquires a system in which all three α particles repel each other.

Recent developments have shown that systems other than those composed of $N\alpha$ particles might exhibit a similar gas-like structure. An example of this is ^{11}B , for which microscopic calculations suggest a $\alpha + \alpha + t$ gas-like structure. In order to make comparisons with ^{12}C , a quantity D can be introduced which is defined as [30, 34]

$$D = \frac{1}{A} \int_{\frac{\rho(r)}{\rho_0} < \frac{1}{5}} \rho(r) d^3r, \quad (1.20)$$

where A is the mass number, $\rho(r)$ is the density function and ρ_0 is a normal density which can be chosen to be 0.16 fm^{-3} . D can be interpreted as the fraction of nucleons which reside at locations where the nuclear density is lower than 20% of the normal density. Calculations of this D value for ^{12}C and ^{11}B for the groundstate and the 0_2^+ and $3/2_3^-$ excited states respectively give similar values. This suggests that if ^{12}C exhibits a gas-like structure, this is likely also the case for ^{11}B .

1.2.2 Mean field theories

It is tempting to try to explain cluster states from a mean field perspective just like what was done in the case of the nuclear shell model. To develop such a theory, one can start once more from a potential of the form of Equation (1.3). For simplicity, the terms proportional to \mathbf{l}^2 and $\mathbf{l} \cdot \mathbf{s}$ can be neglected. From intuition it is expected that the cluster states are deformed. Accordingly the potential can once more be adapted to the form of Equation (1.6), again neglecting the last two terms. The energy levels related to this state are given by

$$E_{deformed} = \frac{3}{2} \hbar \omega_0 + \hbar \omega_{\perp} (n_x + n_y) + \hbar \omega_z n_z, \quad (1.21)$$

where n_x , n_y and n_z are the quantum numbers labeling the state. A graphical representation of these energy levels as a function of the elongation ε can be seen in Figure 1.11. As ε increases, there is an initial lifting of the degeneracy. However, at some values of ε the degeneracy partially returns. This happens $\frac{\omega_{\perp}}{\omega_z}$ attains integer values. The magic

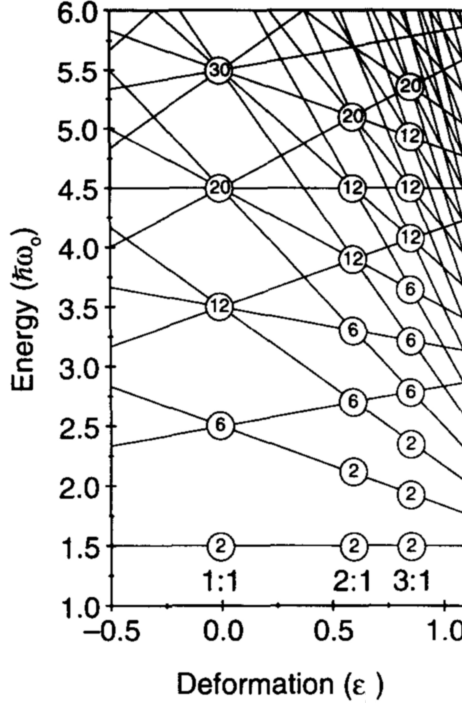


Figure 1.11: Energy levels of the deformed harmonic oscillator as a function of the deformation parameter ε . From [35].

numbers at these deformations are also indicated. It can be seen that these are exactly the ones of the simple harmonic oscillator, but each of them is repeated as many times the integer value of $\frac{\omega_{\perp}}{\omega_z}$. When the fraction is equal to 2, the *superdeformation* occurs, when the fraction is equal to 3, *hyperdeformation* occurs. These arguments suggest that there might be the possibility to describe the system with multiple harmonic oscillators¹² instead at these deformations [36], moreover, at these deformations the structure is especially stable [37]. A model which inherently uses multiple harmonic oscillators is the *2-center oscillator model* [38], which can be generalized having n centers.

The potential for this model is given by (the z -axis being the axis of symmetry) [7, 15, 38]

$$U(\mathbf{r}) = \frac{m}{2} (\omega_{x,i}^2 x^2 + \omega_{y,i}^2 y^2 + \omega_{z,i}^2 (z - z_i)^2 + C \mathbf{l}_i \cdot \mathbf{s} + D (\mathbf{l}_i^2 - \langle N | \mathbf{l}_i^2 | N \rangle)), \quad (1.22)$$

where $i = 1, 2$ such that it relates to one of the two centers. More specifically $i = 1$ when $z > 0$ and $i = 2$ when $z < 0$. z_i indicate the two centers. The resulting energy scheme for this potential for some of the lower lying levels can be seen in Figure 1.12. It is important to remark that for small displacements between the two center, the scheme resemble that of deformed nuclei (see Figure Nilsson). This provides another link between the harmonic oscillator description and the two-center formalism in which the α -cluster nature is explicit [35]. Via the Pauli principle some important other features of this model are revealed. As long as the separation is large enough and the potentials really can be seen as two distinct entities, the quantum numbers (n_x, n_y, n_z) of the simple harmonic oscillator can essentially be used. This changes once the potentials start to overlap. If

¹²If $\frac{\omega_{\perp}}{\omega_z} = n$, this would correspond to a combination of n SU(3) groups.

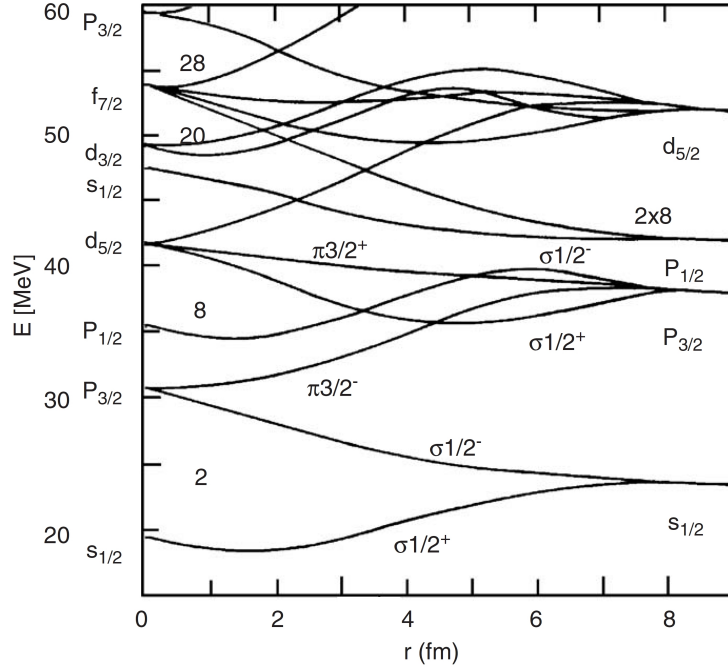


Figure 1.12: The energy levels from a two-centre potential calculation of two α particles. It is indicated which energy levels correspond to σ or π orbits. The energy levels can be filled with nucleons and the nucleons in non-filled levels will correspond to the valence nucleons present in nuclear molecules. The level in which they are found determines their orbits and thus the structure of the nuclear molecule. Adapted from [15].

the merging occurs with respect to the z -axis, n_z will become a function of the separation distance [35]. In general, when N oscillators fully merge, the state described by n_z will populate states with quantum numbers $Nn_z + (N - 1), Nn_z + (N - 2), \dots, Nn_z$. Reversing the reasoning, if there is information on what states are populated in the fused system, predictions can be made what states are populated in the separated harmonic potentials and hence which cluster structures might be present.

Assuming for a moment that the N center potential framework is valid, a combination of N harmonic oscillators can be proposed to describe a $N\text{-}\alpha$ system [35]. The N harmonic oscillator wavefunctions ψ_μ can be decomposed as follows:

$$\psi_\mu = \sum_\nu a_{\mu\nu} \phi_\nu, \quad (1.23)$$

where ϕ_ν is a second set of linearly independent wavefunctions. The total wavefunction will be a Slater determinant $\Psi = \mathcal{A}(\psi_1 \dots \psi_N)^{13}$. Similarly a second Slater determinant can be formed based on the second set of wavefunctions, namely $\Phi = \mathcal{A}(\phi_1 \dots \phi_N)$. If the wavefunctions are properly normalized then $\Psi = \Phi$. Calculations of the density profile of Ψ for light systems such as ^8Be , ^{12}C and ^{24}Mg suggest clustered formations [35]. A comparison can be made with the Bloch-Brink α -cluster model [39] (the model will be

¹³A Slater determinant is a wavefunction which describes the nature of a system composed of multiple fermions. \mathcal{A} is the symmetrization operator which accounts for the Pauli principle needed in this type of systems.

worked out below). The wavefunction describing systems of $N \alpha$ particles is given by [39, 40]

$$\Phi_\alpha = K_{\phi_\alpha} \mathcal{A} \prod_{i=1}^N \phi_{\alpha,i}(\mathbf{r}), \quad (1.24)$$

where K_{ϕ_α} is a normalization factor $\phi_{\alpha,i}$ is the wavefunction for isolated α particles and is given by

$$\phi_{\alpha,i} = \sqrt{\frac{1}{b^3 \pi^{3/2}}} \exp \left[\frac{-(\mathbf{r} - \mathbf{R}_i)}{2b^2} \right]. \quad (1.25)$$

In the previous equation $b = (\hbar/m\omega)^{1/2}$ and can be interpreted as the size of the alpha particle. Calculations for the same light systems as before show that the overlap $\langle \phi_i | \phi_{\alpha,i} \rangle$ is large. This suggest that the wavefunctions $\phi_{\alpha,i}$ in Equation (1.24) can be replaced by ϕ_i , or, equivalently

$$\Psi \sim K_{\phi_\alpha} \mathcal{A} \prod_{i=1}^N \phi_{\alpha,i}(\mathbf{r}). \quad (1.26)$$

This eventually shows that while the harmonic oscillator is a very simple description of the mean field, the α cluster structure in light nuclei can already be predicted. Note however that for accurate calculations, more realistic potentials should be considered [35].

Figure 1.12 can be used to get an idea in which type of orbits the valence nucleons reside in $4n + 1, 4n + 2, \dots$ systems. The formation of a σ or π orbital is determined by the orbital angular momentum of the single particle energy level. In the case of a p -orbital, $l = 1$ and if its projection m onto the separation axis equals 0, a σ orbit is formed. If $m = 1$, i.e. the projection is parallel to the separation axis, a π orbit is formed.

There is however also a need for a theory from which the orbitals are found directly. For this purpose, once more a mean field theory can be used. In the case of an additional particle, one can assume that the interaction between said particle and an α particle has a short range. This way, the particle interacts only with one α particle at a time. Then for each of the $n \alpha$ particles a separate wavefunction ψ_i for the interaction with the nucleon can be assumed. For a simple case such as ${}^9\text{Be}$ which can be considered as a $\alpha + n + \alpha$ composite, the average energy of the neutron is then given by [19, 20]

$$E(\psi_1 + \psi_2) = \frac{\int (\psi_1 + \psi_2) H (\psi_1 + \psi_2) d\mathbf{r}}{\int (\psi_1 + \psi_2)^2 d\mathbf{r}} \approx B + R + Q. \quad (1.27)$$

The hamiltonian H is given by $V_1 + V_2 + T$ with $V_{1,2}$ the interaction potentials of the neutron with the respective α particles and T the kinetic energy. The approximation only holds when there is little overlap between ψ_1 and ψ_2 . B, R and Q are given by $\int \psi_1 (V_1 + T) \psi_1 d\mathbf{r}$, $\int \psi_2 V_2 \psi_2 d\mathbf{r}$ and $\int \psi_1 H \psi_2 d\mathbf{r}$ respectively and have the interpretation of the binding energy of the neutron in the neighborhood of the first α particle, some additional potential energy due to the presence of the second α particle and the exchange energy.

In general the wavefunction of the neutron in a system with n cores is a linear combination of the single core wavefunctions ϕ_i and can be written as

$$\Phi = \sum_{i=1}^n C_i \psi_i. \quad (1.28)$$

One has thus to find the coefficients C_i by diagonalizing the Hamiltonian of the system. This approach is known as the Hückel method, first developed in the framework of molecular physics [15, 19]. Solving $H\Phi = E\Phi$ leads to following determinant

$$\begin{vmatrix} H_{11} - E & H_{12} - ES_{12} & \dots & H_{1n} - ES_{1n} \\ H_{21} - ES_{12} & H_{22} - E & & H_{2n} - ES_{2n} \\ \vdots & \vdots & \ddots & \vdots \\ H_{n1} - ES_{n1} & H_{n2} - ES_{n2} & \dots & H_{nn} - E \end{vmatrix} = 0, \quad (1.29)$$

where $H_{ij} = \int \psi_i H \psi_j^* d\tau$ and $S_{ij} = \int \psi_i \psi_j^* d\tau$. H_{ii} refers to a single core and when only one type of core is present, these integrals should result in the same value, α . H_{ij} corresponds to two cores and can also be assumed to yield the same contribution β when the two cores are neighbors. Otherwise this simply yields 0. Assuming again that the wavefunctions ϕ_i have a short range, the overlap integrals S_{ij} are negligible and can also be set to 0. Note that in order to use this assumption one has to assume a specific configuration for the cluster structure. Possible structures in the case of ^{12}C could for example be a linear chainlike structure or a triangular structure. Solving the eigenvalue problem of Equation (1.29) results in the coefficients needed in Equation (1.28). From this the probability density $|\Phi|^2$ for the additional neutron can be calculated. This probability density resembles the molecular orbitals in which the valence electrons are found in molecules. Because of this resemblance, the additional neutrons are often referred to as the valence neutron of the cluster structure. When more than one valence neutron is present, the orbitals are filled in a similar as in molecular theory. As each orbital is related to a specific energy, the addition of more valence neutrons increases the overall energy of the system. A more detailed discussion of the Hückel method can be found in Reference [41]. Due to the resemblance to molecules, $4n+1$, $4n+2$ and $4n+3$ type nuclei are also referred to as *molecular clusters*.

1.2.3 Advanced theories

The mean field theories discussed in the previous section are able to predict the basics of cluster formation, but fail when the details must be found. To address this problem, more sophisticated methods have been proposed. Some of these methods will be presented in this section.

The Bloch-Brink alpha cluster model (ACM)

This model is useful for the treatment of $N\alpha$ systems [15]. The model assumes that two protons and neutrons cluster together into α particles and can be represented by a 0s-wavefunction. The wavefunction was given earlier in Equation (1.25). For each α particle such a wavefunction is postulated and the resulting total wavefunction will be a Slater determinant of these wavefunction. This was also presented earlier in Equation (1.24). The only thing that remains to be fixed is the relative positions of the α particles.

The Hamiltonian related to a $N\alpha$ system is given by

$$H_{BB} = \sum_{i=1}^A T_i + \frac{1}{2} \sum_{i \neq j} [v(\mathbf{r}_i - \mathbf{r}_j - v_c(\mathbf{r}_i - \mathbf{r}_j)) - T_{cm}], \quad (1.30)$$

where the $\alpha-\alpha$ interactions are described through an effective nucleon-nucleon interaction potential $v(\mathbf{r}_i - \mathbf{r}_j)$ and the Coulomb potential $v_c(\mathbf{r}_i - \mathbf{r}_j)$. T_i and T_{cm} represent the kinetic energy of the i th α particle and center of mass¹⁴ energy respectively. This system can be solved through variational methods in which both the size parameter b and the relative positions \mathbf{r}_i are optimized. This usually results in wavefunctions which predict crystalline-like configurations.

The fact that really fixed positions for the α particles are found is however one of the shortcomings of the model as it can not predict the gas-like structures. To allow for this type of structure, the formalism must be adapted somewhat. The new $N\alpha$ particle state can be written as [42]

$$|\Phi_{N\alpha}\rangle = (C_\alpha^\dagger)^N |0\rangle, \quad (1.31)$$

where $|0\rangle$ represents the vacuum state and C_α^\dagger the α particle creation operator¹⁵. The creation operator is defined as follows

$$\begin{aligned} C_\alpha^\dagger = & \int d^3R \exp\left(-\frac{R_x^2}{\beta_x^2} - \frac{R_y^2}{\beta_y^2} - \frac{R_z^2}{\beta_z^2}\right) \int d^3r_1 \dots d^3r_4 \\ & \times \varphi_{0s}(\mathbf{r}_1 - \mathbf{R}) a_{\sigma_1 \tau_1}^\dagger(\mathbf{r}_1) \dots \varphi_{0s}(\mathbf{r}_4 - \mathbf{R}) a_{\sigma_4 \tau_4}^\dagger, \end{aligned} \quad (1.32)$$

where $\beta_{x,y,z}$ represent the size parameters of the deformed harmonic oscillator, $a_{\sigma\tau}^\dagger$ represents the nucleon creation operator and $\varphi_{0s}(\mathbf{r})$ the s -wavefunction of the nucleon. It can be shown that the wavefunction related to the state $|\Phi_{N\alpha}\rangle$ is given by

$$\langle \mathbf{r}_1 \sigma_1 \tau_1, \dots, \mathbf{r}_N \sigma_N \tau_N | \Phi_{N\alpha} \rangle \propto \mathcal{A} \left[\exp \left\{ -2 \sum_{i=1}^n \sum_{j=x,y,z} \left(\frac{X_{ij}^2}{B_j^2} \right) \right\} \phi(\alpha_1) \dots \phi(\alpha_N) \right], \quad (1.33)$$

where $B_j = b^2 + 2\beta_j^2$ and can be interpreted as the size parameter of the nucleus in three spatial dimensions [43]. $X_i = \frac{1}{4} \sum_{k=1}^4 \mathbf{r}_{ik}$ represent the center of mass coordinate of the i th α cluster. From Equation (1.33) it becomes apparent that the $N\alpha$ cluster all occupy the same deformed $0s$ orbit. This wavefunction is given by the exponential factor. This suggest that indeed the description of a Bose-Einstein condensate can be satisfied. It can also be shown that the wavefunction can be decomposed into a linear combination of Bloch-Brink wavefunctions [42]. Note also that this new description to some extent takes account of the fermionic degrees of freedom explicitly. This was not the case in the standard Bloch-Brink method.

Microscopic theories

The simple Bloch-Brink description assumes the α particles to be single identities and only through the antisymmetrization it takes account of the nucleons. This approach might not be a good approximation for larger cluster cores [15]. For this reason, microscopic approaches have to be introduced. Two methods will be presented, the *Resonating Group*

¹⁴The center of mass frame is a frame in which the total momentum of the particles involved is zero. More information on the center of mass frame will be given in Section 3.3.

¹⁵In the formalism of second quantization, creation and annihilation operators are used. These operators create or destroy particles in a particular state $|\phi\rangle$. The vacuum state is a state which is essentially empty such that $C|0\rangle = 0$ where C is the annihilation operator of a particle.

Method (RGM) and *Generator Coordinate Method (GCM)*. Both have been extensively reviewed by Descouvement [44] and Saito [33]. For a full treatment of the theories, the reader is referred to those works.

In the case of microscopic models the a Hamiltonian with respect to all individual nucleons must be solved. The Hamiltonian of the shell model given in Equation (1.1) suffices. As usual the Schrödinger equation $H\Psi = E_T\Psi$ must be solved in which E_T is the total energy of the system and Ψ the RGM wavefunction defined as (for a two-cluster system)¹⁶

$$\Psi(\xi_{1,i}, \xi(2, i), \rho) = \mathcal{A}(\phi_1(\xi_{1,1})\phi_2(\xi_{2,i})g(\boldsymbol{\rho})). \quad (1.34)$$

In the previous equation $\xi_{1,i}$ and $\xi_{2,i}$ are defined as

$$\begin{aligned} \xi_{1,i} &= \mathbf{r}_i - \mathbf{R}_{cm,1} \text{ if } i = 1, \dots, A_1 \\ \xi_{2,i} &= \mathbf{r}_i - \mathbf{R}_{cm,2} \text{ if } i = A_1 + 1, \dots, A, \end{aligned} \quad (1.35)$$

where $\mathbf{R}_{cm,1}$ and $\mathbf{R}_{cm,2}$ are the center of mass coordinates of the first and second cluster. Furthermore it is assumed that the first cluster is composed of the first A_1 nucleons. The other nucleons are inside the second cluster. $\phi_1(\xi_{1,i})$ and $\phi_2(\xi_{2,i})$ represent the internal wave functions of the two clusters and $g(\boldsymbol{\rho})$ is the relative wavefunction of the cluster with $\rho = \mathbf{R}_{cm,2} - \mathbf{R}_{cm,1}$. The objective of the model now is to find $g(\boldsymbol{\rho})$ by solving the Schrödinger equation. The result is the RGM equation given by

$$\left(-\frac{\hbar^2}{2\mu}\Delta_\rho + V_D(\boldsymbol{\rho})\right)g(\boldsymbol{\rho}) + \int K(\boldsymbol{\rho}, \boldsymbol{\rho}')g(\boldsymbol{\rho}')d\boldsymbol{\rho}' = (E_T - E_1 - E_2)g(\boldsymbol{\rho}). \quad (1.36)$$

In this equation Δ_ρ is the Laplacian with respect to ρ . μ , E_1 , E_2 and $V_D(\boldsymbol{\rho})$ are the reduced mass, the internal energies of the first and second cluster component and direct potential respectively. They are defined as:

$$\mu = m_N \frac{A_1 A_2}{A_1 + A_2} \quad (1.37)$$

$$E_i = \langle \phi_i | H | \phi_i \rangle \quad \text{with } i = 1, 2 \quad (1.38)$$

$$V_D(\boldsymbol{\rho}) = \langle \phi_1 \phi_2 | \sum_{i=1}^{A_1} \sum_{j=1}^{A_2} V_{ij} | \phi_1 \phi_2 \rangle \quad (1.39)$$

$K(\boldsymbol{\rho}, \boldsymbol{\rho}')$ can be written in terms of the RGM kernels $\mathcal{H}(\boldsymbol{\rho}, \boldsymbol{\rho}')$ and $\mathcal{N}(\boldsymbol{\rho}, \boldsymbol{\rho}')$. These are defined as:

$$\begin{Bmatrix} \mathcal{H}(\boldsymbol{\rho}, \boldsymbol{\rho}') \\ \mathcal{N}(\boldsymbol{\rho}, \boldsymbol{\rho}') \end{Bmatrix} = \langle \phi_1 \phi_2 \delta(\boldsymbol{\rho} - \mathbf{r}) | \begin{Bmatrix} 1 \\ H \end{Bmatrix} | \mathcal{A} \phi_1 \phi_2 \delta(\boldsymbol{\rho}' - \mathbf{r}) \rangle. \quad (1.40)$$

A major drawback of the RGM method is that calculations are often very lengthy and hard. A solution to this problem is the GCM. The RGM and GCM can be shown to be equivalent [44]. The basic idea of the GCM is to rewrite the wavefunction of Equation (1.34) as a superposition of Slater determinants. This can be achieved by expanding $g(\boldsymbol{\rho})$ in terms of Gaussian function at different coordinates. The use of Slater determinants makes computations more applicable to numerical analysis.

¹⁶For simplicity, the spin and isospin components are not treated explicitly. See Reference [44] for extensions treating this matter.

The relevant GCM Slater determinant for two clusters at positions \mathbf{S}_1 and \mathbf{S}_2 is given by

$$\Phi(\mathbf{R}) = \frac{1}{\sqrt{N_0}} \mathcal{A} \Phi_1(-\lambda \mathbf{R}) \Phi_2((1 - \lambda) \mathbf{R}), \quad (1.41)$$

where N_0 is a normalization factor and equal to $\frac{A!}{A_1! A_2!}$, $\mathbf{R} = \mathbf{S}_1 - \mathbf{S}_2$, Φ_1 and Φ_2 are the one-center Slater determinants related to the two clusters. Their position in space is defined through the parameter λ . They are given by (centered around \mathbf{S})

$$\Phi_i = \frac{1}{\sqrt{A_1!}} \mathcal{A} \{\hat{\varphi}_1(\mathbf{S}) \dots \hat{\varphi}_{A_i}(\mathbf{S})\}, \quad (1.42)$$

where the functions $\hat{\varphi}_i$ represent wavefunctions of the individual nucleons. The radial components are harmonic oscillator functions characterized by the oscillator parameter b . The GCM calculations can be made easier if the wavefunction of Equation (1.41) is rewritten such that it is factorized in its center of mass and radial components and a common value for b is taken. The new form of the wavefunction reads

$$\Phi(\mathbf{R}) = \frac{1}{\sqrt{N_0}} \Phi_{cm}(\mathbf{R}_{cm}) \mathcal{A} \{\phi_1 \phi_2 \Gamma(\boldsymbol{\rho}, \mathbf{R})\}. \quad (1.43)$$

The function ϕ_1 and ϕ_2 are the same as used in Equation (1.34) and \mathbf{R}_{cm} is the center of mass coordinate of the whole system. $\Phi_{cm}(\mathbf{R}_{cm})$ and $\Gamma(\boldsymbol{\rho}, \mathbf{R})$ represent the center of mass and radial components respectively. They are given by

$$\Phi_{cm}(\mathbf{R}_{cm}) = \left(\frac{A}{\pi b^2} \right)^{\frac{3}{4}} \exp \left(-\frac{A}{2b^2} \left[\mathbf{R}_{cm} + \mathbf{R} \left(\lambda - \frac{A_2}{A} \right) \right] \right) \quad (1.44)$$

and

$$\Gamma(\boldsymbol{\rho}, \mathbf{R}) = \left(\frac{\mu}{\pi m_N b^2} \right)^{\frac{3}{4}} \exp \left(-\frac{\mu}{\pi m_N b^2} (\boldsymbol{\rho} - \mathbf{R})^2 \right). \quad (1.45)$$

Now the basic form of the wavefunction is known. What rests is to solve the Schrödinger equation in order to find the details of the wavefunction and the related energy states.

Antisymmetrized molecular dynamics (AMD)

Both the Bloch-Brink method, RGM and GCM have one shortcoming. They all assume a priori a wavefunction which has inherently clustering characteristics. It is thus useful to develop techniques which do not make such an assumption and compare the results with the previous formalisms. *Antisymmetrized Molecular Dynamics (AMD)* is such a formalism. A review of this formalism can be found in References [45, 46]. Cluster structures in light elements are indeed predicted through this technique [23, 46, 47].

In AMD, the system is represented by the wavefunction Φ which is a linear combination of AMD wavefunctions Φ_{AMD} . Φ_{AMD} is a Slater determinant of wavefunctions φ_i who correspond to individual nucleons. For a system of A nucleons the following can be considered:

$$\begin{aligned} \Phi_{AMD}(\mathbf{Z}) &= \frac{1}{\sqrt{A!}} \mathcal{A} \{\varphi_1, \varphi_2, \dots, \varphi_A\}, \\ \varphi_i &= \phi_{\mathbf{X}_i}(\mathbf{r}_j) \chi_i \tau_i, \end{aligned} \quad (1.46)$$

where

$$\begin{aligned}\phi_{\mathbf{X}_i}(\mathbf{r}_j) &\propto \exp\left[-\nu\left(\mathbf{r}_j - \frac{\mathbf{X}_i}{\sqrt{\nu}}\right)\right] \\ \chi_i &= \begin{pmatrix} 1/2 + \xi_i \\ 1/2 - \xi_i \end{pmatrix}.\end{aligned}\tag{1.47}$$

The functions for $\phi_{\mathbf{X}_i}$ represent Gaussian wave packets which are centered at \mathbf{X}_i and characterized by a second parameter ν . χ_i represents the intrinsic spin function parameterized by ξ_i (which can take value $\pm 1/2$) and τ_i represents the isospin. \mathbf{Z} serves as a shorthand notation for the set of all used parameters, i.e. $\mathbf{Z} \equiv \{\mathbf{X}_i, \dots, \mathbf{X}_A, \xi_i, \dots, \xi_A\}$.

The Slater determinants as presented above do not possess a good parity and total angular momentum I however [48]. Spin and parity projectors can be introduced to resolve this problem. The properly projected wavefunctions are given by

$$\begin{aligned}\Phi_{AMD}^{\pm} &= \frac{1}{2}(1 \pm P)\Phi_{AMD}, \\ \Phi_{AMD}^I &= P_{MK'}^I \Phi_{AMD},\end{aligned}\tag{1.48}$$

where $\frac{1}{2}(1 \pm P)$ and $P_{MK'}^I$ are the parity and total angular momentum projection operators respectively. M and K' denote components of the angular momentum \mathbf{I} . It is possible to construct a wavefunction on which both projection act.

The next step is to find the optimal set of parameters \mathbf{Z} which minimize the energy of the system. This energy is defined as

$$\mathcal{E} = \frac{\langle \Phi | H | \Phi \rangle}{\langle \Phi | \Phi \rangle},\tag{1.49}$$

where H denotes as usual the Hamiltonian. Such a minimization is done through variational techniques. One of these techniques is the frictional cooling method [47]. In this technique the following equations have to be solved

$$\frac{d\mathbf{X}_i}{dt} = (\lambda + i\mu) \frac{1}{i\hbar} \frac{\partial}{\partial \mathbf{X}_i^*} \frac{\langle \Phi | H | \Phi \rangle}{\langle \Phi | \Phi \rangle},\tag{1.50}$$

where λ and $\mu < 0$ are arbitrary real numbers. These equations are solved iteratively where each iteration represents a time step. It can be shown that this always leads to a minimization of \mathcal{E} [45]. The simplest way to solve these equations is by using a wavefunction which only went through the parity projection step. Afterwards, a projection with respect to the total angular momentum is performed. However, better results are found if one redoing this kind of calculation once the second projection step is done [45]. Note that this procedure leads to the lowest I^\pm state. The wavefunctions of the excited states can be found in a similar way as before, but in addition there is the requirement that they remain orthogonal to the lower lying states.

1.3 The cluster structure of ^{10}B

In the preceding sections some arguments were given to understand why cluster structures might appear in certain nuclei. However, the details of clustering behavior is not yet fully

understood from the point of view of the nucleon-nucleon interaction. An interesting set of nuclei to study in this respect are ^{10}Be , ^{10}B and ^{11}B .

In terms of the nuclear shell model, ^{10}Be can be regarded as composed of two α cores with two additional valence neutrons. AMD calculations show that some of the states of ^{10}Be exhibit a cluster structure which is molecular-like [49, 50]. The 0_1^+ state corresponds to a $(3/2^-)^2$ configuration of the valence neutrons. The neutrons reside in π orbitals. The 0_2^+ state has a $(1/2^+)^2$ configuration. For both states rotational bands are predicted. However, for the second band a much larger moment of inertia ϑ is predicted. This would then correspond to a $(\sigma)^2$ configuration. On the other hand, the groundstate does not exhibit a very pronounced cluster structure. This was to be expected from the Ikeda picture as the α, n and $2n$ decay thresholds lie at quite high energies (7.41, 6.81 and 8.48 MeV respectively) [15, 21]. More recent studies predict a state at 12 MeV with a $2\alpha +$ dineutron condensed gas structure [51, 52]. A first 2^+ state is found at 3.36 MeV [21]. This is in agreement with the AMD calculations and the state would be the second member of the first rotational band. Experimentally the second 0^+ state is found at an excitation energy of 6.8122 MeV. 2^+ and 4^+ states are found at excitation energies of respectively 7.542 and 10.15 MeV¹⁷ [54, 55] and could be members of the second rotational band. These values are also in agreement with theory.

As ^{11}B has only one proton less than ^{12}C one could expect a similar structure. It was argued in Section 1.2.1 that the cluster structure of ^{12}C is gas-like. Experimentally a $3/2_3^-$ state is found at an energy of 8.56 MeV. This state could not be described via nuclear shell model calculations [34]. Note that this state lies close to the α decay threshold found at an energy of 8.6641 MeV [21]. AMD calculations predict the $3/2_3^-$ state at an excitation energy which is about 2 MeV larger. However the electromagnetic transition strengths which could not be reproduced through shell model calculations, are in pretty good agreement with experiment [34] in the case of the AMD calculations. Comparisons with the 0_2^+ Hoyle state of ^{12}C show similar values for the transition strengths. For this reason, it is believed that the $3/2_3^-$ state of ^{11}B also has a gas-like $2\alpha + t$ structure¹⁸. Calculations of the density profile also suggest this structure [51].

^{10}B is an odd-odd nucleus with $N = Z = 5$. Naively it can be expected that certain states of this nucleus exhibit similar cluster structures as the neighboring nuclei which only differ in the exchange of a proton and a neutron in the case of ^{10}Be and the addition of a neutron in the case of ^{11}B . However, as was written above, the cluster structures of these two neighbors are very different. It is thus not clear whether a predominantly gas-like structure composed of 2α particles and a deuteron¹⁹ can be expected, or a system in which the deuteron breaks up into a proton and neutron which form molecular bonds between the two α cores. A thorough study of the properties of ^{10}B could reveal this. As a result, more information can be obtained about the nucleon-nucleon interaction in the framework of nuclear clustering.

1.3.1 Theoretical studies of ^{10}B

Nishioka has studied the structure of both ^{10}Be and ^{10}B via the OCM for states up to an excitation energy of 7.5 MeV [56]. In his treatment, a wavefunction with an explicit

¹⁷Note however that this state was previously assigned to be a 3^- state [53].

¹⁸Tritium (t) the ^3He nucleus.

¹⁹The deuteron (d) is the ^2H nucleus.

$2\alpha + d$ structure was considered. It argued that for isospin $T = 0$ levels the intrinsic spin \mathbf{S} must couple to 1 in order to have a bound deuteron. Otherwise, there is a breakup into a proton and neutron. Calculations have been performed for both the $T = 1$ and $T = 0$ states of ^{10}B . As the dinucleon pair couples to spin 0 in the case of $T = 1$, the spin-orbit interaction was not considered in this case. For the $T = 0$ this interaction was properly included. In both cases, the energy level scheme is reproduced rather well, but there calculated results lower compared to experiment by about 2-3 MeV for the positive parity states and higher by 2-4 MeV for the negative parity states. The $(I^\pi; T) = (1_3^+; 0)$ at 5.18 MeV, $(0_2^+; 1)$ at 7.56 MeV and $(2_3^+; 0)$ could be reproduced in this study, whereas this was not possible in shell-model calculations. Therefore it is expected that these states exhibit a prominent cluster structure. The author argued that this should be a $\alpha + ^6\text{Li}$ configuration.

Fujiwara and Tang have studied ^{10}B through RGM in which also a $2\alpha + d$ model was considered [57]. To simplify calculations, clusters were coupled into a new model space spanned by the $\alpha + ^6\text{Li}$, $\alpha + ^6\text{Li}^*$, $d + ^8\text{Be}$ and $d + ^8\text{Be}^*$ configurations. ${}^6\text{Li}^*$ and ${}^8\text{Be}^*$ are to be understood as having inherent cluster structures themselves, namely $d + \alpha$ and $\alpha + \alpha$ configurations respectively. Compared to the study by Nishioka, only the $T = 0$ levels were considered, arguing that the cluster structures for the $T = 1$ would be very similar to the $T = 0$ levels with the exception that the deuteron would break up into a $n + p$ pair. The Coulomb and non-central components of the nucleon-nucleon interaction were also neglected. Overall the energy level scheme is reasonably well reproduced. However, the levels could only be related with the experimentally observed states after considering the non-central part after all. Nevertheless, the energies of all states were somewhat overestimated. On the basis of the calculations a $\alpha + ^6\text{Li}$ configurations was suggested for the $I^\pi = 3_1^+, 1_1^+, 1_2^+, 2_1^+$ and 0_2^+ states. A $\alpha + ^6\text{Li}^*$ configuration was suggested for the 3_2^+ and 2_3^+ states. For The negative parity 2_2^- state a $\alpha + ^6\text{Li}$ configuration was found also. It should be noted that the 1_1^+ state could only be reproduced in this model and not through shell model calculations. For this reason, it is argued that this model has a high degree of clustering.

Kanada-En'yo *et al.* have studied low lying states of ^{10}B via AMD [58]. Especially the effect of the spin-orbit interaction on the dinucleon pair is demonstrated. To treat the two-body interaction, effective nuclear interactions are considered. However, it is also shown that part of the spin-orbit contribution can be related to the three-body interaction between the nucleons. The study focuses mostly on the three lowest states, namely the $(I^\pi; T) = (3_1^+; 0), (1_1^+; 0)$ and $(0_1^+; 1)$ states. By calculating the $\langle \mathbf{S}^2 \rangle$ values for the states, where \mathbf{S} is the spin of the dinucleon pair, it is deduced that the $T = 0$ states have a $(S; T) = (1; 0)$ configuration. This configuration is related to the deuteron. The $T = 1$ has a dominant $(S; T) = (0; 1)$ component. So there is a break up of the deuteron in this state. There is however, also a slight mixing of a $S = 1$ component to this state. The density profiles for the three states can be seen in Figure 1.13. It can be seen that in the case of the 3_1^+ and 0_1^+ states the dinucleon resides closely to the 2α pair. In the case of the 1_1^+ state the structure develops more in space. This effect can be understood from via the spin-orbit term which is attractive. Only in the case of the 1_1^+ state, the relative angular momentum \mathbf{L} is zero such that the spin-orbit contribution also vanishes.

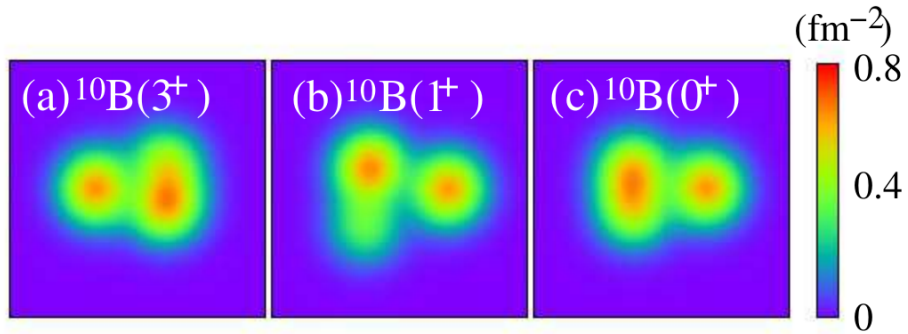


Figure 1.13: The calculated density profiles of the three lowest lying states of ^{10}B . The dinucleon pair is more spatially removed from the 2α core in the case of the 1_1^+ state. From [58].

1.3.2 Rotational band structure of ^{10}B

An overview of the energy level scheme which was experimentally determined can be seen in Figure 1.14. Up to about an energy of 7 MeV, the states are well known. The width of these states are well determined and for each the decay mode is known. At an energy of 4.4610 MeV the α decay threshold is found, the deuteron decay threshold is found at an energy of 6.02767 MeV. From the Ikeda picture of clustering, these decay thresholds can be interesting to find the lowest lying states exhibiting a cluster structure related to that decay. The 1_3^+ state at 5.180 MeV has a width of 110 keV and decays essentially for 100% through α emission [28]. Because of this large α decay width, it can be expected that the state exhibits a cluster structure with an α particle as one of its constituents [15]. If this is indeed the case, this state would be the first state of a rotational band. The 2_2^+ state is found at 5.9195 MeV. This state has a width of 5.82 keV and also decays essentially through α emission. Because of these reasons, this stage might be the second member of the rotational band. However several studies have found a state at an energy of 7.002 MeV. This state has a width of about 100 keV and decay through both α and deuteron emission has been observed [28]. There is no universal agreement on the spin of this state. Balakrishnan *et al.* studied elastic scattering of α particles on ^6Li and reported a tentative 2^+ spin assignment for this state [59]. If this spin assignment is correct, this state could be the second band member rather than the state at 5.9195 MeV. On the other hand, Young *et al.* studied ^{10}B through neutron pickup from ^{11}B and reported a 3^+ assignment for the state [60]. A study of four nucleon pickup by ^{14}N by Oelert *et al.* reported a tentative 3^+ assignment for the state [61].

A graph on which the three discussed energy levels are plotted against $I(I + 1)$ can be seen in Figure 1.15. This kind of plot is useful because the states of the rotational band should follow the relationship of Equation (1.16). For each state the spin projection Ω should be the same such that the most important parameter is the slope. Dependent on which is the correct spin-parity assignment of the 7.002 MeV state, two rotational bands can be constructed. If $I^\pi = 2^+$, a higher slope is found and consequently the moment of inertia ϑ is smaller. As a result, the cluster structure is expected to be more compact. Following this band, a 3^+ state would be expected at an energy slightly below 10 MeV and a 4^+ state at roughly 13 MeV. On the other hand, if $I^\pi = 3^+$ is the correct assignment

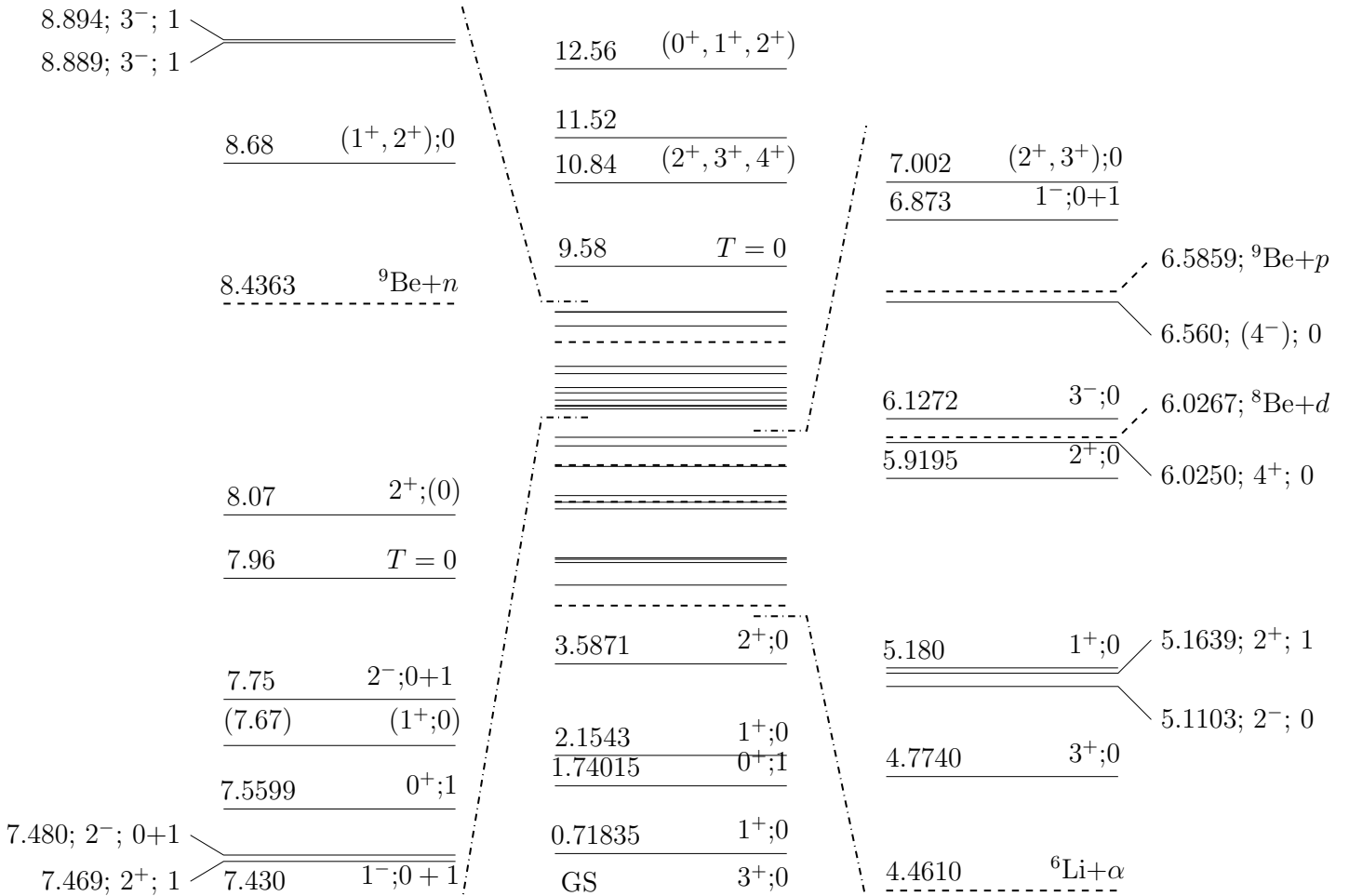


Figure 1.14: Energy level scheme of ^{10}B based on a compilation by Tilley *et al.* [21] and References [59–62]. The energies (in MeV) are indicated on the left side of the bars. The spin, parity and isospin $I^\pi; T$ are indicated on the right side of each bar. The dashed lines indicate the decay thresholds. Values in brackets are tentative.

for the 7.002 MeV state, the state would contribute to a rotational band for which ϑ is larger. In this case a 4^+ state could be expected at an energy of about 8.5 MeV.

In order to be sure which of the two possible bands is correct, information needs to be added from states at higher excitation energies. Referring again to Figure 1.14, it can be seen that for some of the states above the 7.002 MeV the I^π assignments are missing. On top of that, the decay modes are not always known, and even if certain decay channels have been observed, the partial widths of those decays are uncertain [28].

1.3.3 Experimental proposal

During the summer of 2015 an experiment has been performed at L’Institut de Physique Nucléaire d’Orsay (IPNO) with the goal to study the possible cluster structure of ^{10}B . To do this, *resonant elastic and inelastic scattering* of ${}^6\text{Li}$ and α in inverse kinematics was performed. During a resonant reaction process the incident ${}^6\text{Li}$ and target α nuclei merge and form a *compound nucleus*. In this case the compound nucleus is ^{10}B . After typically $10^{-14} \sim 10^{-15}$ seconds, the compound nucleus breaks up again. In almost all cases the

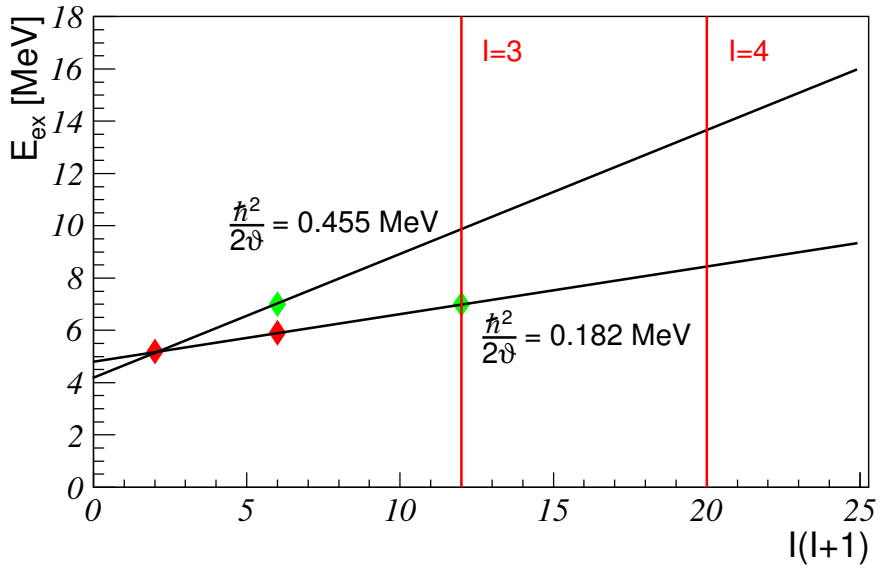


Figure 1.15: Plot with some of the energy levels of ^{10}B which could be part of a rotational band. The point in red indicate states for which the spin I is well known. The 7.002 MeV state is indicated in green together with its two possible spin assignments. The two spin assignments lead to different rotational bands.

fragments are the original incident and target nuclei. An important feature of this kind of reaction is that it has an enhanced probability to occur when the energy of the ^6Li particle is such that the total energy of the compound system is equal to an energy of one of its excited states. This way one has a direct probe for the various states of ^{10}B . Another important feature is that not all incident-target particle combinations will easily lead to a compound system for each of its excitation levels. The formation of the compound system is also enhanced if the partial decay width for one of the particles used in the reaction is large. From theory (see Section 1.3.1) it is expected that cluster structures of ^{10}B have two α particles as its constituents. Moreover, as explained in the preceding section, the states exhibiting such a cluster configuration are expected to have a large α decay width [15]. This immediately explains the choice to use ^6Li and α as the incident-target particle combination. The theory of resonant reactions will be worked out in detail in Chapter 3.

Up to now, elastic and inelastic scattering of ^6Li and α has only been performed for α particle energies E_α between 2.0 and 5.0 MeV and between 13.3 and 18.0 MeV. These energies correspond to ^{10}B excitation energies $E_{ex}(^{10}\text{B})$ between 5.66 and 7.46 MeV and 12.26 and 15.26 MeV respectively²⁰ [21]. Only one study considered another energy range, namely $E_\alpha = 9.5$ to 12.5 MeV ($E_{ex}(^{10}\text{B}) = 10.16$ to 11.96 MeV) [63]. The present study covered a range of $E_{ex}(^{10}\text{B}) = 7$ to 12.5 MeV which was previously mostly unstudied through this reaction. To be able to cover such a broad range of excitations energies, measurements were done at six different beam energies. These energies were 11.5, 14, 16.5, 19, 21 and 23 MeV. The ACTAR TPC (*ACTive TARget Time Projection Chamber*)

²⁰The conversion to $E_{ex}(^{10}\text{B})$ can be done by considering the center of mass frame, which is the reference frame in which the two particles participating in the reactions have momenta which are equal in magnitude, but have opposing directions. This will be explained in detail in Chapter 3.

demonstrator was used to perform the measurement [64]. Inside the detector a gas mixture is present composed of helium and CO₂. This gas is used for three purposes. Firstly, the gas is used to degrade the beam energy such that energies lying between the initial beam energies can be measured. Secondly, as the gas is partially composed of helium, the gas medium can be used as the target for the experiment. Thirdly, through ionization of the gas, the same gas medium will be used to detect the particles. The basic principles behind the detector and the whole setup will be discussed in detail in Chapter 2. The analysis of the data will be discussed in Chapter 4.

Next to the physics, this study has a second goal. The used detector was only a prototype, so this experiment can also be seen as a proof of principle. Furthermore, the data of this experiment can be used to characterize the detector and point out design issues which might be present. By now the design of the ACTAR TPC has been finalized.

The work presented in this thesis is confined to the reconstruction of the excitation spectrum of ¹⁰B. Since no differential cross sections will be deduced for the found states, no spin-parity assignments are done. As long as this is not done, no definitive conclusions can be made about the cluster states of ¹⁰B.

Chapter 2

Experimental setup

2.1 The ALTO facility

The *Accélérateur Linéaire et Tandem à Orsay (ALTO)*[65] facility is dedicated to physics research in a large number of topics. Two particle accelerators are present in the complex. The 15 MV Van de Graaff Tandem accelerator¹ is able to provide beams ranging from protons to Au ions. Depending on the charge state of the positive ion, energies ranging between 10 and 100 MeV can be reached [66]. Typically beam intensities of 10^{10} pps can be provided. A second 50 MeV electron linac² provided accelerated electrons. These electrons are used to induce fission reactions in a UC_x target such that radioactive beams can be created. The beam provided by the Tandem accelerator supplies multiple experimental setups. A schematic overview of the facility can be seen in Figure 2.1.

2.1.1 The Bacchus spectrometer

The Bacchus spectrometer[67] has a 180° design and can be used to filter out beam contaminants and to select a specific charge state. This is important as a different charge state will lead to different energies of the particles in the beam which will contribute to a loss in resolution during experiments. This can be done by applying a magnetic field. This principle can be understood through the Lorentz force:

$$qvB = \frac{mv^2}{r}, \quad (2.1)$$

where q , v , B , m and r are the charge state, velocity, magnetic field strength, mass of the particle and radius of its trajectory respectively. For fixed values of B and r and if it is furthermore assumed that the beam is pure, i.e. m is constant, it can be seen that a selection of the velocity to charge state ratio can be made. However, the for a particle

¹A tandem accelerator accelerates ions in two steps. Through an electrostatic potential, negatively charged ions are accelerated to about halfway the accelerator. At that point, the ions are stripped of some of their electrons such that they become positively charged. Through a belt, the negative charge is carried away. Since the ions now have a positive charge, they are once more accelerated a second stage.

²Linac is an abbreviation for linear particle accelerator. This type of accelerator provides a series of steps in which an oscillating electric potential is present. This way, each step provides an additional acceleration step for the particles along the linear beamline.



Figure 2.1: Schematic representation of the ALTO facility. Figure from [66].

accelerated through an accelerator, the velocity itself depends on the charge state:

$$v = \sqrt{\frac{2mV}{q}}, \quad (2.2)$$

where V is the applied potential in the accelerator stage. If a fixed value of V is used, a real selection of the charge state can be done. Note that by rotating the spectrometer by a few degrees will change the radius r needed to let the particle exit the spectrometer without losing it.

2.2 The ${}^6\text{Li}$ beam

In the experiment six different beam energies have been used (11.5, 14, 16.5, 19, 21 and 23 MeV). However, the beam was never directly fed to the detector. Instead the beam went to multiple stages to ensure the correct charge state and energy and to decrease the beam energy to about 10^7 pps. This decrease was needed to prevent distortions of the electric field inside the field cage [68]. A schematic overview of these steps until the detector is reached can be seen in Figure 2.2. For all parts leading up to the detector a vacuum was employed of $3 \cdot 10^{-10}$ to $1 \cdot 10^{-9}$ bar.

The beam first reaches a reaction chamber. Inside this chamber a ${}^{208}\text{Pb}$ target with a thickness of $300 \mu/\text{cm}^2$ was placed. Through elastic scattering the intensity of the beam could be reduced. The backing of the target was made of carbon and had a thickness of $25 \mu/\text{cm}^2$. Due to the interactions between the ions and the target, the ions will also lose some of their initial energy. Estimations of the beam energy after leaving the target can be seen in Table 2.1. Additionally a Si(Li) solid state detector³ called Mars83 was installed in the reaction chamber. The detector is circular in shape (1.3 cm^2) and was

³Silicon detectors are typically used to detect ions. In this case lithium was drifted in the silicon to enhance the useful properties. More information on the working principle of Silicon detectors can be found in many books, for example in the book of Knoll [71].

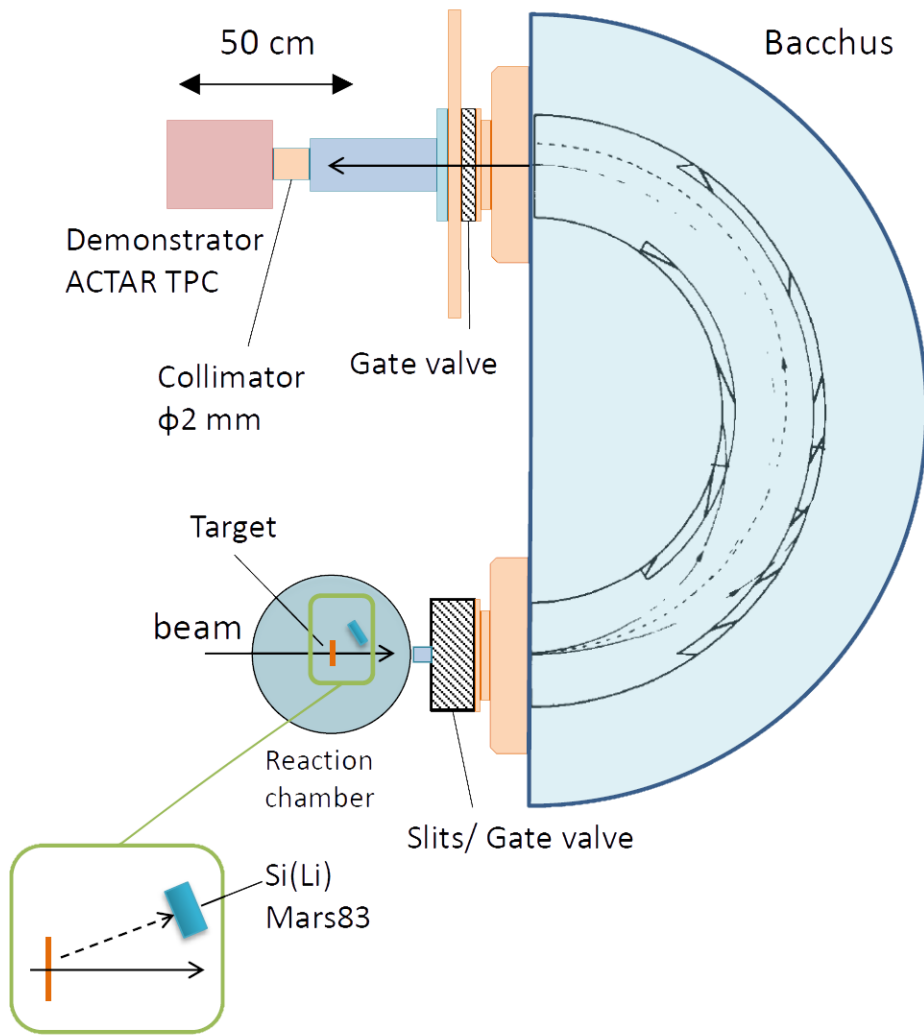


Figure 2.2: Schematic representation of the overall setup. The ${}^6\text{Li}$ beam is provided by the Tandem. The beam has to go through multiple stages before it is able to reach the demonstrator. From [69].

Table 2.1: Energies of the beam after each step in which energy is lost until the actual detector is reached. The calculations have been performed via SRIM [70]. The energies can only be considered as estimates as the energy of each individual particle will be slightly different due to straggling. The Table was reformatted from [69].

	Energy in MeV					
Initial	11.50	14.00	16.50	19.00	21.00	23.00
${}^{208}\text{Pb}$ target	11.37	13.89	16.39	18.90	20.91	22.91
C backing	11.34	13.86	16.37	18.88	20.89	22.89
Mylar (6 μm)	10.10	12.78	15.43	18.04	20.12	22.18

positioned at an angle of 20° and positioned 10 cm from the target. The main purposes of this detector was to monitor the beam intensity and beam energy.

Once the beam leaves the reaction chamber, it has to pass through a set of slits with a diameter of 5 mm. This step is needed to reduce the divergence of the beam (this is related to the energy resolution of the system, see Section 2.3.1). Obviously it also leads to a decrease of the beam intensity. After this step, the beam reaches the Bacchus spectrometer (see Section 2.1.1). The magnetic field was set to allow fully stripped ${}^6\text{Li}$ ions ($q = 6$) to pass through. The field strength could be monitored via a Hall probe⁴. By discarding beam particles with a lower charge state, the intensity was once more reduced. Leaving the spectrometer, the beam passes through a dipole magnet in order to refocus the beam. A collimator with a pitch of 2 mm was installed at the end of the dipole magnet to once more decrease the angular spread of the beam. This also led to a decrease in beam intensity. The total attenuation factor of the beam was estimated⁵ to be $2 \cdot 10^5 \sim 2 \cdot 10^6$. As a last step, the beam has to pass through the entrance window of the detector which separated it from the vacuum conditions in the preceding parts of the setup. The window was made of Mylar⁶. Passing through the window also influenced the beam energy. This is also summarized in Table 2.1.

2.3 The ACTAR TPC demonstrator

2.3.1 Generalities

Detection principles

Traditional nuclear physics experiments use a fixed, thin solid state target. This target is mostly made of stable elements while the incident beam might be radioactive. However, when a beam of exotic nuclei is used, the intensity of this beam is often low. Especially for reactions with a low cross section, this leads to problems in terms of statistics. The most straightforward way to increase the yield, is to use a thick target instead. However the use of such a target degrades the energy resolution of the experiment. In addition, only light particles can be detected. The detection of both reaction products in coincidence can be interesting to reduce the background contamination [71, 72]. Time projection chambers such as ACTAR TPC provide a possible solution to this problem⁷[64].

The basic idea of a time projection chamber can be seen in Figure 2.3. This type of detector uses a gas for the detection of the particles. Ions will (primarily) interact through the Coulomb force with the gas medium such that the gas atoms or molecules get excited or possibly ionized [71]. This way, the ions leave a track of electrons in the gas. By employing an electric field, it becomes possible to collect these charges. If these charges are collected on a segmented plane, it becomes possible to reconstruct the tracks

⁴A Hall probe consists of a slab of semiconductor material and a voltmeter. When the semiconductor is placed in an external magnetic field, the free charge carriers will move to the sides of the slab. This is due to the Lorentz force (see Eq. (2.1)). Negative charges will accumulate on one side, generating a potential across the slab. The voltmeter can measure this potential. Hence, there is a direct relationship between the measured potential and the magnetic field strength.

⁵This estimation was not done by the author of this text. See Ref. [69].

⁶MylarTM is a type of plastic composed of oxygen, hydrogen and carbon.

⁷Remember however that in the present study no radioactive isotopes were used.

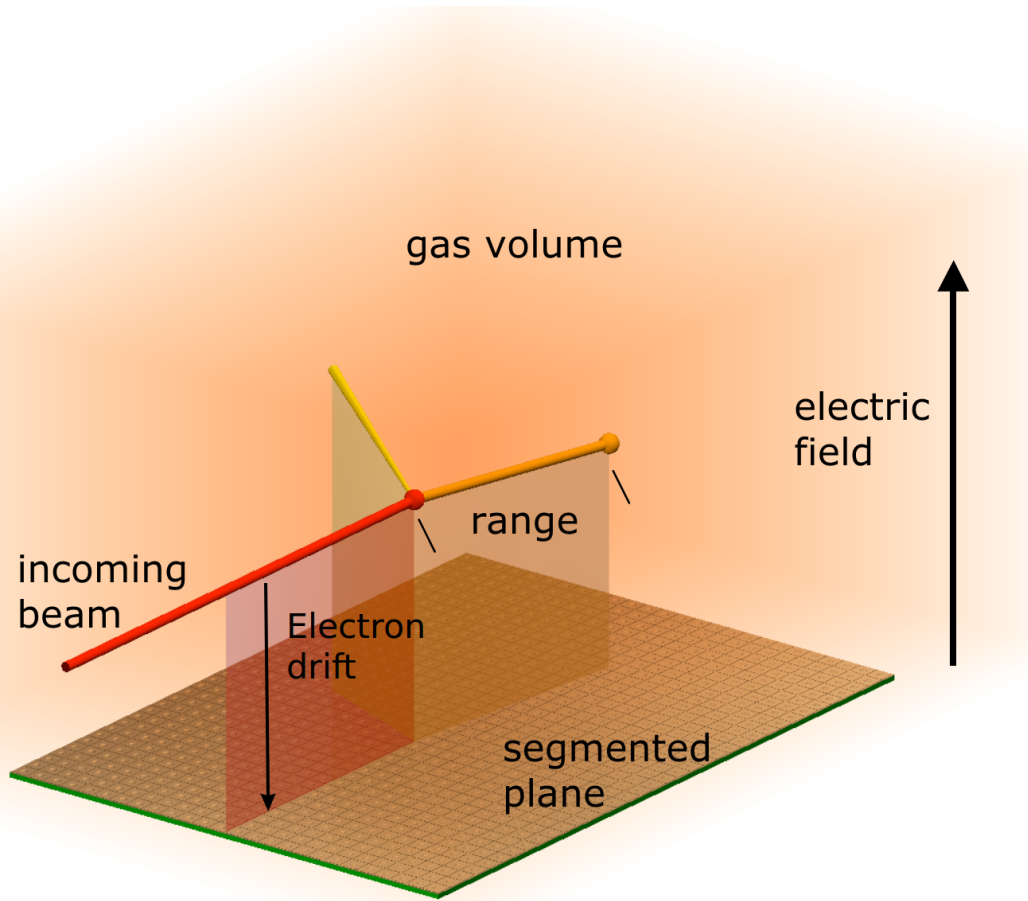


Figure 2.3: Schematic representation of the general principles of ACTAR TPC. The minus signs indicate the generated electrons. Around the gas volume, auxiliary detectors can be placed to detect the energy of particles escaping the volume. Figure adapted from Reference [64].

of the ions in the x - and y -directions. Under the proper conditions, the total charge is also proportional to energy deposited by the ion. The drift velocity of the electrons depends on the strength of the electric field, but this relationship is characteristic for a certain gas composition. By using a fixed electric field strength and by measuring the drift time of the electrons, it becomes also possible to reconstruct the track in the z -direction. A full three-dimensional reconstruction of the ion track can thus be achieved.

The goal of ACTAR TPC is to use the gas not only as detection mechanism, but also as reaction target. In practice, the gas acts as a thick target. The tracking capabilities of the detector allow to reconstruct the tracks of the ${}^6\text{Li}$ particle both before and after the reaction, as well as the track of the recoiling target. This way, the vertex position of the reaction, the length of the tracks and the scattering angles of the two particles can be measured. The stopping power $S = -\frac{dE}{dx}$ of ions depends on the speed of the ion, but this relationship is also characteristic for each ion-gas combination at a fixed gas pressure [71]. The total energy loss for ions traveling a certain distance can be calculated through programs such as SRIM [70]. Hence, the energy of the ${}^6\text{Li}$ ion at the vertex position right before the reaction can be found. The energy deposited in the gas after

the reaction can similarly be found through the range of the track after the reaction (see Figure 2.3). Because the stopping power is characteristic, the generated charge in the gas also immediately provides a way to identify the two reaction products (see Section 4.3). Auxiliary silicon detectors have been placed on both the left and right sides of the detector and on the side opposite to the entrance window. These detectors allow to measure the remaining energy of the particles if they can not be stopped in the gas medium. This allows a full reconstruction of the energetics and kinematics of the reaction. Depending on the pressure in the gas and the ion species, it might be possible to measure both reaction products instead of one. All the aforementioned features allow for a potentially better resolution compared to thick solid targets. The resolution will essentially depend on how accurate the tracks can be reconstructed and the vertex position be determined.

Detector geometry

In Figure 2.4 the geometry of the gas chamber can be seen. All the detecting components, i.e. the MICROMEGAS (which will also be referred to as the *padplane*) [73], DSSDs, Maya detectors and the Diamond detector are indicated. They will be discussed in detail in the following sections. The beam enters from the left and first passes through the mylar window. Then the beam first has to pass through 50 mm of gas before reaching the area covered by the field cage. This cage contains the electric field needed to allow the electrons to drift to the bottom where the MICROMEGAS, which serves as the segmented plane, is located. The cage is also used to eliminate the influence from stray fields from outside the cage. Tracks can only be measured in the area covered by the MICROMEGAS. Note however that if the vertex point of the reaction lies before the MICROMEGAS area, this point can still be reconstructed if proper tracks are found.

From Figure 2.4 it is also clear that the detection efficiency in the auxiliary detectors varies depending on the position of the vertex. Both the Diamond detector and the pillars of the field cage can block the particles. The result is that at certain positions, particles scattering at certain angles can not be detected. There is also a gap between the DSSDs and the Maya detectors. In a similar way as the previous case, this results in a lowering of the efficiency. More problems concerning the geometrical efficiency will be discussed in Chapter 4.

Between the right side of the field cage and the right Maya detectors a source can be mounted for calibration purposes. This source can be rotated 360° and moved up and down such that it does not block particles during actual measurements. There is the possibility to mount a second calibration source at the back of the Diamond detector so get a good coverage of all DSSDs.

2.3.2 The gas medium

The choice of the gas used in the detector and the pressure of this gas is determined by the physics case one wants to study. However, in this choice the good operation of the detector as a whole has to be considered [74]. For the present experiment, the choice to use a He:CO₂ 90:10 gas mixture was made. 90:10 refers to the gas composition in volumetric percentage. The gas mixture was kept constant via a gas mixer. Unfortunately, this

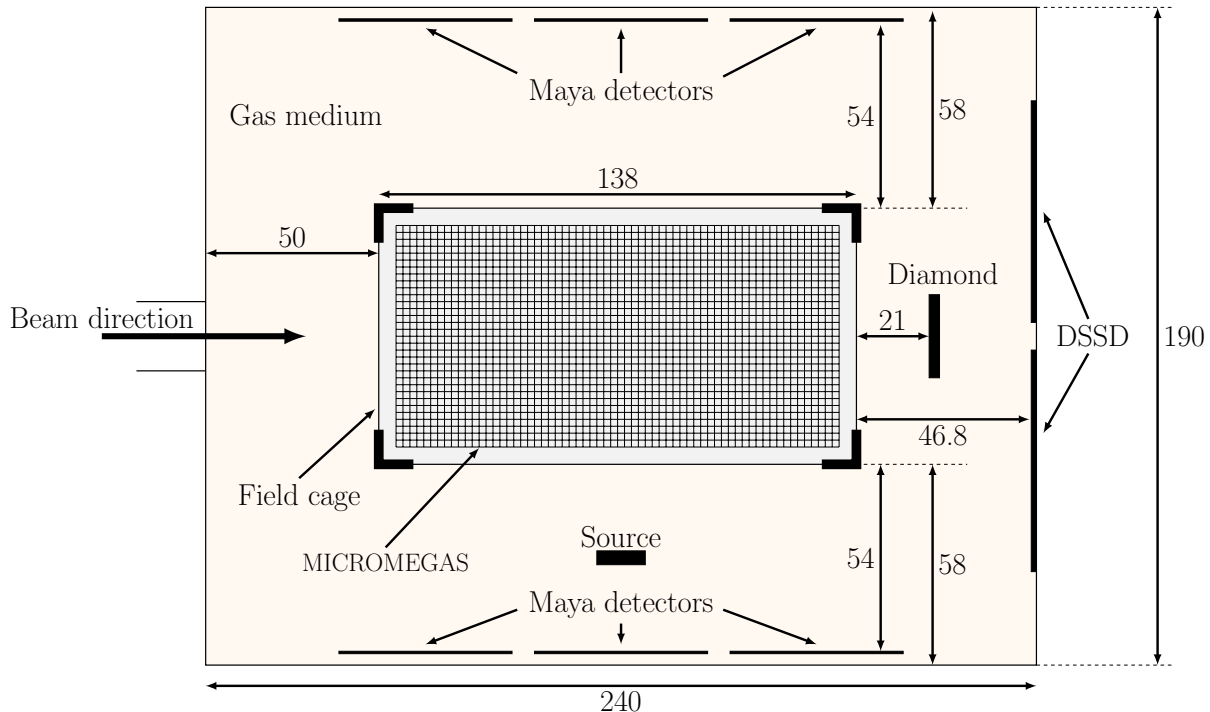


Figure 2.4: Schematic of the gas chamber as seen from above. The various detecting components are indicated and the relevant dimensions are given. The thick black lines at the corners of the field cage indicate the pillars of the cage. The numbers are in milimeters. The distance between the field cage and the sides of the MICROMEGAS is 5 mm.

gas mixer did not work properly during the experiment. Additional measurements⁸ have shown that the actual amount of CO₂ was 5±1 V%. This composition has been used during the analysis of the data.

The helium atoms are the actual target particles in this setup. Mixing CO₂ into this helium gas was done for two purposes. First, the gas is used as a quencher gas. If the ion does not ionize but excites one of the gas atoms or molecules, photons might be created through the decay of these atoms or molecules. The photons can also lead to the ionization of the gas which might degrade the good proportionality. Quencher gases are used to deal with this [71]. Second, the addition of CO₂ increases the drift velocity of the electrons. The drift velocity needs to be high enough such that the system can deal with the high rate of particles inducing reactions. The pressure of the gas inside the detector was 1001 mbar which corresponds to a gas density of 0.245 mg/cm³ and 2.514·10¹⁹ ⁴He nuclei/cm³.

As mentioned in the preceding section, the energy loss can be calculated by measuring the range of the ion in the gas. Figure 2.5 shows the energy of the ⁶Li particle as a function of the length traversed in the gas. Note that this single curve can be used for multiple starting energies (see the caption of Figure 2.5). It can be seen that for the lowest beam energy (11.5 MeV), the beam will never reach the DSSDs since the length of the gas chamber is 240 mm (see Figure 2.4).

⁸The author of this text was not present during these measurements, nor did he contribute to its data analysis.

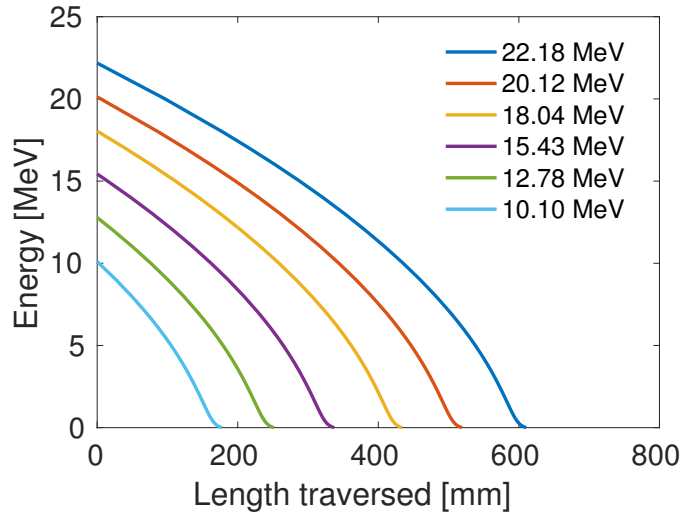


Figure 2.5: Plot with the energy of the incident ${}^6\text{Li}$ versus its length traversed in the gas. The calculation was performed for a He:CO₂ 95:5 gas at a pressure of 1001 mbar and a temperature of 295.15 K. The initial energies correspond to a beam particle which has just exited the Mylar foil (see Table 2.1).

2.3.3 The auxiliary detectors

The Double Sided Silicon Detectors (DSSDs)

In order to measure the energy of the ions which can not be stopped in the gas volume, silicon detectors are the most interesting choice in terms of stopping power and energy resolution [71]. During the present experiment Double Sided Silicon Detectors [75] (DSSDs) have been used. A schematic view of this type of detector can be seen in Figure 2.6. This type of detector employs strip electrodes on both sides. The strips on the backside of the detector are oriented orthogonal to the front side strips. A configuration like this creates a segmented silicon detector which allows to determine the impact point on the detector in x - and y -directions.

The segmentation of the detector is needed to treat cases in which multiple particles go to the same silicon detector. This could for example be the case if one of the particles experiences a breakup or when a beam particle is present within the same time window of the reaction event. Each pixel of the DSSD then corresponds to one of the particles with its own measurement of the energy. An additional advantage of using this type of detector is that once the vertex position of the reaction is known, it provides a way to determine the angle of the reaction of the particle. This can be compared to the angle resulting from the fitting of the tracks.

The DSSDs used in this experiment⁹ consisted of 32 strips on each side¹⁰. The pitch of the strips is 2 mm resulting in a detection area with a total size of 64×64 mm². Four DSSDs are present in the detector in a 2×2 arrangement. The distance between the DSSDs was 8 mm¹¹ and is due to the frame around each DSSD containing the active

⁹Developed by Micron Semiconductor.

¹⁰In what follows, the strips will be labeled by numbers 0 to 31 for the front side and numbers 32 to 63 for the back side.

¹¹This distance is for example visible on Figure 2.4 for the two upper DSSDs.

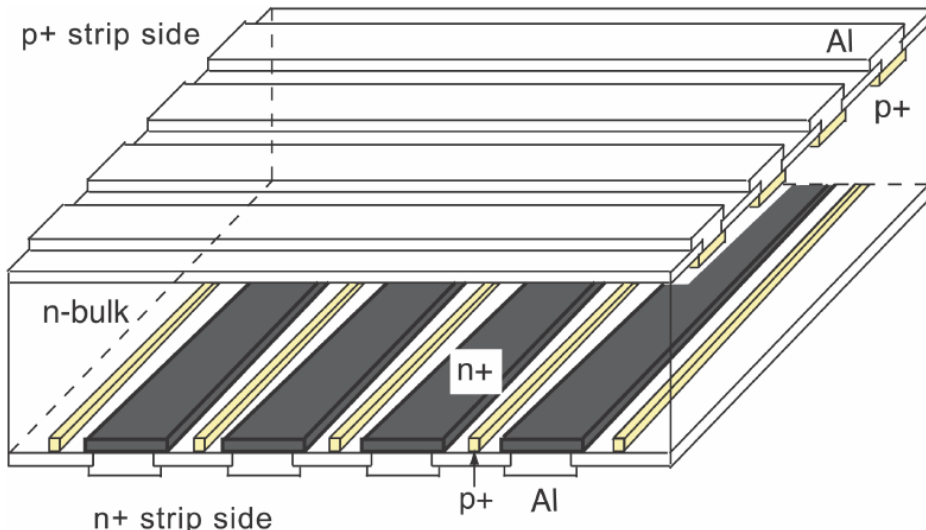


Figure 2.6: Schematic figure of a DSSD. More information on DSSDs can be found in books treating radiation detection such as References [71, 75]. Figure from [76].

area. The detectors are $1700\text{ }\mu\text{m}$ thick. Each strip has to be treated independently by the electronics. In total this configuration results in 256 electronic channels.

The Maya detectors

On each side of the detector, six more silicon detectors¹² are present to stop particles which scatter at large angles and are not stopped in the gas volume. The detectors are arranged in a 3×2 configuration. The distance between each of the detectors is 6 mm^{13} . Each of the detectors is $50\times 50\text{ mm}^2$ in size and $700\text{ }\mu\text{m}$ thick. In total, this configuration results in an additional 12 electronic channels.

These detectors will not be able to give precise information related to the hit position of the particle on the detector. This is however, less of an issue compared to case where the particle scatters at forward angles. First of all, the beam can never reach these detectors. This eliminates the possibility of measuring multiple particles, of which one is a beam particle, with the same detector within the time window of one event. Secondly, doing a correction of the fitted reaction angle is of less importance. Due to the larger scattering angles, the vertex position will be less influenced by an error on the fitted angle. **check statement**

The Diamond detector

The Diamond detector is a plastic scintillator **Seem to recall this, but did not find any documentation** which serves as the beAMDumb. This beAMDumb is needed to protect the other parts of the detector, especially the DSSDs from getting damaged related to the constant bombardment from the beam. No energy information is recovered from this detector. However, it can be used to get a measure of the beam intensity. The size of

¹²These are Passivated Implanted Planar Silicon (PIPS) detectors manufactured by Canberra.

¹³Once more, see Figure 2.4 for the three upper Maya detectors.

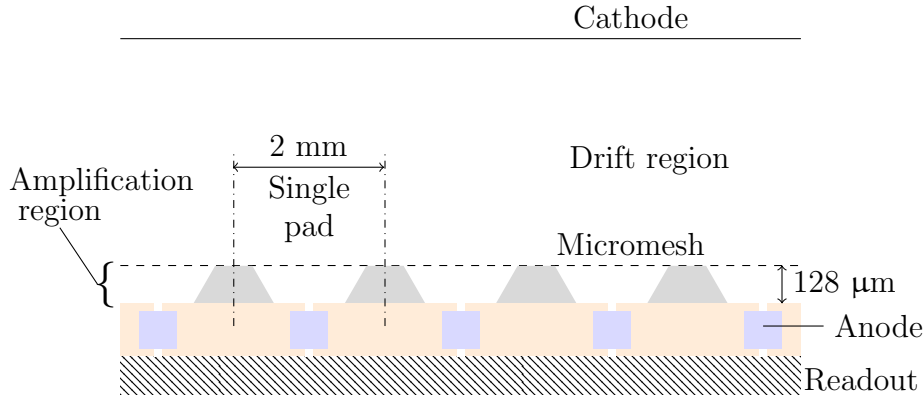


Figure 2.7: Conceptual cross sectional view of the MICROMEGAS. The grey trapeziums are pillars which keep the Micromesh in place. The charge is multiplied in the amplification region and collected on the anodes. The signal is then transported through the readout connectors.

the detector is $24 \times 24 \text{ mm}^2$, with an active area of 2.70 cm^2 . Note however that particles scattering at small angles can also potentially be blocked by this detector. Unless sufficient information can be extracted from the other scattered particle or particles, these events are lost. This leads to a decrease of the geometrical efficiency. The Diamond detector was operated at -300 V.

2.3.4 MICROMEGAS

Detection of the tracks is done with the Micromegas (MICRO-MEsh-GAseous Structure) technology [73]. The Micromegas allows for an amplification of the signal produced by the ionization of the gas. Compared to traditional charge amplification technologies used in gaseous mediums, the MICROMEGAS technology allows to perform measurements with a higher spacial resolution, while also maintaining the ability to deal with high trigger-rates.

The basic idea of MICROMEGAS is shown in Figure 2.7. A metallic mesh of 5 μm thickness which separates the drift region of the electrons from the amplification region is used. The width of the amplification region is 128 μm . The anode collecting the charges is segmented into pads with a pitch of 2 mm. The surface of the anode is close to the amplification region such that they can not drift into the regions covered by the neighboring pads. There is however diffusion of the electrons present in the drift region such that one track still might fire multiple neighboring pads. Through a fitting procedure, this actually allows for a spatial resolution which is smaller than 2 mm [77]. Each pad has to be treated independently by the electronics.

The segmented plane was $128 \times 64 \text{ mm}^2$ which corresponds to a 64×32 configuration of the pads. In total this results in 2048 separate electronic channels. The voltages at which the micromesh and anode were operated was not constant in each run of the experiment. Typical values were -411 V and -388 V for the micromesh and anode respectively. This corresponds to an electric field strength of 257 kV/cm inside the amplification region. Such a high field strength is needed do deal with the dynamic range¹⁴ needed to detect

¹⁴The dynamic range is defined as the ratio between the largest and smallest detectable charge in the

Table 2.2: Table with the possible decay energies for each of the isotopes on which the calibration source is based. Energies are found from Reference [28].

Source	Energy (keV)	Branching ratio (%)
^{239}Pu	5105.50	11.94
	5144.30	17.11
	5156.59	70.77
^{241}Am	5442.80	13.1
	5485.56	84.5
^{244}Cm	5762.64	23.1
	5804.77	76.9

the three different species in the experiment, namely ^6Li , ^4He and d . In principle, a higher field strength and hence amplification would lead to an increase of the dynamic range. However, this would lead to problems such as sparking in the MICROMEGAS. Row 14 up to 18 of the pads were masked with an aluminum foil. This was done to prevent the beam from being measured. Such a measure was needed to protect the MICROMEGAS and to prevent triggering too much events in which no nuclear reaction had taken place. Note however that there was still the possibility that some pads were fired due to the drift of the electrons to pads outside the mask. In some case, electrons also drifted under the foil such that pads in the masked area were fired.

2.3.5 Calibration source

During the experiment additional measurements were performed to calibrate the several detector components mentioned in the previous sections. For this purpose a triple α source composed of ^{239}Pu , ^{241}Am and ^{244}Cm was used. These kind of measurements could be performed in a vacuum such that the total α decay energies could be measured by the silicon detectors. The padplane could be calibrated by filling the chamber with a gas and comparing the simulated energy loss at the several positions of the pad plane with the measured charged. Each of the three isotopes has multiple possible α decay energies. These are listed in Table 2.2 together with their respective branching ratios.

2.4 GET electronics

Due to the large number of electronic channels involved (2316 in total) and the large trigger rate needed in the measurement, specialized electronics are required. For this reason the GET (Generic Electronic system for TPCs) electronics[78] have been developed and employed in this setup. The structure of GET can be seen in Figure 2.8. Only the basic structure and capabilities of GET will be explained here. For a full description of the GET electronics, see References [78–80]. The discussion below is based on those references. Signals coming from the detector components are send through protection circuit cards which are called ZAP cards. The ZAP cards are connected to the front-end AsAd (ASIC¹⁵ support and Analog-Digital conversion) cards. Each AsAd is composed of

gas medium [64].

¹⁵ASIC stands for Application Specific Integrated Circuit.

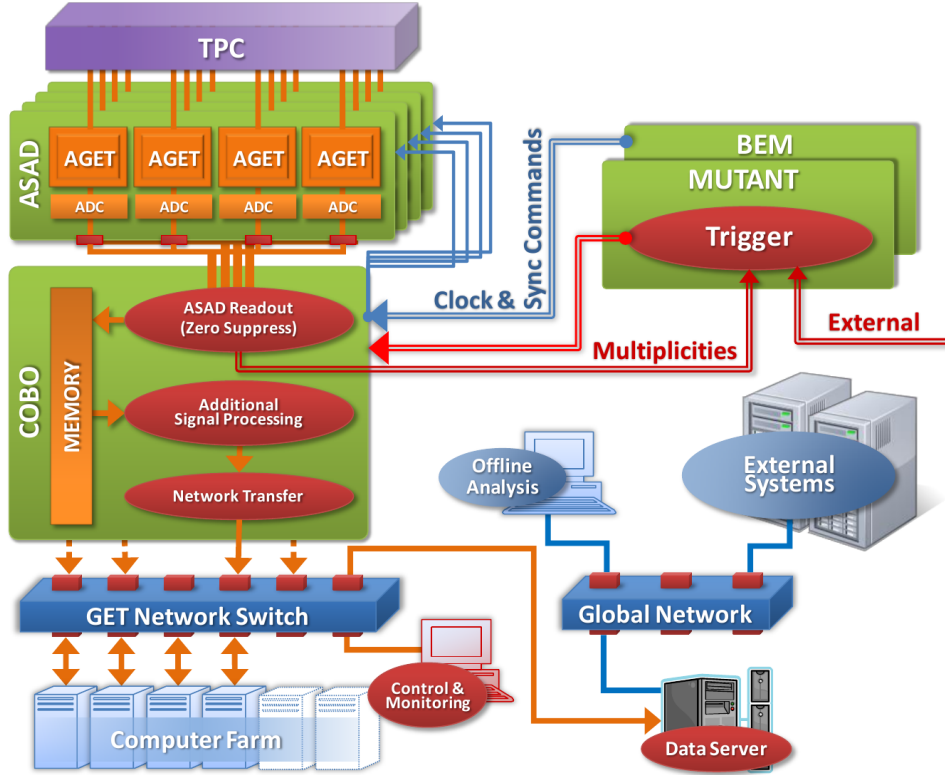


Figure 2.8: General setup of the GET electronics. Figure taken from [80].

four AGET (ASIC for GET electronics) chips, each with its own 12-bit ADC¹⁶ converter. Each of the AGET chips has 64 electronic channels and each of these channels integrate a charge sensitive preamplifier and a signal shaper. The preamplifier can be set to use four different gains. Additionally, its memory is based on a Switched Capacitor Array (SCA) structure with 512 cells. The sampling frequency of the SCA was set to 100 MHz. The AsAd boards also have built-in pulsers which can be used for testing and calibrating the detector. Furthermore in case of a malfunction alarm flags are automatically set. A Concentration Board (CoBo) can be used to collect the information coming from four different AsAd cards. Additionally the CoBo can be used for applying time stamps and zero suppression and it serves as the main communication channels between the AsAd cards and the computers. A μTCA is housing the CoBo. The MuTAnT (Multiplicity Trigger And Time) card is used to manage the triggers needed during the measurement. The MuTAnT card is connected to the CoBo which can transit the trigger signals to the AsAd. Multiple trigger mechanisms are available. An external trigger can be provided through the BEM (Back End Module). Triggers based on time- or event- pattern recognition can also be used. The triggering can be done through the various detectors (the MICROMEGAS or silicon detectors).

The present setup used four CoBos. Two of the CoBos were connected to four AsAd cards each and used to process the signal of the MICROMEGAS. The two other CoBos were connected to only one AsAd card and used to process the signal of the DSSDs and the twelve Maya Detectors. The ten AsAd Cards provided a total of 2560 electronic channels. Signals coming from the several detector components were shaped through the

¹⁶ADC stands for Analog to Digital Converter. For general information on this type of device, see [71].

RC^2 filter¹⁷ integrated in the AGET chips. For most of the runs, the triggering was done on the CoBos related to the MICROMEGAS and the signal in the DSSDs. Some runs only used triggering from the MICROMEGAS.

¹⁷More information on filters can be found in several books, e.g. Reference [71].

Chapter 3

Nuclear reaction theory

In this chapter the basic theory of nuclear reactions will be developed. The focus will be on resonant reactions. This chapter is mostly based on the books by Satchler [81], Hodgson [82] and Burcham [83]

3.1 Terminology

In nuclear reaction experiments one accelerates a particle a which collides with a particle A which is typically at rest. The result of the reactions are the *reaction products* b and B . Such a reaction can be written in the following way:

$$a + A \rightarrow b + B.$$

An often used shorthand notation for this is $A(a, b)B$. The reaction products can be in their ground state or can be in an excited state. Each combination of b and B is referred to as a *exit channel*. Combinations of the reaction products in which an excited state is involved is also considered as a separate channel. Similarly the combination a and A is referred to as the *entrance channel*. The shorthand notation invites to use the notation (a, b) to refer to a general class of reactions which can take place. An example is the scattering of a proton on a heavy target which results in the emission of a target-like recoil particle with one neutron less and a deuteron. This kind of reaction is then denoted as a (p, d) reaction.

Not all combinations of entrance and exit channels are always possible. The possibility of the occurrence of a specific reaction is determined by the physical quantities which are conserved. First of all, there is a conservation of the nucleon numbers. This means that the number of protons and neutrons in the entrance channel must always equal the number of protons and neutrons in the exit channel. This does not imply that mass is conserved. This is only the case when the exit and entrance channel are exactly the same. There is however a conservation of energy and momentum. This implies that the following must hold [2]:

$$E_{k,f} = E_{k,i} + Q, \quad (3.1)$$

where $E_{k,f}$ and $E_{k,i}$ are the total kinetic energies of the final and initial sets of particles respectively and Q is the *Q-value* of the reaction. The Q-value is defined as

$$Q = (m_i - m_f)c^2, \quad (3.2)$$

where m_i and m_f are the total masses of all initial and final particles combined respectively. c is the speed of light. From Equations (3.1) and (3.2) it is clear that mass is indeed not conserved. Instead, when Q is positive, the additional energy is distributed over the particles of the exit channel as kinetic energy. This is an *exoergic* reaction. On the other hand, if Q is negative, additional energy is needed to compensate for the additional mass in the exit channel. These are *endoergic* reactions and can only be initiated if the total energy in the center of mass of the initial particles is higher than the Q -value. Note that when one of the reaction products is in an excited state, one has to subtract the excitation energy needed to reach the excited state from the Q -value. The actual Q -value is then $Q_{ex} = Q - E_{ex}$, where E_{ex} is the excitation energy.

There is also conservation of angular momentum. Defining $\mathbf{I}_A, \mathbf{I}_a, \mathbf{I}_B$ and \mathbf{I}_b as the nuclear spins of the initial and final particles and ℓ the angular momentum transferred in the reaction, one has

$$\mathbf{I}_a + \mathbf{I}_A + \ell = \mathbf{I}_b + \mathbf{I}_B. \quad (3.3)$$

During the reaction, the parity π must also be conserved. Defining π_a, π_A, π_b and π_B as the parity of the initial and final particles, one has

$$\pi_a \cdot \pi_A \cdot (-1)^\ell = \pi_b \cdot \pi_B. \quad (3.4)$$

A last quantity which can be important is the isospin [2]. The isospin is fictitious ‘spin’ used to distinguish protons and neutrons when they are treated as if they were a single particle, the nucleon. The z -component of the isospin t of the proton is equal to $\frac{1}{2}$ and for the neutron it is equal to $-\frac{1}{2}$. Then a total isospin \mathbf{T} can be assigned to each state of the nucleus. Isospin is only an approximately conserved quantity. This means that reactions which do not conserve isospin can occur, but the probability is diminished. The conservation of angular momentum, parity and isospin can be used to determine the spin-parity of the populated states of the reaction products. This is done through the measurement of the cross section which highly depends on ℓ . Determination of ℓ and knowledge of the I^π of the states of the initial particles allows for the determination of the I^π of the states of the reaction products.

Depending on the Q -value of the reaction, the kinetic energy of the incident particle and the structures of the nuclei involved, two broad types of reactions can occur, *direct* and *compound nucleus* reactions. The two reaction mechanisms are depicted in Figure 3.1. The probability that the reaction goes through either mechanism depends on the parameter \mathcal{B} , which is defined as the perpendicular distance between the initial path of the incoming particle and an axis through the center of the target nucleus. If \mathcal{B} is similar to the radius R of the nucleus, direct reactions have a higher probability of occurring. Then only the outer nucleons of the target nucleus take part in the reaction. If \mathcal{B} is much smaller than R , compound nucleus reactions are more likely to occur. In this type of reaction, the initial nuclei merge together and form an intermediate state. This compound nucleus is typically in a highly excited state. After some time, the compound nucleus decays such that the reaction is finished. The reaction time of direct reactions is of the order of 10^{-22} s. Due to the fact that an intermediate state is formed in which there are a lot of interactions between the many nucleons, the reaction time is longer in the case of a compound nucleus reaction, namely of the order of 10^{-15} s. The many interactions also causes the compound system to emit the reaction products more or less

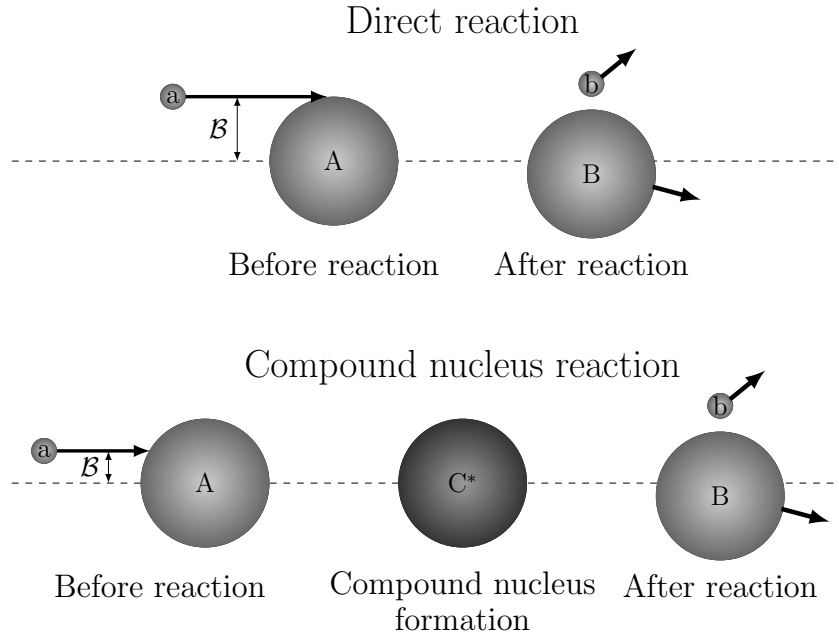


Figure 3.1: Schematic representation of the two broad classes of reactions. Note that the impact parameter \mathcal{B} is smaller in the compound nucleus mechanism. During direct reactions, no intermediate state is formed. The figure was inspired by Figure 2.28 of Reference [81].

isotropically¹. It can be expected that this description works better for heavier systems [83]. Generally the *independence hypothesis* also holds which states that the probability to have the compound system decay through a specific channel is independent the way the compound system was formed. In comparison, the angular distribution in the case of a direct reactions varies much stronger with angle [2]. The tendency to proceed through either reaction mechanism also depends on the energy of the incident particle. When the energy increases, the probability to proceed through direct reactions increases. When an exit channel opens in which one of the reaction products is a charged particle, the probability to proceed through a compound nucleus reaction suddenly decreases. This is due to the fact that a reaction in which a charged particle is emitted has to deal with the Coulomb barrier of the compound nucleus. Note however, that at all times the two reaction mechanisms are not mutually exclusive [82].

Several reaction subtypes exist. *Elastic* scattering is a process in which the entrance and exit channels are the same. Consequently the Q -value of the reaction is 0. The *inelastic* scattering process is similar, but one (or more) of the reaction targets is in an excited state. During a *stripping* reaction, one or more nucleons are transferred from the target to the incident particle. When the opposite happens, namely one or more nucleons are transferred from the incident nucleus to the target nucleus, the reaction is called a *pick-up* reaction. The last two are collectively known as *transfer* reactions.

¹In this case the energy-averaged angular distribution in the center-of-mass frame is meant.

3.2 Basic formalisms

Useful property that can be used to quantify nuclear reactions is the *cross section* σ of the reaction. Referring to the generic reaction $A(a, b)B$, its cross section can be defined as [2]

$$\sigma = \frac{R_b}{I_a N_A}, \quad (3.5)$$

where R_b is the number of particles b emitted per unit time, I_a is the number of incident particles a per unit time and N is the number of target nuclei A per unit area. σ can be interpreted as the probability of a reaction occurring through an exit channel involving particles b and B when the entrance channel involves particles a and A . Similar definitions of the cross section can be used for reactions using the same entrance channel, but different exit channels. Summing the cross section of all possible exit channels results in the *total cross section*. Note that even though the interpretation of the cross section is one of probability, its dimensions are those of an area. Typically the unit *barn*² is used. Related quantities are the *energy spectrum* $d^2\sigma/d\Omega dE$, the *differential cross section* $d\sigma/d\Omega$ and the *excitation function* $d\sigma/dE$ [84]. The energy spectrum gives the cross section for finding the particle b inside a solid angle Ω at an energy E for a given initial energy of the incident particle a . Through an integration of the energy of the b particles the differential cross section is found. In the literature, the energy spectrum at discrete sets of energies (for example in the case of excitation states) are often also referred to as the differential cross section $d\sigma/d\Omega$. The excitation function is found through an integration of the whole solid angle. Similar to the other quantities, it gives the probability to find the particle with an energy E at any angle. After a measurement, one wants to compare the measured cross sections with theory in order to interpret the results. For this reason, the basics of nuclear scattering will be presented below.

3.2.1 Nuclear scattering theory

This section will present the general theory of nuclear scattering. It will more or less follow the structure of References [82] and [81]. Some additional information was found in Reference [83]. First only spinless neutral particles will be treated. The theory will afterwards be adapted for particles with charge, spin, and the internal degrees of freedom of the nuclei.

Elastic scattering of neutral spin-less particles

To describe elastic scattering, the appropriate Schrödinger equation must be solved:

$$\nabla^2\psi + \frac{2m}{\hbar^2} (E - V(r)) \psi = 0, \quad (3.6)$$

where $V(r)$ is a real potential, E and m the energy and mass of the particle and ψ the wavefunction of the particle. Initially, the wavefunction can simply be represented by plane waves. Choosing the z -axis as the initial direction of the incident particle, the wavefunction of the particle before the reaction is given by

$$\psi_{in} = A e^{ikz}, \quad (3.7)$$

²The symbol of the barn is b. 1 b = 10^{-24} cm²

where A is a normalization factor and k the wave number given by $\sqrt{2mE}/\hbar$. Solutions of Equation (3.6) will be wavefunctions which are partially spherical in nature but also asymptotically, i.e. for large r , plane waves:

$$\psi = \psi_{in} + \psi_{out} = A \left(e^{ikz} + \frac{e^{ikr}}{r} f(\theta) \right), \quad (3.8)$$

where $f(\theta)$ is the *scattering amplitude*. Note that Equation (3.8) only strictly holds when the Coulomb interaction is absent. If this is not the case, the interaction potential essential extends to infinity, which distorts the wavefunction [81]. In the following, the Coulomb interaction will be neglected and a correction will be discussed below. It can be shown that³

$$\frac{d\sigma}{d\Omega} = |f(\theta)|^2. \quad (3.9)$$

The goal is thus to find an appropriate form for $f(\theta)$. This can be achieved through the partial wave expansion. This method assumes that the complete wavefunction is a superposition of wavefunctions with orbital angular momenta $L = 0, 1, 2, \dots$. The wavefunction is then factorized in an angular and radial part:

$$\psi = \sum_L \frac{u_l(r)}{r} P_L(\cos \theta), \quad (3.10)$$

where $u(r)$ are the radial wavefunctions and $P_L(\cos \theta)$ Legendre polynomials of degree L and θ is the angle. Similarly, e^{ikz} can be expanded as

$$e^{ikz} = \sum_{L=0}^{\infty} (2L+1) i^L j_L(kr) P_L(\cos \theta), \quad (3.11)$$

where $j_L(kr)$ are the Bessel functions of the first kind. The use of the partial wave expansion modifies Equation (3.6):

$$\frac{d^2 u_L}{dr^2} + \left[\frac{2m}{\hbar^2} (E - V(r)) - \frac{L(L+1)}{r^2} \right] u_L = 0. \quad (3.12)$$

This equation can be solved to find an expression for $u_L(r)$. To do so, one can assume that $V(r)$ only has nuclear characteristics⁴ so that it becomes zero for large r . The term proportional to r^{-2} also becomes negligible for large r . By writing

$$\psi_{out,L} = \frac{u_L(r)}{r} - \psi_{in,L}, \quad (3.13)$$

and considering Equation (3.11), an expression for the outgoing wave with angular momentum L can be found:

$$\begin{aligned} \psi_{out,L} &= \frac{A e^{-i\delta_L}}{2ir} \left(e^{2i\delta_L} e^{i(kr - \frac{1}{2}L\pi)} - e^{-(kr - \frac{1}{2}L\pi)} \right) P_L(\cos \theta) \\ &\quad - (2L+1) \frac{i^L}{2ikr} \left(e^{i(kr - \frac{1}{2}L\pi)} - e^{-i(kr - \frac{1}{2}L\pi)} \right) P_L(\cos \theta). \end{aligned} \quad (3.14)$$

³See for example Reference [85].

⁴The Coulomb interaction is once more explicitly neglected.

In the previous equation δ_L represents a *phase shift*. Notice also that terms of the form e^{-ikr} are present. These represent ingoing spherical waves and must be eliminated. This can be achieved by setting

$$A \frac{e^{-i\delta_L}}{2ir} = -(2L+1) \frac{i^L}{2ikr}. \quad (3.15)$$

Eventually, by comparing Equations (3.8) and (3.14) one can find an expression for $f(\theta)$:

$$f(\theta) = \frac{1}{2ik} \sum_{L=0}^{\infty} (2L+1)(e^{2i\delta_L} - 1) P_L(\cos \theta). \quad (3.16)$$

In this expression the scattering matrix element can be defined as

$$S_L = e^{2i\delta_L}. \quad (3.17)$$

Generalization of the theory

The expression of $f(\theta)$ was derived by assuming that only the elastic channel was present. The internal degrees of freedom of the nuclei involved were also not considered. Assume a general reaction of the form $A(a, b)B$. The entrance channel can be indicated as α and the exit channel as β . To include the internal degrees of freedom, the incident wavefunction of Equation (3.7) must be modified, namely

$$\psi_\alpha = A e^{i\mathbf{k}_\alpha \cdot \mathbf{r}_\alpha} \varphi_a \varphi_A, \quad (3.18)$$

where \mathbf{k}_α and \mathbf{r}_α represent the relative momentum and position between particles a and A and φ_a and φ_A their internal wavefunctions. Both φ_a and φ_A are normalized to one. The latter wavefunctions also include properties such as spin and state of the nuclei. The outgoing wave will resemble the form of Equation (3.8), namely

$$\psi_{out} = A \left(e^{i\mathbf{k}_\alpha \cdot \mathbf{r}_\alpha} \varphi_a \varphi_A + \sum_{\beta} f_{\beta}(\theta, \phi) \frac{e^{i\mathbf{k}_{\beta} \cdot \mathbf{r}_{\beta}}}{r_{\beta}} \varphi_b \varphi_B \right). \quad (3.19)$$

In the previous equation $f_{\beta}(\theta, \phi)$ has once more the interpretation of the scattering amplitude. Note however that now it is defined for each exit channel separately and the dependence on the azimuthal angle has been made explicit **can probably be said better**. Equation (3.9) can then be generalized to

$$\frac{d\sigma_{\beta}}{d\Omega} = \frac{v_{\beta}}{v_{\alpha}} |f_{\beta}(\theta, \phi)|^2, \quad (3.20)$$

where $\frac{v_{\beta}}{v_{\alpha}}$ is the ratio of the relative velocities of the exit and entrance channel. When this fraction is equal to 1, the elastic scattering cross section of Equation (3.9) is found again.

To treat the scattering problem further, the Schrödinger equation which has to be modified such that it can account for the internal components in the system. Denoting H_a and H_A as the internal Hamiltonians such that $H_a \varphi_a = E_a \varphi_a$ and $H_A \varphi_A = E_A \varphi_A$, Equation (3.6) is generalized to

$$\nabla_{\alpha}^2 \psi + \frac{2\mu_{\alpha}}{\hbar^2} (E - H_a - H_A - V_{\alpha}(r)) \psi = 0, \quad (3.21)$$

where μ_α is the reduced mass of the system⁵. One can now expand the incident wavefunction according to the several excited states of a and A . One finds:

$$\psi_\alpha = \sum_{a'A'} \chi_{a'A'}(\mathbf{r}_\alpha) \varphi'_a \varphi'_A, \quad (3.22)$$

where $\chi_{a'A'}(\mathbf{r}_\alpha)$ denotes the plane wave part of the wavefunction. Using this expansion, one can write Equation (3.21) as

$$[\nabla_\alpha^2 - U_{aA,aA}(\mathbf{r}_\alpha) + k_{aA}^2] \chi_{aA}(\mathbf{r}_\alpha) = \sum_{a' \neq a} \sum_{A' \neq A} \chi_{a'A'}(\mathbf{r}_\alpha) U_{aA,a'A'}(\mathbf{r}_\alpha), \quad (3.23)$$

where

$$\begin{aligned} U_{aA,a'A'} &= \frac{2\mu_\alpha}{\hbar^2} \langle aA | V_\alpha | a'A' \rangle, \\ k_{aA}^2 &= \frac{2\mu_\alpha}{\hbar^2} (E - E_a - E_A). \end{aligned} \quad (3.24)$$

The diagonal matrix elements $U_{aA,aA}$ on the left hand side of Equation (3.23) represent the elastic channels, the off-diagonal matrix elements $U_{aA,a'A'}$ on the right hand side of the equation represent the inelastic channels. It is clear that all possible elastic and inelastic channels are coupled through Equation (3.23). Hence, they are called *coupled equations*. If all matrix elements can be calculated, the equation can in principle be solved. In practice however, there are an infinite number of terms which have to be considered. This necessitates the use of a truncation of the sum. Such a truncated sum can then be treated theoretically if an appropriate model is used for V_α . An example is the *optical model* which is also often used in practice.

The general form of $f_\beta(\theta, \phi)$ can be found in a similar way as described in the previous section. The most general way to expand the ingoing wave function into partial waves is⁶

$$\chi(\mathbf{r}_\alpha) = \sum_{L,M} \chi_{LM} = \sum_{L,M} c_{LM} u_L(r) Y_L^M(\theta, \phi). \quad (3.25)$$

In this case the z -projection of \mathbf{L} is indicated by the quantum number M . The function $Y_L^M(\theta, \phi)$ is a spherical harmonic [8] and c_{LM} are weight coefficients which depend on the combination of L and M . Note that if one chooses the z -axis such that \mathbf{k}_α is oriented along this axis, $M = 0$. The radial part of the Schrödinger equation will essentially be the one in Equation (3.12) in which u_L is replaced by χ_{LM} and m by μ_α . Solving the equation analogously as before, one eventually finds

$$f_\beta(\theta, \phi) = \frac{1}{2ik_\alpha} \sqrt{\frac{v_\alpha}{v_\beta}} \sum_L (2L+1) [S_{L,\beta} - \delta_{\alpha\beta}] P_L(\cos \theta). \quad (3.26)$$

In the previous equation $\delta_{\alpha\beta}$ is the Kronecker delta which is equal to 0 if the entrance and exit channels are different, and gives 1 if they are the same. $S_{L,\beta}$ has the same interpretation as before, but for all possible exit channels. To allow for the conservation of flux of the partials, the S -matrix must be unitary, i.e.

$$\sum_\beta |S_{L,\beta}|^2 = 1. \quad (3.27)$$

⁵Equation (1.37) can be used for this purpose in which 1 = a and 2 = A . A more accurate definition is to use the masses explicitly instead of the nucleon numbers. In that case m_N falls out of the equation.

⁶The integral wavefunctions are not important in this respect.

Modifications due to the Coulomb force

As mentioned in the previous sections, the derivation only holds if the Coulomb force is neglected. In this section, the effects of the Coulomb force will briefly be discussed. The spherical, outgoing wave has to be modified with an additional term due to the Coulomb force:

$$\frac{1}{r} \exp i(k_\beta r - n_\beta \ln(2k_\beta r)), \quad (3.28)$$

where $n_\beta = Z_b Z_{Be}^2 / (\hbar v_\beta)$ in which Z_be and Z_{Be} are the charges of the reaction products. n_β is called the *Sommerfeld parameter*. The scattering amplitude is also modified as follows

$$f_\beta(\theta, \phi) = f_C(\theta)\delta_{\alpha\beta} + f'_\beta(\theta, \phi), \quad (3.29)$$

where $f_C(\theta)$ is the *Rutherford cross section* (For a derivation, see References [2, 81]). Due to the Kronecker delta, it is clear that the Rutherford cross section only contributes to the elastic channel. Moreover, the effect becomes more important at lower incident energies [2]. $f'_\beta(\theta, \phi)$ is the *Coulomb distorted scattering amplitude* and is essentially given by Equation (3.26), but an additional phase factor must be added of the form $\exp(2i\sigma_L)$ in each term. This phase accounts for the Coulomb effects.

3.2.2 Resonances of the compound nucleus

An important feature of compound nucleus reactions is that resonances can occur [82]. Considering a general reaction $A(a, b)B$ in which A is the target and a compound nucleus C^* is formed, a resonance occurs when the sum of the kinetic energy of the entrance channel in the center of mass frame E_α and binding energy S_α released in the formation of C^* is equal to the energy of a state of C^* . This means that the following must hold:

$$E_\alpha + S_\alpha = E_{ex}, \quad (3.30)$$

where E_{ex} is the energy of the excited state. When such a resonance occurs, the cross section of the reaction suddenly increases. All resonances found through the $A(a, b)B$ reaction lie at energies higher than S_α . In this sense, S_α can be interpreted a threshold energy. For low lying states of the compound nucleus, the resonances are typically rather sharp. The sharpness of the resonance is related to the total width Γ of the state (See also Section 1.1.3.). For the low lying states the resonances are also typically far apart such that they can easily be resolved from each other. For these resonances definite quantum numbers I and L can be defined [82]. At higher excitations energies, the resonance become broader and at some point, they start to overlap. It then becomes possible to observe maxima which are not due to a single real resonance, but rather due to a superposition of resonances. Careful analysis has to be done in order to distinguish the two.

Resonant elastic scattering for spinless particles

In order to describe the shape of the resonances one can start by considering the scattering amplitude from Equation (3.29). The resonance is essentially due to the nuclear part of the scattering amplitude such that only the second term of Equation (3.29) is relevant. For simplicity it will be assumed that the scattering occurs at low energies and only the elastic channel is open. The z -axis can also be chosen such that it coincides with the

momentum \mathbf{k} of the incident particle such that all $M \neq 0$ components of the scattering amplitude are zero. In that case, the scattering amplitude of Equation (3.16) can be used (the additional phase factor due to the Coulomb contribution has to be added however). It is clear that the cross section reaches a maximum if $S_L = -1$. This implies that a resonance occurs when $\delta_L = \frac{\pi}{2}$. As the resonances appear as a function of energy, it means that the phase shifts δ_L also must be a function of the energy [82]. This function is not known, but in the region of the resonance, it can be assumed that a linear relationship holds. One then gets

$$\delta_L = \frac{\pi}{2} - (E_0 - E) \frac{d\delta_L}{dE}, \quad (3.31)$$

where E_0 is the resonance energy. The slope $\frac{d\delta_L}{dE}$ will determine the sharpness of the resonance. If the slope is large, this means that the phase shift varies fast with energy such that a sharp resonance is expected. A shallow slope implies that the resonance is broad. Through this relationship, the width Γ can be defined

$$\Gamma = 2 \left(\frac{d\delta_L}{dE} \right)^{-1}. \quad (3.32)$$

Plugging this definition back into Equation (3.31) and using the definition of S_L in Equation (3.17), one finds

$$S_L = \frac{E_0 - E + \frac{i\Gamma}{2}}{E_0 - E - \frac{i\Gamma}{2}}. \quad (3.33)$$

This can be used in the expression of $f(\theta)$ to find an expression for the differential cross section in Equation (3.9). In principle only one of the partial waves results in a resonance. The cross section due to the other partial waves can then essentially be neglected. One finds

$$\frac{d\sigma}{d\Omega} = \frac{(2L+1)^2}{4k^2} \frac{\Gamma^2}{(E_0 - E)^2 + \frac{1}{4}\Gamma^2} P_L^2(\cos \theta) \quad (3.34)$$

and after integration of the whole solid angle

$$\sigma = (2L+1) \frac{\pi}{k^2} \frac{\Gamma^2}{(E_0 - E)^2 + \frac{1}{4}\Gamma^2}. \quad (3.35)$$

This equation is called the *Breit-Wigner* formula [86] for a single isolated resonance for which only the elastic channel is open. It can be seen that a maximum is reached when $E = E_0$, that is, when a resonance is hit. The cross section also increases when the width of the state becomes broader.

Generalization of the theory

Equation (3.35) can be generalized for a generic reaction $A(a,b)B$. One has then to consider the partial widths of both the entrance and exit channels. Moreover, since spin is now involved, a statistical factor has to be added. Denoting once more the entrance and exit channels as α and β , the Breit-Wigner formula becomes

$$\sigma_{\alpha\beta} = \frac{\pi}{k^2} g \frac{\Gamma_\alpha \Gamma_\beta}{(E_0 - E)^2 + \frac{1}{4}\Gamma^2}, \quad (3.36)$$

where Γ_α and Γ_β are the partial widths of the entrance and exit channel, g is the statistical factor related to the spins and orbital angular momenta of the particles involved and Γ is the total width of the resonance as defined by Equation (1.18). The statistical factor g is given by [83]

$$g = \frac{2I+1}{(2s_a+1)(2s_A+1)}, \quad (3.37)$$

where I is the spin of the compound nucleus and s_a and s_A the spins of the incident and target particle respectively. The statistical factor can be understood as follows [83]. In order to form the compound nucleus and find it in a specific excited state, a specific amount of incident orbital momentum \mathbf{L} must be available. The following equation must be satisfied

$$\mathbf{L} + \mathbf{s}_a + \mathbf{s}_A = \mathbf{I}. \quad (3.38)$$

Defining a *channel spin* \mathbf{j} as

$$\mathbf{j} = \mathbf{s}_a + \mathbf{s}_A, \quad (3.39)$$

the following must then hold

$$s_a + s_A \geq j \geq |s_a - s_A|. \quad (3.40)$$

This means that j can either have $2s_a+1$ or $2s_A+1$ distinct values depending on whether $s_a \geq s_A$ or $s_a \leq s_A$. Furthermore, each spin has several z -axis projections⁷. If the system has no particular orientation, this results in the following probability to form a channel spin with magnitude j from spins s_a and s_A :

$$\frac{2j+1}{(2s_a+1)(2s_A+1)}. \quad (3.41)$$

One can now rewrite Equation (3.38) in terms of \mathbf{j} such that one finds

$$\mathbf{L} + \mathbf{j} = \mathbf{I}. \quad (3.42)$$

A completely analogous reasoning can be made as above to find the probability to form the spin I with the channel spin j and orbital angular momentum L :

$$\frac{2I+1}{(2L+1)(2j+1)}. \quad (3.43)$$

In the Breit-Wigner formula of Equation (3.35) a factor $2L+1$ was present. Multiplying this with the two factors of Equations (3.41) and (3.43), one eventually arrives at the correct statistical factor g as seen in Equation (3.37).

Interference effects

According to Equation (3.36), the shape of the resonance should resemble that of a Lorentzian function [81]. However in practice different shapes are sometimes observed. One quite obvious case is that of overlapping resonances. Then multiple Breit-Wigner type functions have to be considered and superimposed.

⁷For a generic spin ℓ with magnitude ℓ , there are $2\ell+1$ possible z -axis projections [8].

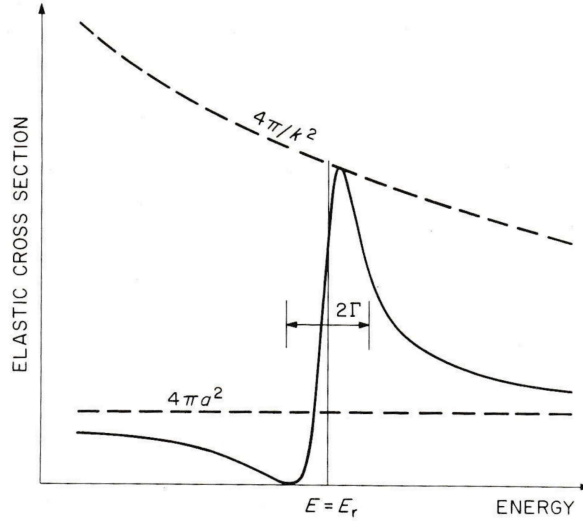


Figure 3.2: Typical shape of a resonance when both resonant and shape-elastic scattering is present. The upper dashed line indicates what the maximum of the resonance could at various energies. This drops off as k^{-2} as indicated by Equation (3.36). The lower dashed line shows the shape-elastic scattering contribution resulting in a flat background. Due to interference of the two types of scattering, a dip in the cross section can be expected. Figure taken from Reference [81].

A more subtle case is that of interference between a background of elastic scattering through direct reactions. The latter type of scattering is also known as *potential-* or *shape-elastic* scattering [83]. The shape of the resonance then typically looks as the one presented in Figure 3.2. Instead of a more or less symmetric behavior, the cross section first experiences a dip before the maximum is reached. The maximum is then no longer exactly at the resonance energy E_0 , but rather at a slightly larger energy.

To understand this effect, one has to consider the S_L matrix element once more. Once shape-elastic scattering is present, the phase shift δ_L can be decomposed in two parts, namely β_L and ϕ_L such that $\delta_L = \beta_L - \phi_L$ [83]. This way, δ_L no longer only represents the resonant behavior. This is instead attributed to β_L . On the other hand, the phase shift ϕ_L specifically represents the shape-elastic scattering. It can now be shown that $f(\theta)$ consists of two parts such that [81]

$$f(\theta) = A_{shape} + A_{res}, \quad (3.44)$$

where A_{shape} and A_{res} represent the shape-elastic and resonant elastic scattering amplitudes respectively. When a square well potential of finite depth is considered⁸ and one assumes that only s -wave ($L=0$) scattering is present, then the two terms are given by [81, 82]

$$\begin{aligned} A_{res} &= \frac{i\Gamma_\alpha}{(E - E_0) + \frac{1}{2}i\Gamma}, \\ A_{shape} &= e^{2i\phi_L}. \end{aligned} \quad (3.45)$$

⁸This type of potential is useful to describe the present interference effects qualitatively. To make accurate comparisons with experimental data, more realistic potentials should be considered [82].

The resonant scattering amplitude can essentially be found the same way as before. When a square well is used to describe the interaction potential one has that $\phi_L = kR$, where R is the radius of the potential. It is clear that using Equation (3.9) and doing the integration for all θ , results in the following:

$$\sigma = \frac{\pi}{k^2} |A_{shape} + A_{res}|^2. \quad (3.46)$$

From this it can be seen that indeed cross terms of the form $2\text{Re}(A_{shape}A_{res}^*)$, where A_{res}^* is the complex conjugate of A_{res} . This is exactly the interference term and changes sign in the vicinity of the resonances, skewing the shape. In this section only *s*-wave scattering was considered. This is sufficient as A_{shape} is typically much smaller for waves of higher angular momentum [81].

3.3 Kinematics of nuclear reactions

The *kinematics* of a nuclear reaction describes at what angles the scattered particles can be expected and how large their kinetic energy. The relations between the angles and energies of the particles are characteristic for the reaction. This way, the kinematics can provide a useful framework to identify particles or even reaction mechanisms.

When the particles of the incident beam are lighter than the target particles, the reaction is referred to as a reaction in *direct* kinematics. If the beam particles are heavier than the target particles, the reaction is referred to as a reaction in *inverse* kinematics. In the center of mass frame, the kinematic formulas are mathematically the same. The type of kinematics will however influence the relations between the scattering angles and the kinetic energies of the particles.

In Section 3.3.1 the most important kinematic formulas will be derived. This will not be done in a relativistic framework. The energies of the particles involved in the experiment concerning this thesis were sufficiently low such that a non-relativistic treatment serve as a good approximation. The general case of inelastic scattering will be treated, but each of the formulas easily reduce to the elastic case if the magnitudes of the velocity vectors in the center of mass frame stay the same after the collision. A fully relativistic treatment of the kinematics can be done be done via an Excel spreadsheet called CATKIN by Catford W. This is freely available online⁹. In Section 3.3.2, these formulas will be applied to the specific case of the ${}^6\text{Li}(\alpha, \alpha'){}^6\text{Li}$ reaction in inverse kinematics. Several plots will be provided.

3.3.1 Two-body kinematics

To describe the scattering of two nuclei, it is convenient to make use of two different reference frames. The *lab frame* is the frame in which actual experiments are performed. The scattering in this frame is shown in Figure 3.3(a). The target is considered to be stationary. In the calculations related to this frame, the following notation will be employed. The velocity vector of the incident particle with mass M is v_{lab}^M . The velocity vectors after scattering has occurred are given by V_{lab}^M and V_{lab}^m for the particles with masses m

⁹For more information, see: <http://personal.ph.surrey.ac.uk/~phs1wc/kinematics/>. Last visited on 21/04/16.

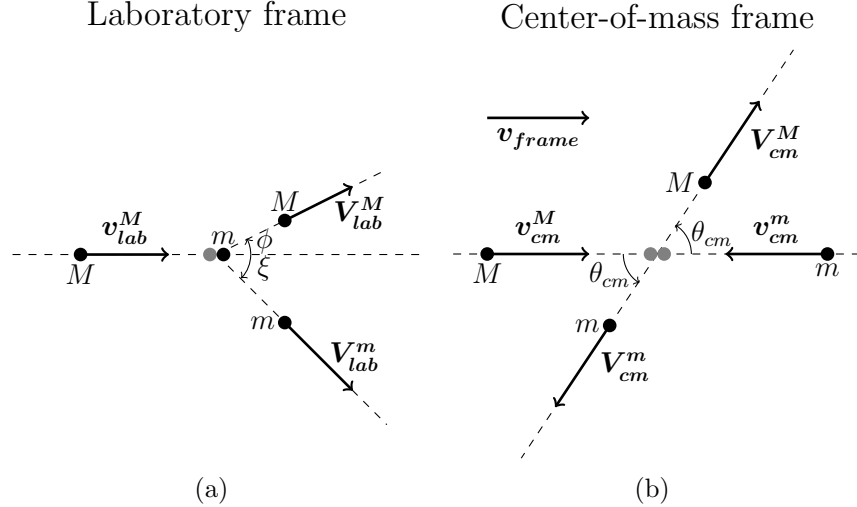


Figure 3.3: Illustration of the (in)elastic scattering process both in the (a) lab frame and (b) center of mass frame. Notice that the center-of-mass frame itself has a constant velocity \mathbf{v}_{frame} .

and M respectively. The scattering angles for those two particles are ϕ and ξ and defined as indicated on the figure. Figure 3.3(b) shows the setup of scattering in the *center of mass frame*. It is clear that now both particles move prior to the reaction with velocities \mathbf{v}_{cm}^M and \mathbf{v}_{cm}^m for the particles with mass M and m respectively. The scattering is now defined by only one angle θ_{cm} such that the two particles always move back-to-back after scattering. Their velocities are then \mathbf{V}_{cm}^M and \mathbf{V}_{cm}^m . The frame itself also move with a constant velocity, namely \mathbf{v}_{frame} . In a two-body scattering process, all trajectories of the particles lie in a single plane. In this section it will be assumed that this scattering plane is the xy -plane.

A basic property of the center-of-mass frame is that the total momentum of the system is zero at all times. This means that

$$M\mathbf{v}_{cm}^M + m\mathbf{v}_{cm}^m = M\mathbf{V}_{cm}^M + m\mathbf{V}_{cm}^m = 0. \quad (3.47)$$

This immediately implies that

$$\mathbf{v}_{cm}^M = \frac{-m}{M}\mathbf{v}_{cm}^m, \quad (3.48a)$$

$$\mathbf{V}_{cm}^M = \frac{-m}{M}\mathbf{V}_{cm}^m. \quad (3.48b)$$

The velocities in both frames can easily be related through the center of mass velocity \mathbf{v}_{frame} . A simple Galilean transformation holds

$$\begin{aligned} \mathbf{v}_{lab}^x &= \mathbf{v}_{cm}^x + \mathbf{v}_{frame}, \\ \mathbf{V}_{lab}^x &= \mathbf{V}_{cm}^x + \mathbf{v}_{frame}, \end{aligned} \quad (3.49)$$

where x can be either m or M . Multiplying Equation (3.49) by m and M when $x = m$ or $x = M$ respectively and adding the two equations, an expression for \mathbf{v}_{frame} can be found

$$\mathbf{v}_{frame} = \frac{M\mathbf{v}_{lab}^M + m\mathbf{v}_{lab}^m}{M + m}. \quad (3.50)$$

Since the target is stationary in the lab frame, the second term on the right hand side of the previous equation drops out and via Equation (3.49) one has that $\mathbf{v}_{frame} = -\mathbf{v}_{cm}^m$. The Galilean transformation between the two frames also suggests that there is relation between the total kinetic energies of the two separate frames. By using Equations (3.49) and (3.50) one finds in the center of mass frame

$$E_{cm}^m = \frac{m(\mathbf{v}_{cm}^m)^2}{2} = \frac{m}{2} \left(-\frac{M}{m+M} \mathbf{v}_{lab}^M \right)^2 = \frac{Mm}{(m+M)^2} E_{lab} \quad (3.51)$$

$$E_{cm}^M = \frac{M(\mathbf{v}_{cm}^M)^2}{2} = \frac{M}{2} \left(\frac{m}{m+M} \mathbf{v}_{lab}^M \right)^2 = \left(\frac{m}{m+M} \right)^2 E_{lab}, \quad (3.52)$$

such that

$$E_{cm}^m + E_{cm}^M = E_{cm} = \frac{m}{m+M} E_{lab}. \quad (3.53)$$

A relationship between the lab angles ϕ and ξ and the center of mass angle θ_{cm} can be found by considering the conservation of momentum. Using Equations (3.49), \mathbf{V}_{lab}^M and \mathbf{V}_{lab}^m can be decomposed in its x - and y - components

$$\mathbf{V}_{lab}^M = (V_{cm}^M \cos \theta_{cm} + v_{frame}) \mathbf{e}_x + (V_{cm}^M \sin \theta_{cm}) \mathbf{e}_y \quad (3.54a)$$

$$\mathbf{V}_{lab}^m = (-V_{cm}^m \cos \theta_{cm} + v_{frame}) \mathbf{e}_x + (-V_{cm}^m \sin \theta_{cm}) \mathbf{e}_y. \quad (3.54b)$$

From this, the relations between the angles in the two frames immediately follow

$$\tan(\phi) = \frac{V_{cm}^M \sin \theta}{V_{cm}^M \cos \theta + v_{frame}} \quad (3.55a)$$

$$\tan(\xi) = \frac{V_{cm}^m \sin \theta}{v_{frame} - V_{cm}^m \cos \theta}. \quad (3.55b)$$

In order to find the speed of the particles in the lab and center of mass frames after the reaction has occurred, one can start from the principle of conservation of energy. This is given by

$$\frac{M \mathbf{v}_{cm}^{M^2}}{2} + \frac{m \mathbf{v}_{cm}^{m^2}}{2} = Q + \frac{M \mathbf{V}_{cm}^{M^2}}{2} + \frac{m \mathbf{V}_{cm}^{m^2}}{2}, \quad (3.56)$$

, where Q is the excitation energy of one of the scattered particles. When elastic collision occurs, $Q = 0$. Starting from the previous equation and using Equation (3.47) one can find after a lengthy calculation that

$$V_{cm}^M = \left(\mathbf{v}_{cm}^{M^2} - \left(M + \frac{M^2}{m} \right)^{-1} Q \right)^{\frac{1}{2}}, \quad (3.57)$$

$$V_{cm}^m = \left(\mathbf{v}_{cm}^{m^2} - \left(m + \frac{m^2}{M} \right)^{-1} Q \right)^{\frac{1}{2}}. \quad (3.58)$$

Using once more Equations (3.54a) and (3.54b), the speed of the particles in the lab frame after collision can be found:

$$V_{lab}^M = \sqrt{\mathbf{V}_{cm}^{M^2} + \frac{M^2}{m^2} \mathbf{v}_{cm}^{M^2} + 2v_{cm}^M V_{cm}^M \cos \theta_{cm}} \quad (3.59a)$$

$$V_{lab}^m = \sqrt{\mathbf{V}_{cm}^{m^2} + \frac{M^2}{m^2} \mathbf{v}_{cm}^{m^2} - 2v_{cm}^m V_{cm}^m \cos \theta_{cm}}. \quad (3.59b)$$

Note that these equations do not explicitly depend on the lab angles ϕ and ξ but rather on θ_{cm} . The equation can however be related to their respective lab angles through Equations (3.55a) and (3.55b).

3.3.2 The Kinematics of the ${}^6\text{Li} + \alpha$ reaction

During the experiment, different beam energies were used. Furthermore, the energy of the ${}^6\text{Li}$ beam degraded when it traveled through the gas medium. Because of this, a very broad spectrum of incident energies should be considered when looking at the kinematics. This makes identification of the particles through the kinematics of the problem somewhat harder. Nevertheless, it is useful to consider one beam energy and discuss the kinematics of the ${}^6\text{Li}(\alpha, \alpha'){}^6\text{Li}$ reaction in inverse kinematics since the general features stay the same.

In this section the kinematic plots of the ${}^6\text{Li}(\alpha, \alpha'){}^6\text{Li}$ reaction will be discussed. Two cases will be considered, elastic and inelastic scattering. In the case of elastic scattering, the Q -value of the reaction is 0. In the case of inelastic scattering, only excitations of ${}^6\text{Li}$ will be considered. As mentioned earlier, the first excited state of ${}^4\text{He}$ is found at an energy of 20.21 MeV [18]. This is a very high energy, hence it is highly improbable for the highest beam energies and even impossible for the lower beam energies that this state becomes significantly populated. The first excited state of ${}^6\text{Li}$ is found at 2.186 MeV [21] and can significantly be populated. The calculations of the inelastic scattering case have been performed with respect to this excited state. The Q -value of this reaction is then also equal to 2.186 MeV.

Figures 3.4(a) and 3.4(b) show the lab angles of ${}^6\text{Li}$ and ${}^4\text{He}$ versus their respective center of mass angles. It can be seen that both particles cover center of mass angles from 0° to 180° . For the ${}^4\text{He}$ particle there exists a simple linear relation between the angles in the two frames. In the case of ${}^6\text{Li}$ there is a maximal lab angle at approximately 42° . Two separate center of mass angles correspond to a single lab angle. In the case of inelastic scattering, more or less the same behavior is seen in the case of ${}^6\text{Li}$. The maximum lab angle is smaller, about 32° . There is no longer a linear relationship in the case of ${}^4\text{He}$. The behavior is qualitatively similar to that of ${}^6\text{Li}$. The maximum angle is about 55° .

Figures 3.5(a) and 3.5(b) show the lab energies of ${}^6\text{Li}$ and ${}^4\text{He}$ versus their respective center of mass angles. For both elastic and inelastic scattering it can be seen that the energy changes significantly with center of mass angle. The energy of the ${}^6\text{Li}$ particle is never zero however. From this it is also clear that the two different center of mass angles which had one common lab angle (see Figures 3.4(a) and 3.4(b)) correspond to two very different regimes. One center of mass angles corresponds to a low kinetic energy, the other to a high kinetic energy. The information of the previous two sets of figures can be combined to find the lab energies of the particles as a function of the lab angles. This is shown in Figures 3.6(a) and 3.6(b). These kind of plots are also called *plectrum* plots. The same typical features from before can be seen. Interesting to note is that in the inelastic case, the plectrum-like shapes tend to become smaller with increasing excitation energy.

An especially useful kinematic plot is that of the angular correlations between the two particles. This can be seen in Figure 3.7. From the equations given in Section 3.3.1, it can be shown that when elastic scattering occurs, the angular correlation between the ${}^6\text{Li}$ and ${}^4\text{He}$ particles is independent of the energy of the incident particle. Hence, the angular correlation provides a good means to check the consistency of the measured angles.

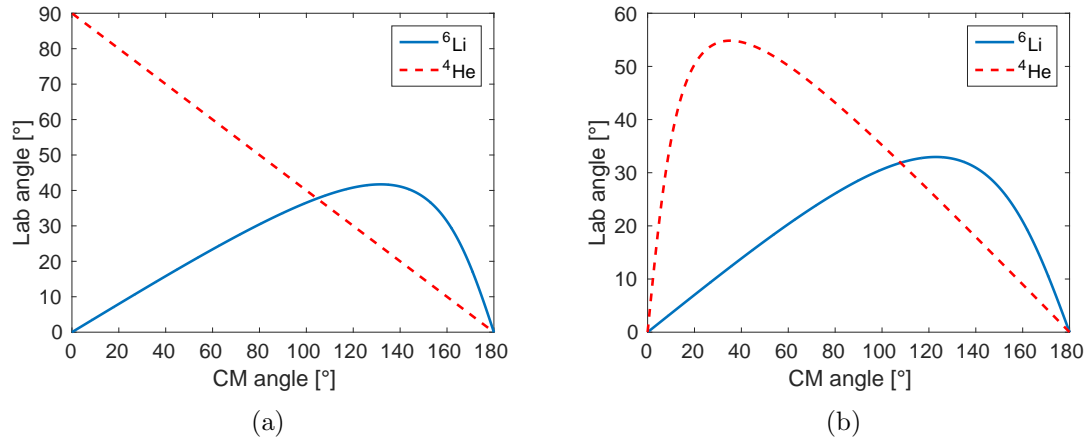


Figure 3.4: Expected relation between the lab angles and center of mass angles of ${}^6\text{Li}$ and ${}^4\text{He}$. The calculations have been performed with an initial kinetic energy of 16.5 MeV. The Figure (a) shows relation in the case of elastic scattering. Figure (b) for inelastic scattering.

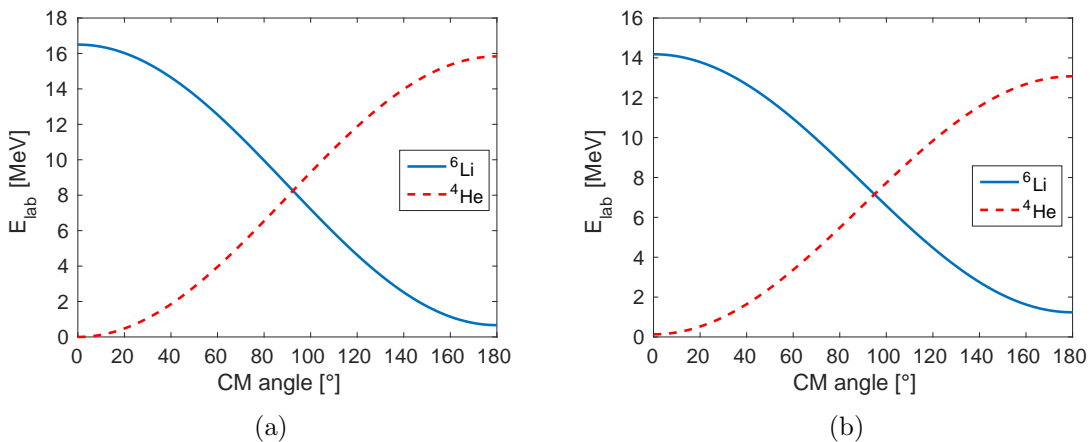


Figure 3.5: Expected relation between the lab energies and center of mass angles of ${}^6\text{Li}$ and ${}^4\text{He}$. The calculations have been performed with an initial kinetic energy of 16.5 MeV. The Figure (a) shows relation in the case of elastic scattering. Figure (b) for inelastic scattering.

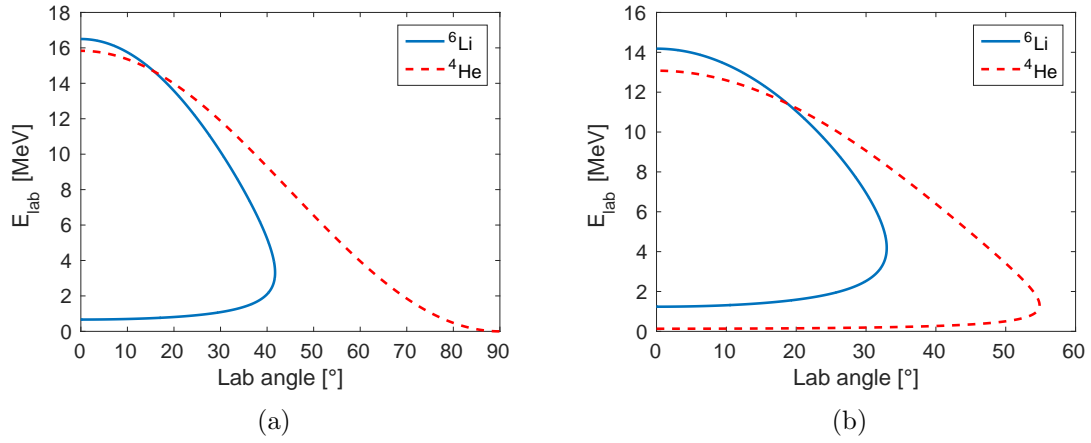


Figure 3.6: Expected relation between the lab energies and lab angles of ^6Li and ^4He . The calculations have been performed with an initial kinetic energy of 16.5 MeV. The Figure (a) shows relation in the case of elastic scattering. Figure (b) for inelastic scattering.

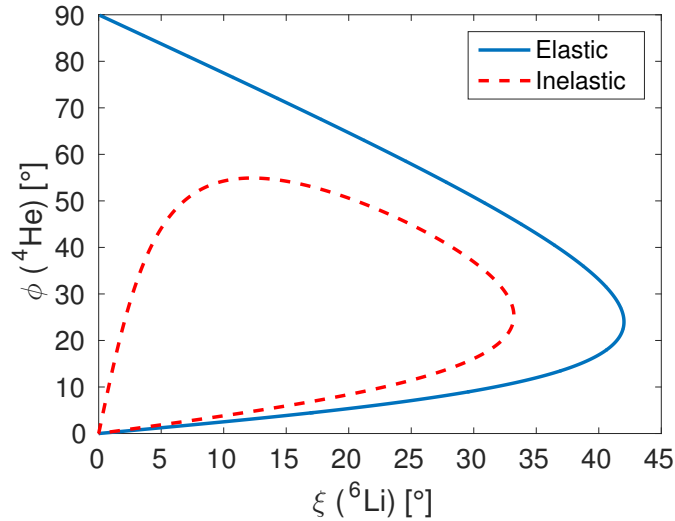


Figure 3.7: Expected relation between the lab angles of ^6Li and ^4He . The calculations have been performed with an initial kinetic energy of 16.5 MeV. The angles correspond to those indicated on Figure 3.3(a).

This is however, no longer true when inelastic scattering occurs. It is expected that for increasing excitation energy, the particles are increasingly more found at forward angles. The scattering angles also tend to become smaller as the energy of the incident particle decreases.

Chapter 4

Data analysis

To make any kind of claim on the properties of ^{10}B a thorough analysis of the experimental data has to be done. In this chapter the several steps in this process are explained and the results discussed.

4.1 Calibration of the detector components

4.1.1 The DSSDs

Right before and after the experiment, additional measurements have been done for calibration purposes. The used source was presented in Section 2.3.5, more specifically in Table 2.2. For a detector of ideal resolution, seven peaks are expected. In the present case only three peaks could be resolved. Each of the 256 electronic channels (4×64) had to be calibrated separately. For this reason a code was written to automate the calibration process. In this procedure, first the number of distinct peaks was counted. The centroids of those peaks are found through a fitting procedure. Those centroids, which are still denoted in channel numbers, are then plotted against the known decay energies (Table 2.2). Ideally the centroids lie on a straight line such that a linear fit through the three points then results in useful calibration parameters. Using these parameters any arbitrary channel number can be converted into an energy value.

When the peaks are nicely symmetric, Gaussian functions should be sufficient to fit the peaks. However, in the present case a tail at the low energy side of the peaks is present. This tail is due to energy losses in the dead layer of the detector and incomplete charge collection [71]. Because of this, the use of Gaussian functions results in estimations of the centroids which do not lie on a straight line. An example of this can be seen in Figure 4.1(a). Bortels *et al.* [87] has suggested an analytical function to fit α decay spectra for which the peaks exhibit tails. The suggested function is the result of a convolution of a Gaussian function and a left-handed exponential. It is given by

$$f(x; A, \mu, \sigma, \tau) = \frac{A}{2\tau} \left(\frac{x - \mu}{\tau} + \frac{\sigma^2}{2\tau^2} \right) \operatorname{erfc} \left[\frac{1}{\sqrt{2}} \left(\frac{x - \mu}{\sigma} + \frac{\sigma}{\tau} \right) \right], \quad (4.1)$$

where A is the area under the peak, τ a parameter defining the exponential function, μ the centroid of the peak, σ the standard deviation and $\operatorname{erfc}()$ the complementary error function. Note that μ and σ are defined through the Gaussian function. Hence they have the same useful interpretation. In general, one can use multiple exponential functions

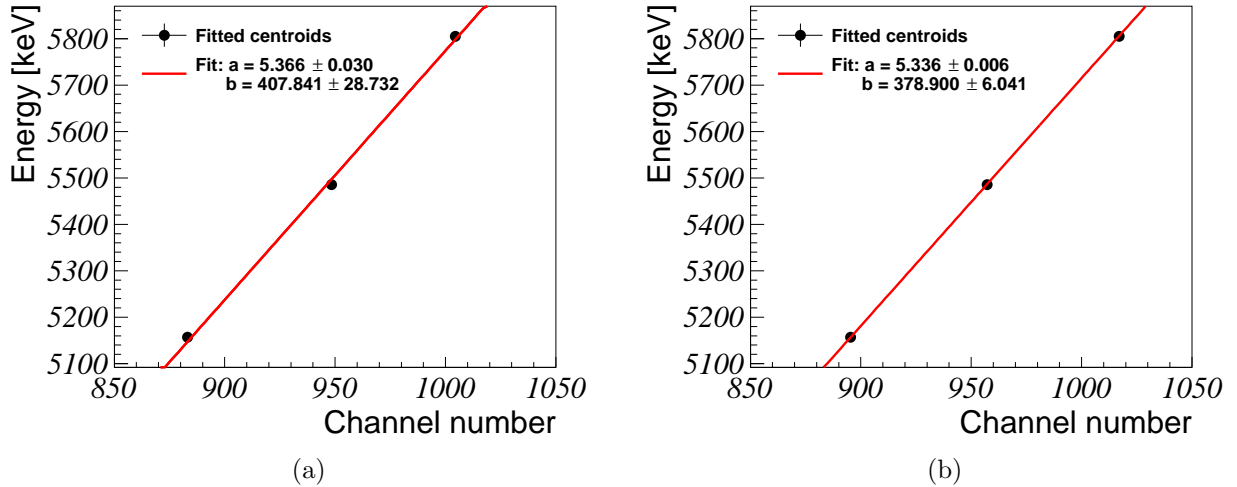


Figure 4.1: Plots showing the difference in quality for the two different fitting functions used to fit the triple α spectrum. (a) shows the result of the procedure with three Gaussian functions. (b) shows the result when the fitting function of Equation (4.2) is used. Strip 28 of DSSD 0 (right top corner following the direction of the beam) was used in this example. In both cases the error on the centroid is smaller than the size of the used marking.

with different τ parameters to improve the fit. The following fitting function was used in the present case (for three peaks) [88]

$$F(x) = \sum_{j=1}^3 \sum_{i=1}^2 \eta_{ji} f(x; A_j, \mu_j, \sigma_j, \tau_i), \quad (4.2)$$

where the factors η_i are scaling factors defining the weight of the exponential functions. Figure 4.1(b) shows the linear fit through the centroids when they are estimated by using the fitting function of Equation (4.2). It can be seen that the collinearity of the three is stronger. Moreover, all the points are shifted towards higher channel numbers, indicating that the fit is less influenced by the tail.

During the calibration it became apparent that the resolution of the several detectors is not the same. For all four DSSDs, the strips on the front have a better resolution. This is illustrated in Figures 4.2(a) and 4.2(b). It is clear that the strip on the front side has better resolved peaks and that the tail on the low energy side is less heavy. The degradation of the resolution of the backside strips is most likely due to incomplete charge collection as it was observed that in some cases multiple neighboring strips were hit on the back side whereas only a single strip was hit on the front side. Nevertheless, the use of the fitting function presented in Equation (4.2) still resulted in reasonably good estimates of the centroids for most strips.

Figure 4.3 shows the resolution for each separate strip. It can be seen that the four DSSDs perform roughly the same. The resolution seems to be more stable for DSSDs 1 and 3. These detectors are located in the bottom half of the chamber. Once more it is clear that the resolution of the strips on the back side of the detector is worse compared to the front side. For this reason, all the following analysis steps have been performed

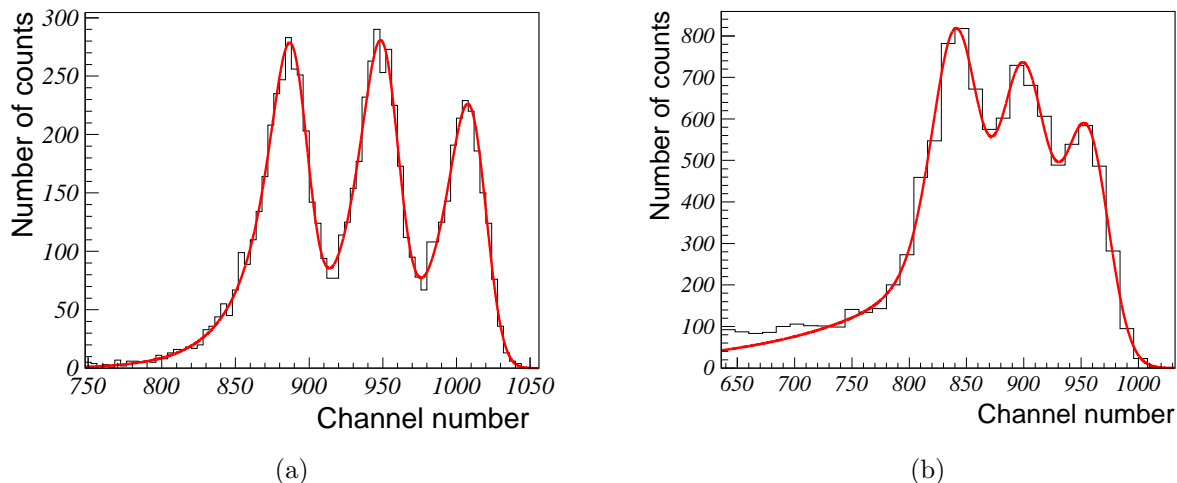


Figure 4.2: Plots showing the measured triple α spectra for two strips of DSSD 0. Figure (a) corresponds to a strip on the front side (strip 28) and figure (b) to a strip on the back side (strip 60). The red line shows a fit to the histogram of the form presented in Equation (4.2).

only using energy information from the front side. The information from the back side has solely been used to identify which pixel of the DSSD has been hit during an event. Lastly, it seems like the resolution somewhat improves for strips closer to the center of the chamber¹. This effect is most pronounced in case of the front sides. Particles hitting strips further away from the center have to travel through a larger effective dead layer. This degrades the resolution in those cases and explains the trend [71].

4.1.2 The Maya detectors

The overall procedure to calibrate the Maya detectors was the same as explained in Section 4.1.1. To fit the three peaks, the same fitting function as before (Equation (4.2)) has been used. The resolution of these detectors can be seen in Figure 4.4. The resolution is comparable to the resolution of the DSSDs (see Figure 4.3). It is clear however that for the detectors on the left side, the resolution is consistently worse compared to the detectors on the right side of the detection chamber. The resolution is especially worse for detectors 2, 3 and 4 on the left side. These are located towards the end of the chamber following the direction of the beam (see also Figure 2.4). This is somewhat unfortunate because from the kinematics of the considered reaction (see Section 4.4) and the geometry of the detector, it is expected that these detectors can detect more useful events.

4.1.3 Alignment of the padplane

The various pads of the MICROMEGAS do not have exactly the same charge multiplication capabilities. Corrections are needed for this such that a specific amount of deposited

¹In the case of the front side, strips close to the center are found at high strip numbers. For the back side, strips close to the center are found at high strip numbers for DSSD 0 and 2 and at low strip numbers for DSSD 1 and 3.

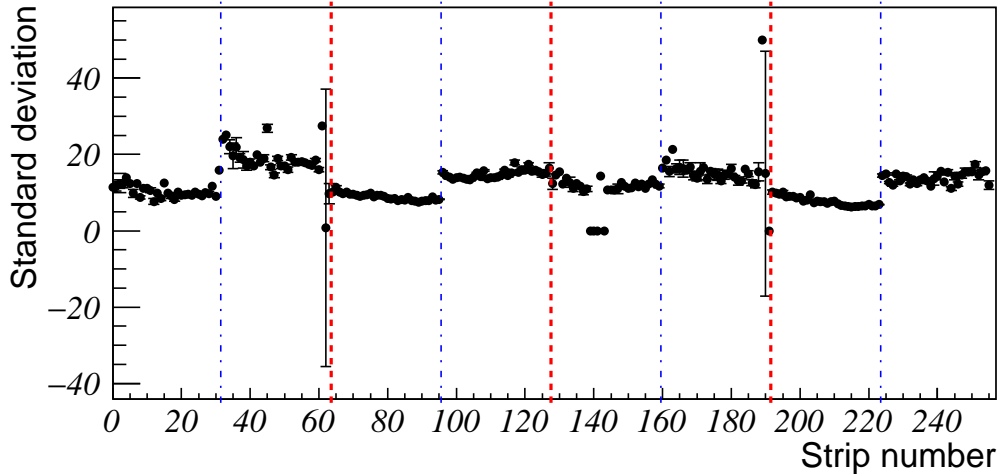


Figure 4.3: Plot of the mean resolution (average of the three peaks) for each separate strip. The resolution is denoted in channel number. The first 64 strip numbers correspond to DSSD 0, the second set of 64 strip numbers to DSSD 1, etc. For clarity, the red dashed lines separate the four DSSDs. The blue dash-dotted lines separate the strips related to the front and back side of the detector. In some cases the error is masked by the size of the marking. A standard deviation of 0 means that the strip was not operational.

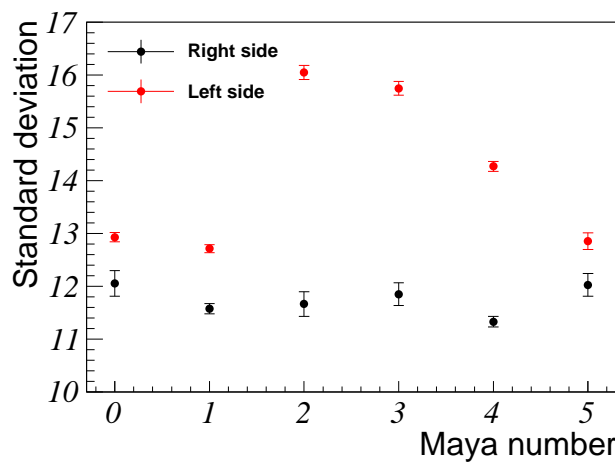


Figure 4.4: Mean resolutions for the twelve maya detectors. Values indicated by the red markers correspond to the silicon detectors located at the left side following the direction of the beam. The values indicated by the black markers corresponds to the detectors on the right side of the detection chamber. The resolution is denoted in channel number

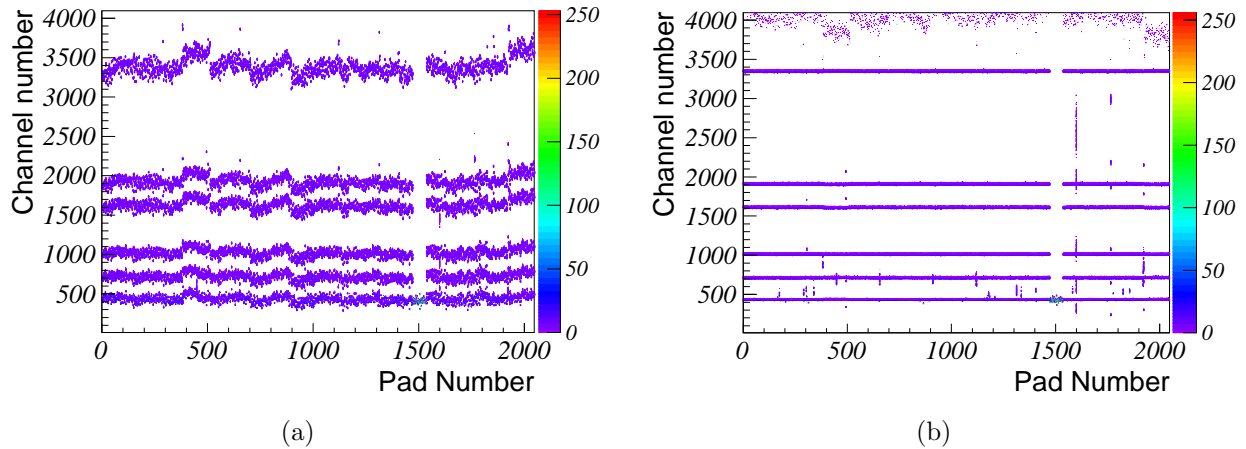


Figure 4.5: Plots showing the results of the pulser measurement for all 2048 separate pads. Figure (a) shows the result before alignment of the pads, figure (b) after the alignment of the pads. The noisy signal at high channel numbers in (b) are due to a 7th signal which was saturated and thus not properly measured.

energy can be related to a specific amount of collected charge. The pulser capabilities of the electronics have been used to perform measurements for each of the pads separately. All observed peaks were nicely symmetric and could be fitted with Gaussian functions. Taking a single pad as the reference, conversion parameters for each of the pads were calculated such that in a sense, the pads have been calibrated. A real calibration by using the triple α source and performing calibration measurements in a gas was not strictly needed since in the analysis presented below, no energy information has to be extracted directly from the collected charge.

Figure 4.5(a) shows the result of the pulser measurement for each separate pad before any alignment has been done. It is clear that the results can vary a lot for the separate pads. Around pad number 1500, there is a discontinuity in the lines. The pads did not function properly during the measurement and will not be treated in the subsequent analysis steps. Figure 4.5(b) shows the same result, but after the pads have been aligned. Six more or less straight lines can be seen, showing that the procedure works as intended. In the subsequent analysis steps, the same conversion parameters have been used to treat the particles signals recorded by the MICROMEGAS. While it can not easily be seen on Figure 4.5(b), there are slight shifts in the channel number for two sets of pad numbers (two times two separate AGET chips) around pad number 450 and 2100. This is due to nonlinear behavior in the electronics. However, the effect is small and did not generate problems in the subsequent analysis steps.

4.2 Treatment of the particle tracks

4.2.1 Fitting of the tracks

An important step in the analysis procedure is the fitting of the tracks created by the particles. For each triggered pad, the collected charge and drift time was recorded. Con-

sidering the triggered pads, a track could be fitted where the collected charge served as a weighting factor for each pad. Via the drift velocity, the drift time was converted into a distance with respect to the padplane. Hence it wa possible to determine the z -component of track.

The first step in the algorithm consists of finding the starting point of the track by iterating over the pad positions. To simplify the iteration procedure, it was chosen to divide the padplane into two halves, more precisely a left halve and a right halve. Once a starting point is found, the iteration proceeds, considering only the triggered pads which are in the neighborhood of the last treated pad. The information found in these pads is then used in a three-dimensional fitting algorithm as suggested by Reference [89]. When holes in the track are encountered, they are skipped. Once the track has been fitted, it is easy to estimate the scattering angle in the xy -plane θ , the scattering azimuthal angle ϕ and the three dimensional scattering angle θ_{3D} via trigonometric formulas. When a second track is found in the same halve, the algorithm is simply restarted. To make sure that the same pad is not used a second time, it receives a flag the moment it is used in the fitting procedure for the first time.

This straightforward procedure fails in some specific situations and some adaptations had to be made. A first problem occurs when the track is scattered at a small angle θ . The result is that the track is influenced by charges created in the masked beam area, but have drifted outside this area. Additionally, part of the track created after the scattering event is masked. This results in a underestimation of the scattering angle. The procedure to resolve this problem is essentially the same as the one suggested in Reference [90] and is illustrated in Figure 4.6(a). The basic idea is to apply an artificial cut on the side of the track opposite to the border of the masked area. This cut and the border of the masked area define an area of relevant pads on which the fitting procedure is redone. The additional cut balances the effect the border has on the result. This procedure is repeated multiple times until the fitted angle converges.

A second problem arises when multiple tracks are present on one halve of the padplane and their vertex positions are very close to one another². This problem is treated in two ways. When the two tracks arise from two distinct scattering events and the second event happens considerably later than the first event, the two tracks can easily be disentangled by looking at their timing characteristics. While iterating over the pads of the first track, an additional check is performed in which the timing between the present and previously treated pad is compared. When the difference between the two timings is large, the present pad is related to the second track and is skipped. This is seen in Figure 4.6(b) where the line separates the two tracks on the basis of their timing characteristics. The skipped pads can then be considered in the fitting of the second track. A more difficult situation arises when the two tracks also have more or less the same timing characteristics. Then the charge pattern of the tracks must be considered. In principle, the charge density is expected to be the highest in the center of the track. Charges at the edges of the track have drifted away from the center. Hence, if one considers a single line of pads perpendicular to the y -direction, it is expected that the collected charge rises, reaches a maximum and then goes back to zero. If now two track lie next to each other, one can expect the charge pattern to rise, reach a maximum, decrease and eventually rise again due to the presence of the second track. It is then possible to separate the first track

²They can for example be close when two distinct scattering events happen close to each other. The vertex position is even the same if the two track arise from the breakup of ${}^6\text{Li}$ into $\alpha + d$.

from the second by stopping the iteration over the pads (in a single line) when the charge pattern starts to rise again after its decline. This procedure is shown in Figure 4.6(c). In the figure a line separates the two tracks on basis of the charge.

A last problem occurs for tracks which consist of pads close to the corners of the field cage. In these case the track starts to deviate from a straight line and bends over towards the left or right side (depending which halve is considered) of the field cage. This is due to stray fields from the DSSDs and Maya detectors. These field cause deformations of the drift field. Because of the deformations, the electrons no longer follow a path straight to the padplane, but more in the xy -plane. This way, the charge is collected on the wrong pads. An example of this effect can be seen in Figure 4.6(d). The bending of the tracks obviously distorts the fit such that the scattering angle is incorrectly estimated. To resolve this problem, areas where the deformation becomes important have been defined. The fitting of the track proceeds as usual until pads are reached which lie in these predefined areas. These pads are then simply not considered in the fit, such that only pads forming a straight track line are used. This way a correct estimation of the scattering angle is regained. The grey zones in Figure 4.6(d) indicate the areas not considered in the fitting procedure.

4.2.2 Determination of the vertex position

Due to the masked area, the actual vertex position of the reaction could not be observed. However, when all tracks are fitted exactly, the vertex is found at the position where the fits of the tracks coincide. In practice, this is never the case due to uncertainties on the fitted angle. It was therefore chosen to find the vertex position through a least-square minimization procedure. Essentially this reduced the problem to solving a set of linear equations³. Two cases had to be considered where either two or three tracks coincide. These cases are physically related to the elastic scattering of ${}^6\text{Li}$ on α and inelastic scattering of ${}^6\text{Li}$ on α where ${}^6\text{Li}$ experiences a breakup into $\alpha + d$ (also see Section 4.3). It should be mentioned that in the latter process, the tracks of the d were sometimes either absent or only measured partially. This is because the gain of the MICROMEGAS was not high enough to accommodate the lower charge deposition by the d .

Obviously there is a margin of error on the vertex determination. This is partially due to the least-square procedure to find the vertex. However, since the calculated vertex position depends on the fitted angles, the error on these angles also directly contribute to the error on the vertex position. Unfortunately, the error on the fitted angles could not be determined because there is no knowledge on what the real scattering angle is. To get estimates of the error, the scattering events will have to be simulated. This is out of the scope of this thesis.

Only events for which the calculation of the vertex position yields physically possible results are usable in the subsequent analysis steps. The vertex is only deemed physically reasonable when its calculated value lies close to the path of the beam and when it is found within the borders of the gas chamber. Revisiting Figure 2.4 on page 37 shows that

³A line in three dimensions can easily be written as

$$\mathbf{r}_{0,i} + s_i (\mathbf{r}_{1,i} - \mathbf{r}_{0,i}), \quad (4.3)$$

where $\mathbf{r}_{0,i}$ and $\mathbf{r}_{1,i}$ are two coordinates defining the i th line and s_i its slope. One simply has to find the parameters s_i such that the lines intersect.

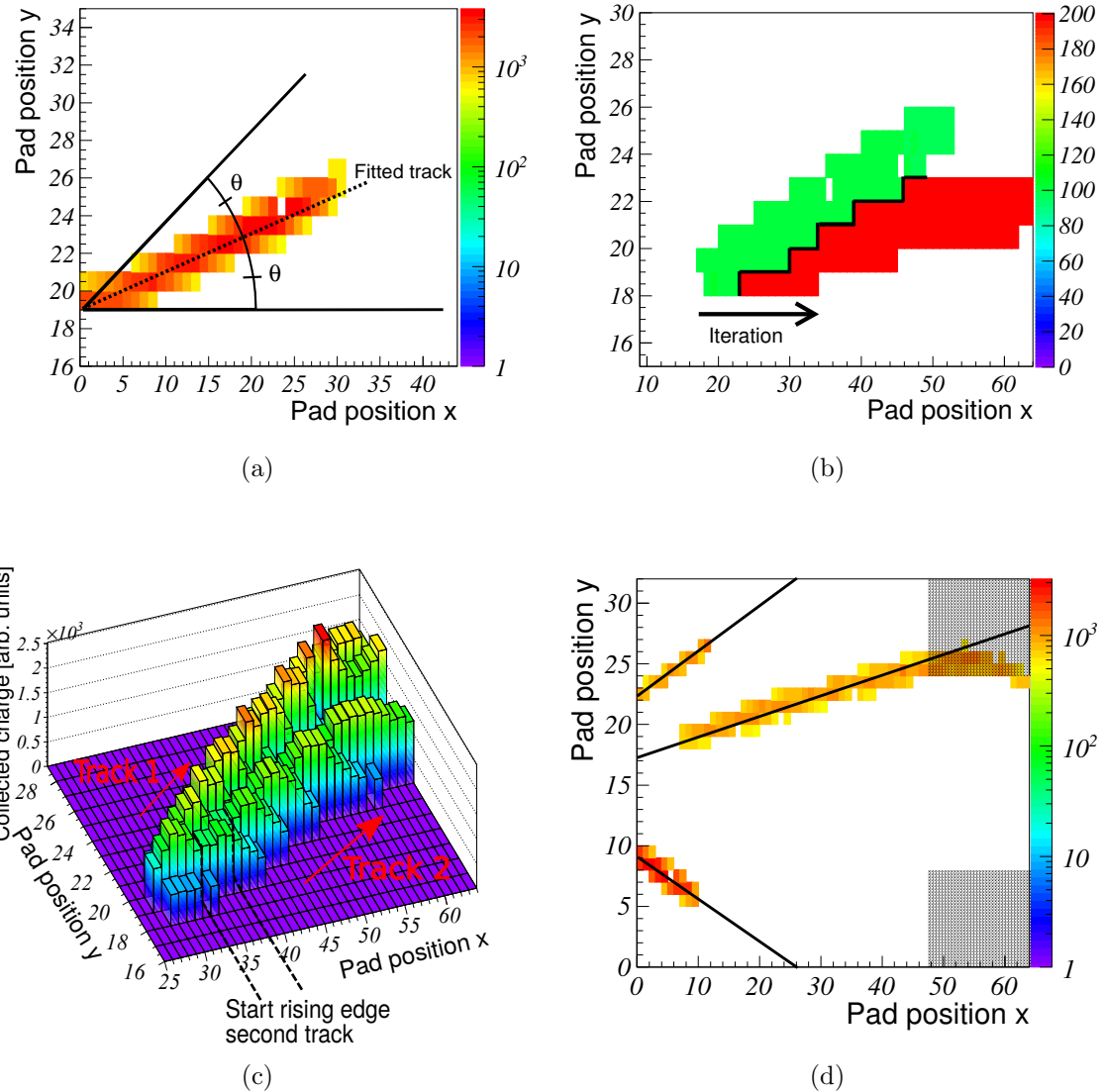


Figure 4.6: Set of figures indicating the several types of problems which can occur and how they can be solved. For more information on the procedures, see text. Figure (a) shows that an underestimation of the scattering angle θ can be solved by using an artificial cut at an angle of 2θ . Figure (b) shows that two tracks can be untangled on the basis of their timing characteristics. Figure (c) shows the charge profiles of two tracks. The tracks can be untangled on the basis of their charge characteristics. Figure (d) shows the problem of the bending of the tracks. The lines show the fits of the tracks when the charge in the gray zones is discarded. The color coding of (a), (c) and (d) is related to the collected charge. In (b) it is related to the measured drift time. Only (d) shows the complete padplane. Note that multiplying the value of the pad positions by 2 results in the actual geometrical dimensions in mm.

the distance between the entrance window and the MICROMEGAS is about 55 mm. All vertices found in this region must thus also be considered.

4.3 Particle identification

A common way to identify particles is by looking at their energy loss while they travel through a certain type of material with a fixed thickness. In the present case, the material is a gas. As discussed in Section 2.3.1 on page 34, the stopping power S is characteristic for each particle-gas combination but also depends on the speed of the particle. In a non-relativistic approximation S is given by [71]

$$S = -\frac{dE}{dx} = \frac{4\pi e^4 z^2 Z N}{m_e v^2} \ln \left(\frac{2m_e v^2}{I} \right), \quad (4.4)$$

where e is the charge of the electron, z and Z are the charge states of the incident ion and absorber atoms respectively, m_e is the electron rest mass, v is the speed of the incident ion, N is the electron number density and I is the average excitation and ionization potential of the absorber gas. This equation is also called the Bethe-Bloch formula. After integration of Equation (4.4) with respect to the path covered by the ion in a specific region of the gas chamber, the total energy lost while traversing this region can be calculated. The amount of energy lost in this region can then be plotted versus the energy measured in one of the silicon detectors. Such a plot is called a ΔE - E plot. One expects to see distinct lines for different particles because the energy loss is dependent on the charge state and mass of the ion⁴. Furthermore, the energy in the silicon detector is implicitly related to the speed of the ions⁵. If one gates on the lines present in the ΔE - E plot, an identification of the particles is effectively done. In the present case, no energy calibration of the padplane was performed. Still, the amount of created charges in the gas should be proportional to the energy deposited in the gas. It is thus sufficient to create ΔE - E plots in which the ΔE is still represented in channel numbers. The downside to this procedure is that no quantitative comparisons can be made with calculations done via SRIM⁶.

To create the ΔE - E plots, the regions over which the charge related to the ΔE is collected, must be strictly defined. The definition of the regions can be seen in Figure 4.7. However, because the particles scatter at different angles θ_{3D} , they also have different traveling distances in this region. More specifically, larger scattering angles result in larger effective thicknesses the particle has to traverse. In order to make reasonable comparisons between the particles a correction factors must be applied to the measured charge. From the geometry of the scattering problem it is easily seen that this correction factor is $\cos \theta_{3D}$ for particles detected in one of the DSSDs. A factor $\cos \phi \sin \theta$ has to be considered when particles are detected in one of the Maya detectors.

⁴The energy loss is not explicitly dependent on the mass (see Equation (4.4)). However, it is dependent on the speed. For a fixed energy, the speed of particles with a higher mass, will be lower.

⁵This requires to calculate the distance between a specific position in the gas chamber and the silicon hit position. Via SRIM the energy lost over this distance can be found. Adding this value to the energy measured in the silicon detector, results in the energy at the considered position and hence, its speed the speed of the particle at this position.

⁶It would in principle still be possible to do qualitative comparisons by looking at the relative differences between the lines.

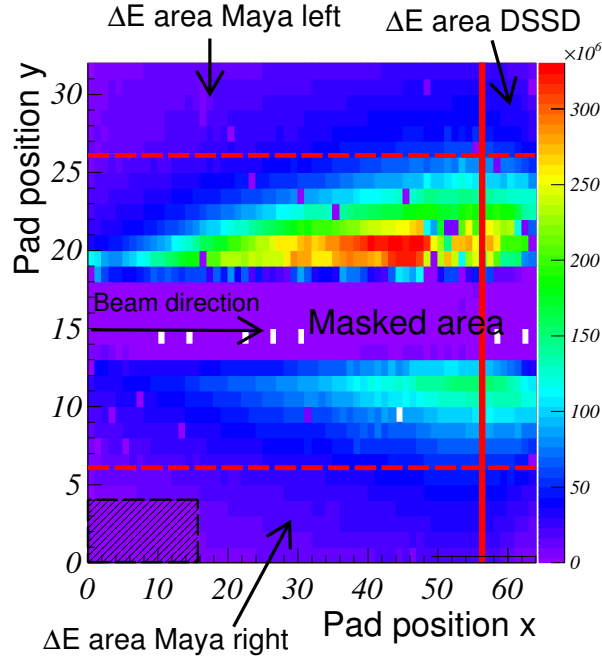


Figure 4.7: Plot with the total charge collected (in channel numbers) on the padplane. The plot was created from runs 281 and 282 for which a beam energy of 21 MeV was used. The red solid line indicates the start of the area which is considered to create the ΔE - E plot for particles detected in one of the DSSDs. The red dashed lines delimit the areas considered for the ΔE - E plot for particles identified in one of the Maya detectors. The black dashed line shows the area where a card of the electronics was present. Because of this, no proper measurements could be performed in this area.

In the present experiment, three particles can be expected to be found, ${}^6\text{Li}$ nuclei, α particles and deuterons. Sections 4.3.1 and 4.3.2 will discuss the ΔE - E plots for particles detected in the DSSDs and Maya detectors respectively. Each time the left and right side of the chamber will be discussed separately in order to point out some difference between the two sides.

4.3.1 The DSSDs

Figures 4.8(a) and 4.8(b) show the ΔE - E plots for particles detected in the DSSDs located in the left and right halves of the gas chamber respectively. The plots correspond to a beam energy of 21 MeV. For other beam energies similar results are obtained. It should be noted that in these plots only events are considered for which the fitted track is correlated to the correct pixel in the relevant DSSD. This constraint is applied by calculating the hit position on the DSSD from information of the fitted tracks. Tracks for which the hit position does not coincide with the triggered pixel, are discarded.

In both cases, two lines can be seen. The charge and mass dependence of Equation (4.4) shows that the upper line is related to the ${}^6\text{Li}$ particles⁷. At about 13.8 MeV a blob can be seen. These points correspond to beam particles which escaped the mask. This is

⁷It should be noted that for two beam energies, 11.5 and 14 MeV, the ${}^6\text{Li}$ was not observed. The energy loss was too high such that the beam particles never reached the silicon detectors.

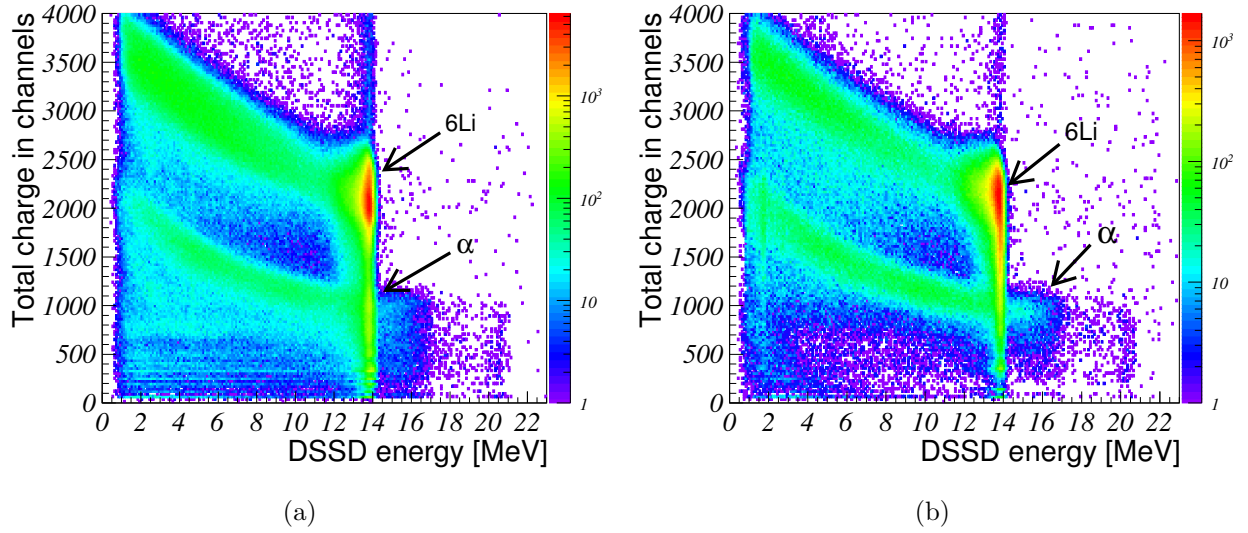


Figure 4.8: ΔE - E plots based on the DSSDs on (a) the left side of the gas chamber (DSSD 2/3) and (b) the right side of the gas chamber (DSSD 0/1). Notice the logarithmic color scale. The plots correspond to all measurement runs with a 21 MeV beam energy.

another point of evidence showing that this line should be the ${}^6\text{Li}$ line. The lower line corresponds to the scattered α particles. It can be seen that the maximally observed energy in the DSSDs is higher for these particles. This is possible when the α particles scatter at forward angles near the beginning of the chamber. (See also Figure 3.6(a) on page 60. Note however that a different energy for the ${}^6\text{Li}$ is considered.). Afterwards, the α particle loses less energy than the ${}^6\text{Li}$ particle.

It is clear that some tracks could not be properly identified. These are not necessarily the result of an improperly fitted track. Inspection of individual tracks shows that quite often one or more holes are present in the track. This lowers the collected charge such that points are found below the line they are actually part of. Another problem is that for some events the track only starts in the area considered for the ΔE - E plots. This limits the collected charge such that the points related to such events are also found lower than expected. The same problem is the source of the strong vertical line connected to the blob identified as beam particles. In this case the beam escapes the mask minimally, resulting in a low charge collection. It can be seen that overall, the quality of the plots is worse when the left half of the chamber is considered. Revisiting Figure 4.7, it can be seen that the charge pattern is less smooth for columns 46 up to 63 in the upper halve of the plot. This indicates that some pads were malfunctioning during the measurement, resulting in a lower charge collection. Note that the same problem was observed in nearly all experimental runs. A potential solution is to move the area for the charge collection further away from the end of the padplane, for example to columns 35 to 42. This would increase however the amount of events which can not be identified because more vertices would lie in the region used for the charge collection or behind this region.

Figure 4.8(b) shows an additional feature between 0.75 and 4 MeV and between a charge (in channels) of 0 and 1000. It is possible that this feature is due to deuterons. This feature does not clearly appear in Figure 4.8(a). It is probably obscured by the large

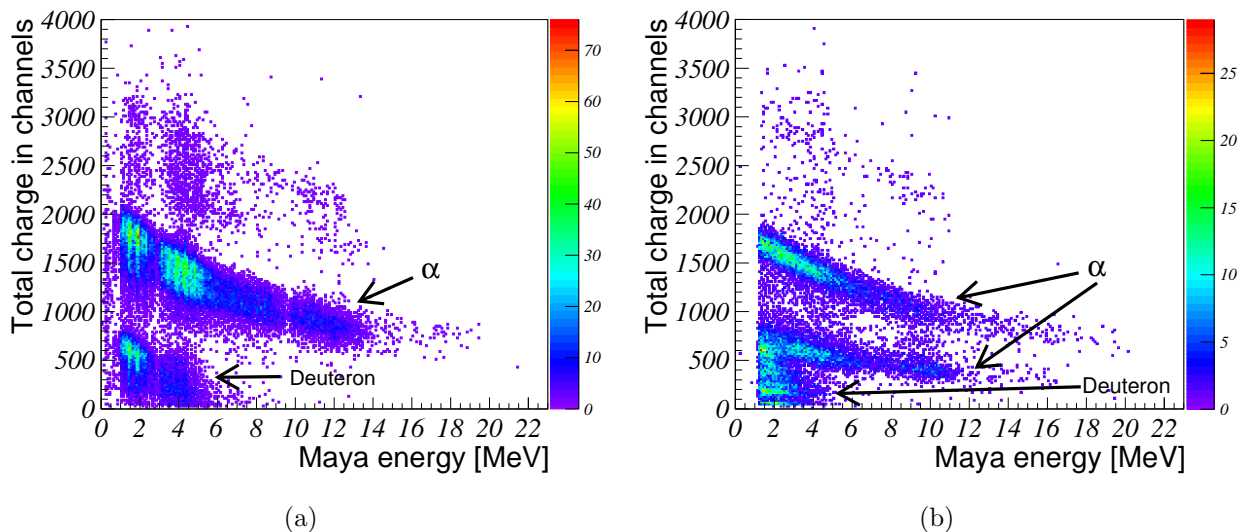


Figure 4.9: ΔE - E plots based on the Maya detectors on (a) the left side of the gas chamber and (b) the right side of the gas chamber. Notice the linear color scale. The plots correspond to all measurement runs with a 21 MeV beam energy.

number of particles which could not be identified.

4.3.2 The Maya detectors

Figures 4.9(a) and 4.9(b) show the ΔE - E plots for the Maya detectors located in the left and right halves of the gas chamber respectively. In Figure 4.9(a) two lines can be seen. The upper is this time related to the α particles. In order to reach the Maya detectors, the scattering angle is typically between 30° and 50° . Revisiting Figure 3.6(a) on Page 60 shows that the ${}^6\text{Li}$ particles loses a lot of energy in such a scattering event. Calculations with SRIM have shown the amount of energy left after the scattering is in most cases not sufficient to reach the detector. The few particles that do reach the detector create the few point above the α particle line. The lower line corresponds to detected deuterons. It can be seen that at around 2.75 and 9.75 MeV there is a decrease in counts. Furthermore, vertical lines seem to appear which distorts the nice banana-like shape of the α line. These features are due to a malfunctioning of the electronics during some events. Looking at the raw signal shapes, it becomes apparent that in some events, the correct values of certain time samples is elevated by a random number. The effect was most severe for time samples of which its signal value corresponds to energies around 2.75 and 9.75 MeV. The result is that the signal shape starts out correctly, but then suddenly attains a false maximum which is higher than the real maximum of the signal. For some events, when the elevated value is part of the rising or decreasing edge of the signal, the problem can be corrected. However, when the real maximum of the signal itself is elevated, a correction is no longer possible. This leads to the decrease of counts observed in the plot. Examples of a correctly and incorrectly measured signal can be seen in Figures 4.10(a) and 4.10(b) respectively. This problem occurred for all Maya detectors located on the left side of the gas chamber. The problem was present during the whole experiment. Only a few runs

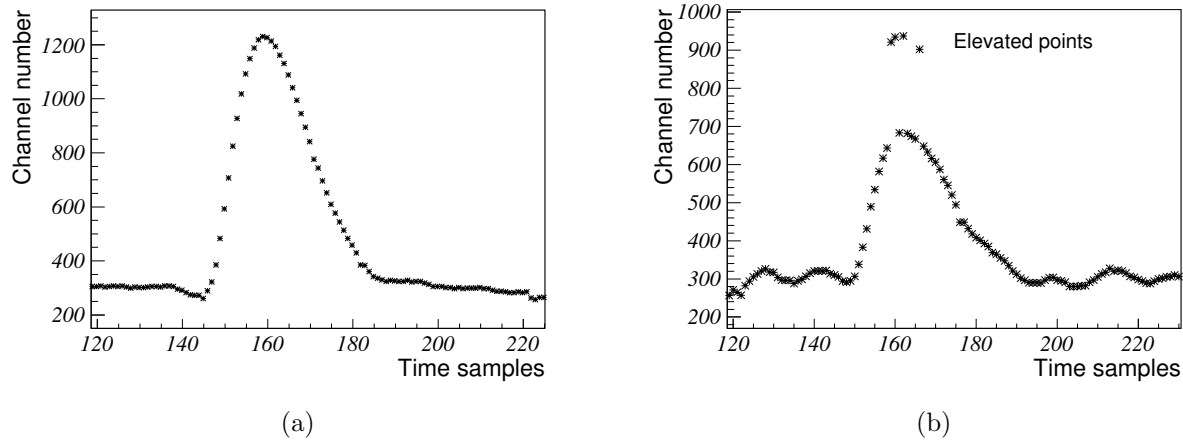


Figure 4.10: Examples of a good signal shape (a) and a bad signal shape (b). In case (b), the elevated points must be neglected in order to get the correct maximum.

did not exhibit the problem.

In contrast to Figure 4.9(a), three lines can be seen in Figure 4.9(b). Once more no clear line related to ${}^6\text{Li}$ can be distinguished. The top line corresponds to α particles. The middle lines covers more or less the same energy range in the Maya detectors which is an indication that this line also corresponds to α particles. Inspecting the tracks of these particles shows that they consistently cover pads in the left bottom corner as indicated on Figure 4.7 by the black dashed line. During the experiment, one of the electronic cards covered this area such that no charge could be collected. Because of this, the charge collection for particles traversing this area is lowered. Because this is a systematic effect, these particles can still be properly identified. Note however that the quality of the fits of these tracks might be lower because the amount of triggered pads which can be included in the fit is less. The lower line once more corresponds to the deuteron particles. It can be seen that this line is broader compared to the lowest lying line in Figure 4.9(b). This can also be attributed to tracks passing through the area masked by the electronics card. It is clear that the discontinuities observed in Figure 4.9(a) are not present in Figure 4.9(b). The problem with the signal shapes did not occur for the Maya detector located on the right side of the gas chamber.

4.4 Reconstruction of the kinematics

For each beam energy the kinematics of the scattering problem have been reconstructed. This is useful to compare with the results presented in Section 3.3.2. Especially the comparison of the angular correlation is useful as this is energy independent (for elastic scattering). It gives an idea how well the track fitting procedure reproduces the scattering angles. In this section only the plots for a beam energy of 16.5 MeV will be presented. For the other beam energies, similar results have been found. Note that throughout the experiment, alignment of the beam was not perfect. Based on the angle of detected beam particles, it was possible to deduce that the alignment was off by about 1.8° towards the left side of the chamber. This value varied slightly in time. This effect can also be observed

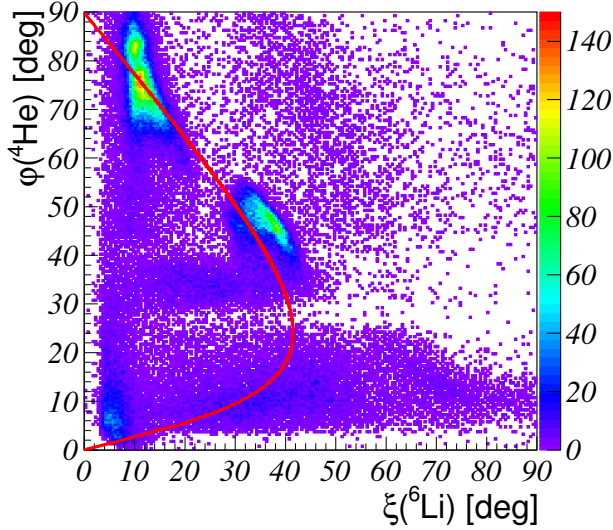


Figure 4.11: Plot showing the angular correlation between the scattering angles. The red solid line shows what is theoretically predicted in the case of elastic scattering (see also Figure 3.7). The figure contains all events for which at least one of the particles was properly identified, but only two clear tracks were observed.

in Figure 4.7 where clearly more charge is collected on the upper half of the padplane. In all the subsequent results, the fitted angles have been corrected for this offset in the alignment.

In Figure 4.11 the angular correlation for events in which two tracks were observed, is shown. Only events for which at least one of the particles could be identified, are included. When only two tracks are observed, it is assumed that these tracks correspond to a ${}^6\text{Li} + \alpha$ combination. If a track is identified as ${}^6\text{Li}$, it is assumed the other one is an α particle and vice versa. It can be seen that a strong feature appears between $\xi = 10^\circ$ and $\xi = 20^\circ$. These points agree with the theoretically predicted curve. A smaller feature appears between $\xi = \varphi = 0^\circ$ and $\xi = \varphi = 10^\circ$. These points lie agree less well with the predicted values. In these events the scattering angle of ${}^6\text{Li}$ is still consistently underestimated. The error is present because in this case the ${}^6\text{Li}$ particles have very little energy (see Figure 3.6(a)). Hence it is not possible to fit a proper track. There are also a lot of points present between $\xi = 20^\circ$ and $\xi = 45^\circ$ and $\varphi < 20^\circ$. Points which lie close to the red line can be identified as elastic events. Note that in the previous three features each time the identified particle was detected via the DSSDs. Overall, it seems like the scattering angles are properly found for particles identified by the DSSDs. A last clear feature appears between $\phi = 40^\circ$ and $\phi = 55^\circ$. These are events for which the α particle is identified by the Maya detectors. It can be seen that the feature appears at larger angles to the theoretically predicted values. Inspection of individual events do not show any systematic errors in the fitted angle. It is thus not clear why this feature is not exactly found at the theoretically predicted line. Unfortunately, the Maya detectors are not segmented such that the fitted angles cannot be compared with the hit position on the detector. A possibility to resolve this problem is make comparisons with simulations. These comparisons could indicate whether the problem is due to an error during the measurement or due to the fitting procedure. The problem seems to become less severe

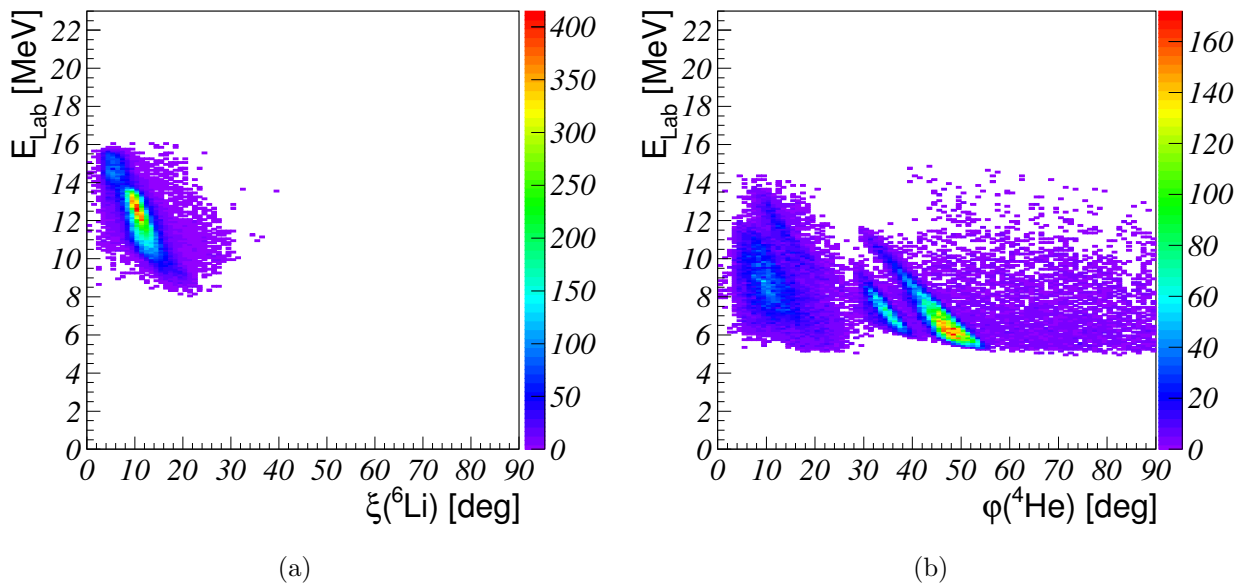


Figure 4.12: Plots related to the kinematics of the problem. Figures (a) and (b) show the lab energy versus the scattering angle for ${}^6\text{Li}$ and α particles respectively.

for higher energy runs. The exception is the 11.5 MeV run which is briefly discussed in Section 4.5.1.

All other points are either due to incorrectly fitted tracks or due to inelastic events. It is hard to make a clear distinction between the two because it is not easy to predict the angular correlation for the inelastic case. Moreover, ${}^6\text{Li}$ will experience a breakup and resulting particles are not emitted at fixed angles. They are however, confined in a *breakup cone* of several degrees. This cone becomes larger with decreasing energy.

To conclude this section the relation between the lab energies and the scattering angles will be discussed for both ${}^6\text{Li}$ and α particles. This can be seen in Figures 4.12(a) and 4.12(b) respectively. The first figure shows one distinct line. This is expected as the inelastic line of ${}^6\text{Li}$ should be absent since the nucleus experiences a breakup. This line does not nicely agree with the theoretically predicted result for a single initial energy. One can expect from the geometry of the setup that larger scattering angles can be measured when the scattering occurs deeper in the gas medium. However, the energy of the ${}^6\text{Li}$ beam particle decreases while traveling through the gas. There is thus in fact a whole range of theoretical lines corresponding to different initial energies which should be considered in order to reproduce the observed lined. In the second figure two sets of two lines can be seen. The first set is located at angles smaller than 25° and the second set at angles larger than 25° . The two sets correspond to particles detected in the DSSDs and Maya detectors respectively. Comparison with Figures 3.6(a) and 3.6(b) shows that each time the lines at larger angles should correspond to the case of elastic scattering. The other line then corresponds to inelastic scattering to the 3^+ state of ${}^6\text{Li}$. Once more a whole range of theoretical lines should be considered to reproduce the plot. The lines at larger scattering angles look sharper. This is because the various theoretical curves for different initial energies converge to one another as the scattering angle increases. The lines at smaller scattering angles are less pronounced due to a background of breakup α

particles. At forward angles it can be expected that when ${}^6\text{Li}$ breaks up in to $\alpha + d$, that the breakup α was identified instead of the scattered α . Between the two cases, no clear distinction can be made. This background will also influence the excitation spectrum of ${}^6\text{Li}$, discussed in Section 4.5.

4.5 Excitation spectrum of ${}^6\text{Li}$

In principle it should be possible to deduce the excitation spectrum of ${}^6\text{Li}$ from this experiment. If this spectrum can be recreated, it serves as an important proof that this kind of setup works. In the case of elastic and inelastic scattering, the energy of the ground state and excited states will be equal to the Q -value of the reaction. In the present case it can be calculated as [2]

$$Q = E_{obs} \left(1 + \frac{m_{obs}}{m_{stop}} \right) - E_i \left(1 - \frac{m_i}{m_{stop}} \right) - \frac{2}{m_{stop}} \sqrt{m_i m_{obs} E_i E_{obs}} \cos \theta_{obs}, \quad (4.5)$$

where E_{obs}, m_{obs} and θ_{obs} are the kinetic energy, mass and scattering angle of the identified particle, E_i and m_i are the energy and mass of the beam particle and m_{stop} is the mass of the other reaction product which is stopped in the gas. The identification of either reaction product thus determines which masses should be used in Equation (4.5). Note that a priori the mass of the excited ${}^6\text{Li}$ nucleus is not known. Using Equation (3.2) (page 44) and solving for Q together with Equation (4.5), gives a general result for any mass (and thus excitation state) of ${}^6\text{Li}$. The excited states of ${}^6\text{Li}$ can only be observed through the identification of the α particle because of the breakup of ${}^6\text{Li}$.

Knowing the masses of the ground states of ${}^6\text{Li}$ and the α particle, it is clear that three other quantities have to be known, namely the energy of the beam right before the reaction E_i , the scattering angle θ_{obs} and the energy right after the reaction E_{obs} . The first quantity is determined by the position of the vertex of the reaction. Through calculations with SRIM and knowing the beam energy at the entrance window, it is possible to calculate how much energy was lost while traveling to the vertex position. Subtracting this energy loss from the initial energy results in a value for E_i . The scattering angle is directly found from the fitting procedure. The energy E_{obs} is found by calculating the distance between the vertex position and the hit position (as calculated from the track properties) on the relevant silicon detector. Knowing the energy measured in the silicon detector and the traveled distance, calculations with SRIM can once more be used to determine the energy E_{obs} . Eventually Q can be calculated.

In the following two sections, the excitation spectra of ${}^6\text{Li}$ for two different beam energies, namely 11.5 and 16.5 MeV, will be presented. The excitation spectra related to the other beam energies will not be discussed in detail but can be found in Appendix A.1. Each time the spectra are presented twice, once for particles identified by the DSSDs and once for particles identified by the Maya detectors.

4.5.1 The 11.5 MeV beam energy

The calculated excitation spectra of ${}^6\text{Li}$ for a beam energy of 11.5 MeV can be seen in Figures 4.13(a) (the black histogram) and 4.13(b) for particle detected by the DSSDs and Maya detectors respectively. In both cases all counts are essentially due to detected α

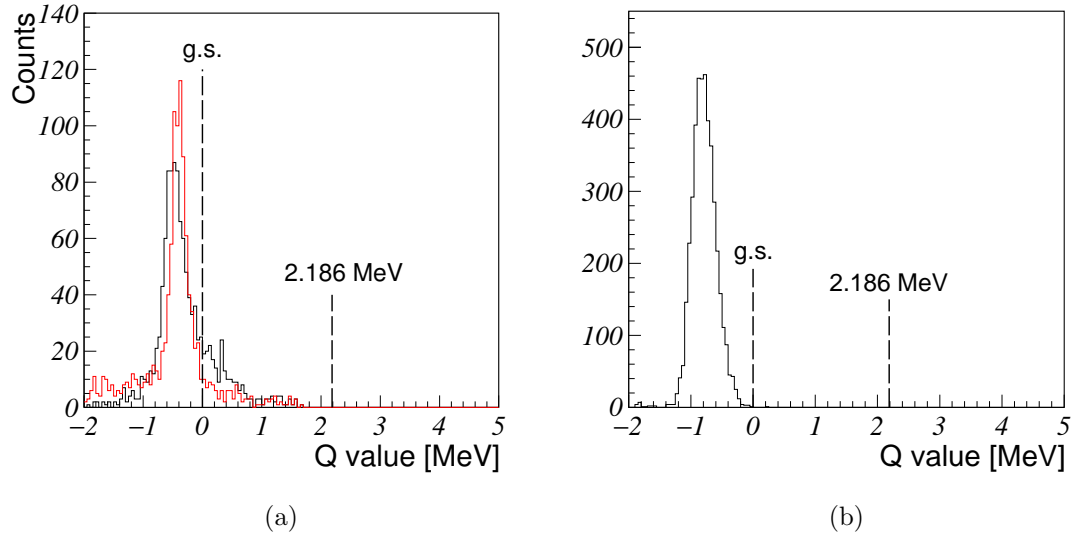


Figure 4.13: The ${}^6\text{Li}$ excitation spectra for (a) particles identified by the DSSDs and (b) particles identified by the Maya detectors. The black histogram in figure (a) shows the uncorrected spectrum. The red histogram shows the corrected spectrum. The dashed lines indicate the energies at which the ground state (0 MeV) and first excited state (2.186 MeV) are expected to be found [28].

particles. The ${}^6\text{Li}$ could not reach any of the silicon detectors. Only a single peak can be observed. The most likely option is that this peak is due to elastic scattering events. The inelastic peak can not be observed because no clear track for the scattered ${}^6\text{Li}$ particle can be measured. This can be explained via the kinematics of the problem and the geometry of the detector.

When elastic scattering occurs and the α particle scatters at forward angles (up to 20°), the scattering angles of the ${}^6\text{Li}$ particle can be as large as 40° (see Figure 3.7). In this case the energy of the scattered ${}^6\text{Li}$ will be low. As an example, it can be calculated that its energy ranges between 500 keV and 1 MeV when the energy before the reaction was about 8 MeV. These values will further decrease when the scattering occurs deeper in the chamber. Calculations from SRIM suggest that these energies are then quite sufficient to escape the masked beam area. The situation is similar when the α particle is detected by the Maya detectors. Then the ${}^6\text{Li}$ scattering angle will be similar as before, but the energy of the particle will be higher. Once more the particle can escape the masked area. On the other hand, when inelastic scattering occurs, if the α particle scatters at forward angles, the scattering angle of ${}^6\text{Li}$ is typically quite small (See Figure 3.7 for an example, the situation is similar at lower energies). Its energy is however somewhat higher, typically 1.1 MeV for an initial energy of 8 MeV (once more the final energy decreases when the initial energy decreases). The ${}^6\text{Li}$ will eventually breakup into $\alpha+d$, distributing its energy over the two particles. Because of the smaller scattering angles, the particles reside longer in the masked area. Calculations with SRIM show that in this case the energy is not sufficient to escape the masked area. Then, no vertex position can be determined such that a calculation of the Q -value is no longer possible. The situation for detection by the Maya detectors is somewhat different. When inelastic scattering occurs, angular range

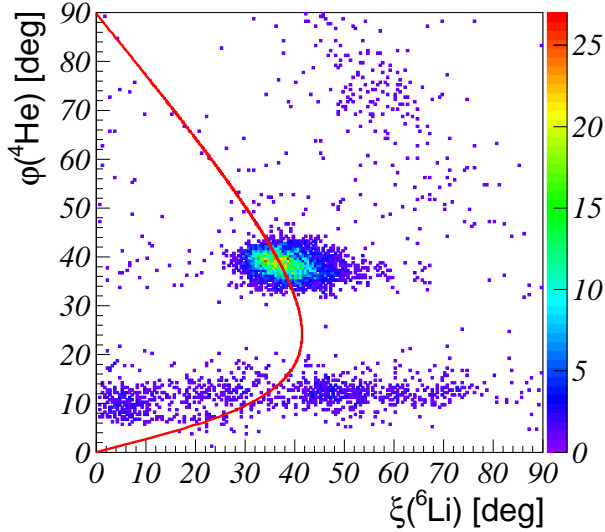


Figure 4.14: Angular correlation plot for all runs with a beam energy of 11.5 MeV. The red line shows the theoretically predicted correlation for elastic scattering. The large number of point at intermediate angles are due to particles identified by the Maya detectors. Particles detected in the DSSDs are found at forward angles, below about 20° .

of the α particle decreases (see 3.7 for an example) with decreasing energy. Eventually it becomes so small that from the geometry of the detector, the Maya detectors are no longer reachable.

It can be seen that in both cases the peak is not found at exactly 0 MeV, but is shifted by a few hundred keV in the negative Q -value range. The angular correlation plot for this energy can been seen in Figure 4.14. Inspecting this plot shows that not a lot events nicely follow the theoretically predicted line when the α particle scatters at forward angles. This is likely due to the very short tracks of the scattered ${}^6\text{Li}$. The result is that the vertex position is either over- or underestimated for over- and underestimated scattering angles respectively. The overall shift towards lower Q -values can partially be explained by an overestimation of the vertex position. A tail on the right hand side of the peak can also be observed. These values can be explained through the underestimation of the vertex position. In order to verify this, attempt was made to correct for the over- and underestimation of the vertex positions. This can be done by using trigonometric relations and comparing the fitted angles with the theoretically expected angles. One should note that this is only a very rough type of correction. The result is given by the red histogram in Figure 4.13(a). It can be seen that the ground state peak is more symmetric. The overall shift of the peak is about 50 keV less and the resolution is somewhat better. These results suggest that the given explanation is appropriate. However, it is clear that other effects still induce an overall shift of about 400 keV. This shift might partially due to the uncertainty of the gas composition. Still, other effects must be present since the amount of He in the gas would have to be unreasonably low (less than 3%) to explain the shift completely. The shift of the peak observed in Figure 4.13(b) can not at all be explained by the over- or underestimation of the vertex. Revisiting Figure 4.14, it can be seen that the measured angular correlation for the particles detected by the Maya

detectors is more or less in agreement with theoretical predictions. There is some spread on the value of the ${}^6\text{Li}$ scattering angles which degrades the resolution of the peak. It is not clear which effect induces the shift. Once more it is unreasonable that the uncertainty on the gas composition can explain the effect fully. Inspection of the individual track do not suggest that something consistently goes wrong with the fitting procedure. Once more, simulations might help to resolve this problem.

4.5.2 The 16.5 MeV beam energy

In Figures 4.15(a) and 4.15(b) the ${}^6\text{Li}$ excitation spectra can be seen for the runs with a beam energy of 16.5 MeV. Figure 4.15(a) corresponds to events in which the identified particle is detected by the DSSDs. It can be seen that two peaks appear, more or less at the expected energies. Any offset from the correct energies can be explained by the uncertainty on the gas composition. As explained in Section 3.3, the angular correlation seems to be better for the particles detected by the DSSDs. So no shift is expected as described in the previous section. It can be seen that the elastic peak is almost completely due to detected ${}^6\text{Li}$ nuclei. Events in which α particles are detected are suppressed in the elastic peak because the forward scattering of α results in low energies for the ${}^6\text{Li}$ (see Figure 3.6(a)). Similar as in the previous section, SRIM calculation suggest that these energies might be too low in some cases such that the ${}^6\text{Li}$ can not escape the mask. On the other hand, the inelastic peak is essentially completely due to detection of α particles. This is expected since ${}^6\text{Li}$ experiences a breakup. Near the peak of the first exited state a significant amount of background counts can be observed. This background is once more due to the presence of breakup α particles.

Figure 4.15(b) shows a completely behavior of the spectrum. The peak related to the ground and first excited states can longer be found at the expected energies. It can be seen that the inelastic peak is essentially completely due to α particles detected in the left Maya detector. This can be explained by the offset of the alignment. A few degrees is enough to make the typical distance between the vertex position and the Maya detectors longer by several millimeters. Additionally, the typical scattering angle has to be larger in order to be able to reach the detectors from a geometrical point of view. Kinematically, it is expected that the energy of the α particle decreases with increasing angle. The combination of these two features has the result that the α particle is stopped right before the detectors. Following this reasoning, it is expected that the first excited state becomes observable via particles detected in the right Maya detector once the beam energy increases. This is indeed the case.

From Figure 4.15(b) it is clear that the particles detected in the right Maya detectors result in a peak at the expected Q -value of 0 MeV. In contrast, the ground state peak for particles detected in the left Maya detectors is found at around -0.8 MeV. This offset is similar to the one observed in Figure 4.13(b). So at first glance, it seems that the same problem could be present in both cases. However, as discussed in Section 4.4 a clear offset of the angles could be observed in the angular correlation plot. This is not observed in the case discussed in the previous section. Additionally, it seems that there is a slight increase in counts at around 0 MeV, indicating that that some event can still be treated correctly. Inspection of the individual vertex positions indicated that the events for which the Q -value is shifted, are typically found at larger vertex positions compared to the events with a Q -value close to 0. This suggests that the vertex position and thus the

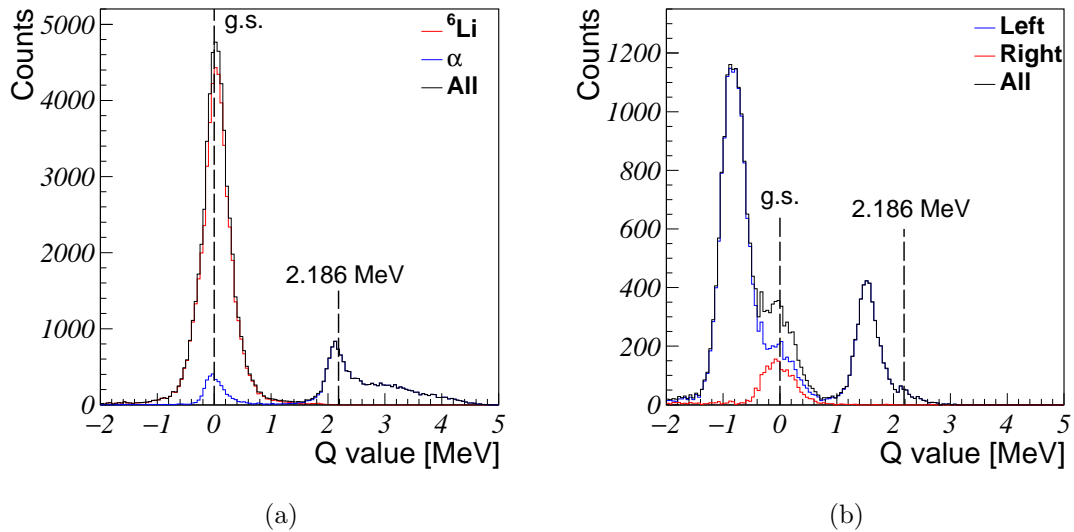


Figure 4.15: The ${}^6\text{Li}$ excitation spectra for (a) particles identified by the DSSDs and (b) particles identified by the Maya detectors. In figure (a), the red histogram indicates the counts in which the particle is identified as ${}^6\text{Li}$ and the blue histogram the counts in which it is identified as an α particle. The black line shows the total amount of counts. In figure (b), the red and blue histograms indicate the particles detected in the left and right Maya detectors respectively. The black line once more shows the total amount of counts. The dashed lines indicate the energies at which the groundstate (0 MeV) and first excited state (2.186 MeV) are expected to be found [28].

angles of the shifted events might be overestimated. This would be in agreement with the offset observed in Figure 4.11. The observed set of points at intermediate angles would move (perpendicular to the x -axis) towards lower angles. Still, inspection of the individual tracks does not suggest in any way that the angles are overestimated. No clear conclusions can be made on this matter until comparisons have been made with simulations.

4.6 The excitation spectrum of ${}^{10}\text{B}$

This section will present the excitation spectrum of ${}^{10}\text{B}$. These spectra can be created by considering the vertex position of each individual reaction. Via SRIM calculations the distance between the entrance window and the vertex position can be converted into an energy loss. Hence, the energy of the ${}^6\text{Li}$ nucleus can be found at this position. If a compound nucleus reaction occurs, the energy of ${}^{10}\text{B}$ can be calculated by Equation (3.30). In the present case, the threshold energy for the ${}^6\text{Li} + \alpha$ reaction is 4.4610 MeV (see also Figure 1.14) [28]. The conversion of the ${}^6\text{Li}$ to the center of mass energy can be done via Equation (3.53). In practice, the lab energy has to be multiplied by a factor ≈ 0.4 .

In the following, the results based on the two same beam energies as discussed in Section 4.5 will be presented. Each time the excitation spectra will be discussed for particles detected in the DSSDs and Maya detectors separately. Additionally, the distinction will be made between elastic and inelastic scattering events. This distinction is made

by gating on the peak of the ground state and first excited state of the ${}^6\text{Li}$ excitation spectra. This is done to point out some differences between the results. Figures related to the other beam energies can be found in Appendix A.2. The 11.5 MeV beam energy is interesting as it covers excitation energies below 8.5 MeV. Potentially energies can be reached which already have been covered in ${}^6\text{Li} + \alpha$ scattering studies in the past. This is useful to make comparisons. Moreover, more information on the 7.002 MeV state might be gained. Revisiting Figure 1.15 on page 1.15 shows that this is an interesting excitation energy in terms of cluster states of ${}^{10}\text{B}$. The 16.5 MeV beam energy is interesting because it covers excitation energies ranging between 8.1 and 10.6 MeV⁸. Revisiting Figure 1.15 shows that in this energy range band members might be expected slightly below a few hundred keV below and above 10 and 8 MeV respectively.

4.6.1 The 11.5 MeV beam energy

As no peak related to inelastic events could be observed for this beam energy, the ${}^{10}\text{B}$ excitation spectra only include elastic events. The results can be seen in Figures 4.16(a) and 4.16(b) for particles detected in the DSSDs and Maya detectors respectively. It is immediately clear that the two spectra are quite different. The result based on the DSSDs shows that there is an overall decrease in counts going towards higher excitation energies. This effect is explained by geometrical effects. If the reaction occurs farther away from DSSDs, the scattering angle of the detected particle must be smaller in order to reach the silicon detectors. Going towards lower excitation energies, the vertex position moves deeper into the gas chamber. This results in a larger range of scattering angles which can be measured, increasing the total number of counts. Additionally, it can be seen in Figure 3.7 that scattering angle of ${}^6\text{Li}$ can potentially be quite large when the α scatters at forward angles. In that case, even when the scattering occurs quite close to the padplane, the ${}^6\text{Li}$ track might not be observed such that those events are lost because no vertex position can be found. Below energy of about 6.7 MeV, there is a sharp decrease in the number of counts. The events corresponding to lower energies can not be used because either both reaction products do no longer have enough energy to reach any of the DSSDs or because the energy of the ${}^6\text{Li}$ becomes too low such that it cannot escape the masked area.

Similarly, geometrical effects also influence the ${}^{10}\text{B}$ spectrum for particles detected by the Maya detectors. In that case the angular range stays more or less the same for all vertices in the area of the padplane. However since now the scattering angles are always quite large (see Figure 4.14), most events with a vertex position found before the padplane are lost. Once more there is not the possibility to observe the tracks of the particles properly. This behavior is reflected in Figure 4.16(b). Almost no counts registered at the higher excitation energies, until about 8 MeV. On the other hand, starting from the lowest excitation energies, it can be seen that only events can be treated starting from an excitation energy of about 7.25 MeV. At lower excitation energies, the no particle can be detected because they both have an energy which is to low to reach the detectors. The start of the spectrum lies at an higher energy compared to the previous case. This is because the energy of the scattered the α particle decreases with the scattering angle. It is clear that geometrical effects together with the energy loss influence the detection

⁸The lower bound of this range was calculated by assuming that vertex positions can be found up to the end of the padplane.

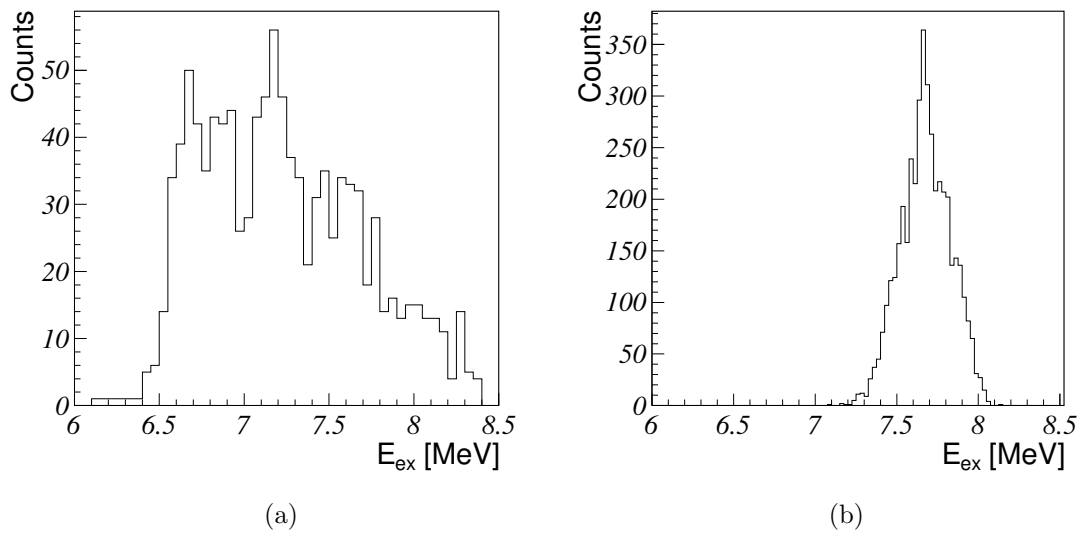


Figure 4.16: The ^{10}B excitation spectra for (a) particles identified by the DSSDs and (c) particles identified by the Maya detectors.

efficiency. Similar effects are observed at all beam energies. This makes a quantitative interpretation of the spectra difficult. In order to make definitive conclusions, the efficiency as a function of the vertex positions in the gas chamber should be estimated such that the spectra can be corrected for these effects. Such an estimation has to be done by simulating the results. This is out of the scope of this thesis. Nevertheless, the spectra might show indications of real resonances.

The compilation by Tilley *et al.* [21] suggests that a lot of excited states of ^{10}B are present in the considered range of excitation energies. For a complete list of all references quoting these states, the reader is referred to this publication and reference therein. Figure 4.16(a) shows that a first peak might be present at an energy of 6.67 MeV. A close-by state at 6.56 MeV was reported by Meyer *et al.* who studied ^{10}B through elastic (α, α) scattering [91]. The same resonance was found through the same reaction in a study by Balakrishnan *et al.* [59]. The width of the state was determined to be about 26 ± 3 keV. Auwärter *et al.* reported another nearby state at 6.88 MeV through the $^6\text{Li}(\alpha, \gamma)^{10}\text{B}$ reaction [92]. Sierk *et al.* reported the same state at an energy of 8.89 MeV [93]. Young *et al.* reported the same two state in a study of the $^{11}\text{B}(^3\text{He}, \alpha)^{10}\text{B}$ reaction with the subsequent emission of an α particle [60]. It also reports a state at 6.67 MeV. However, this state has not been reported in other studies.

A second peak seems to appear at an energy of 6.86 MeV. This peak could be related to the already mentioned state at 6.87 MeV. However, if the peak at 6.67 MeV is shifted downward in energy. The present peak is likely too. Then, the most likely candidate is the state at 7.002 MeV [21]. This state was observed in the the studies of References [59] and [60]. Furthermore the state was observed by Oelert *et al.* in nucleon pick-up studies [61]. The next peak appears at about 7.17 MeV. Following the reasoning of before, this peak could be shifted downward in energy. The closest candidates are states at 7.430 MeV, 7.469 MeV and 7.480 MeV [21]. These states have been reported by Reference [92] and in studies of the (p, d) and (p, p) reactions on ^9Be by Hornyak *et al.* [94] and Mo *et*

al. [95] respectively. Since the shift is quite a bit larger compared to the previous cases, it seems unlikely that the 7.17 MeV really corresponds to either of the two states. It should also be noted that according to the study of Mo *et al.*, the partial α decay widths of the 7.469 MeV and 7.480 MeV states are almost 0 and smaller than 0.1 respectively.

At around 7.45, 7.62 and 7.77 MeV three more peak-like features are seen. The first peak could then be related to one of the three states between 7.4 and 7.5 MeV discussed above. Considering the small α decay widths of the highest states suggest that the 7.430 MeV state might be the most likely. However, if the other peaks have been shifted from their correct energies, it is expected that this peak would also be shifted. A candidate in this case would be a state at 7.56 MeV [95]. It has been deduced however that the partial width for proton decay is essentially 1 such that it is unlikely that this state can be populated through the reaction considered in the present study. Moreover, the isospin of the state is 1, which would also make it harder to populate the state since the isospin of the groundstates of both ${}^6\text{Li}$ and ${}^4\text{He}$ are 0. The same reference also suggests a state at 7.67 MeV with isospin 0. The study suggested that the state has a non-negligible α decay width. In order to reach this state, a large shift in energy is required which makes the relation to this state doubtful. Instead, the second peak might be related to the a state at 7.67 MeV. The 7.77 MeV peak could correspond to a state around 7.75 MeV. This state was found by Mozer *et al.* found the state at 7.77 MeV in (p, p) reaction studies on ${}^9\text{Be}$ [96]. References [94] and [95] found the state at 7.75 and 7.79 MeV respectively. In a (p, d) reaction study by Weber *et al.* the state was found at an energy of 7.71 MeV [97]. Theoretical studies suggest that the state has a non negligible α decay width [21]. Once more, it might be that the observed peak has to be shifted to higher energies. Then a state at 7.96 MeV reported by Leask *et al.* who performed breakup measurements of ${}^{10}\text{B}$ might be a candidate [98]. However, the study suggests that this state can only be populated through inelastic scattering such that the first excited state of ${}^6\text{Li}$ is populated. A last peak is observed at an energy of 8.25 MeV. However, no states near this energy have been reported in the literature.

The spectrum based on the particles observed in the Maya detectors as seen in Figure 4.13(b) shows only one broad feature. Due to the problems with the efficiency with the detector, it is difficult to determine whether the observed peak is a real resonance or not. The maximum is found at an energy of 7.67 MeV. A peak at this energy was also found in the spectrum discussed above. Based on the fact that some peaks might have been shifted towards lower energies in that spectrum, it could be that a similar shift is present in the spectrum of Figure 4.13(b).

It is clear that while it is possible to associate some of the observed peaks with known resonances reported in the literature, it is nearly impossible to associate them all at once. It could be that the shifts in the vertex position discussed in Section 4.5.1 shift the actual excitation energies in such a way that fake peaks are created.

Results after vertex correction

Similar as in Section 4.5.1 one could try to correct the ${}^{10}\text{B}$ excitation spectrum. This way it might become possible to observe peaks which can more consistently be related to the states reported in the literature. It should be stressed once more that this the used procedure can only correct the spectrum in a rough way.

The result is shown in Figure 4.17. It can be seen that less peaks are present. A first

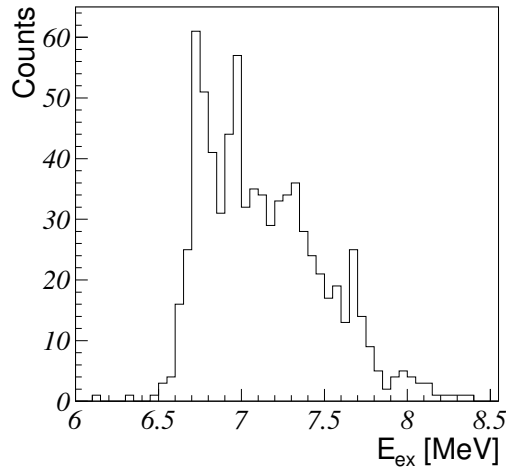


Figure 4.17: Correction of the spectrum in Figure 4.16(a). The same procedure was used as in the correction of Figure 4.13(a).

peak appears at an energy of 6.76 MeV. This could be the 6.87 MeV state reported by References [60, 92, 93]. The second peak appears at around 6.94 MeV. If the peak at 6.76 MeV really is shifted to lower energies, it is expected that this is also be the case for the 6.94 MeV peak. Then, it might be related to the 7.002 MeV state reported by References [59–61]. A small feature seems to appear at 7.1 MeV. Following the shift of the previous two peaks, this state does not seem to correspond to any resonance reported in the literature. Another feature appears at an energy of 7.3 MeV. No state has previously been reported at this energy. Using a shift comparable to the ones used for the previous peaks, the peak might be related to the state at 7.43 MeV reported by references [92, 94]. A rather strong peak is observed at 7.67 MeV. This state could be related to the state at 7.75 MeV reported by References [94–97]. It is interesting that this peak is found exactly at the maximum of the spectrum shown in Figure 4.13(b). This could be an indication that the observed peak in that spectrum might be a real resonance rather than a peak created by the efficiency problems. A last small feature can be seen at an energy of 7.97 MeV. This feature could not be seen in the spectrum of Figure 4.16(a). The energy lies close to the state at 7.96 MeV reported in Reference [98]. However, as mentioned before, it is unlikely that this state is populated through elastic scattering. Another state can be found at an energy of 8.07 MeV. The state is reported in Reference [98]. The study suggests a very broad width of about 800 keV. A shift in the energy could relate the observed peak to this state.

Overall, it seems that almost all peaks can be explained by a shift of roughly 100 keV. Only the peak at 6.94 MeV seems to be shifted somewhat less. Such a shift can be explained by the uncertainty of the gas composition. Overall, the agreement of this spectrum with the literature is reasonably good.

4.6.2 The 16.5 MeV beam energy

Figures 4.18(a) and 4.18(b) show the ^{10}B excitation spectra for particles detected by the DSSDs and Maya detectors respectively. It can be seen that the spectra are quite

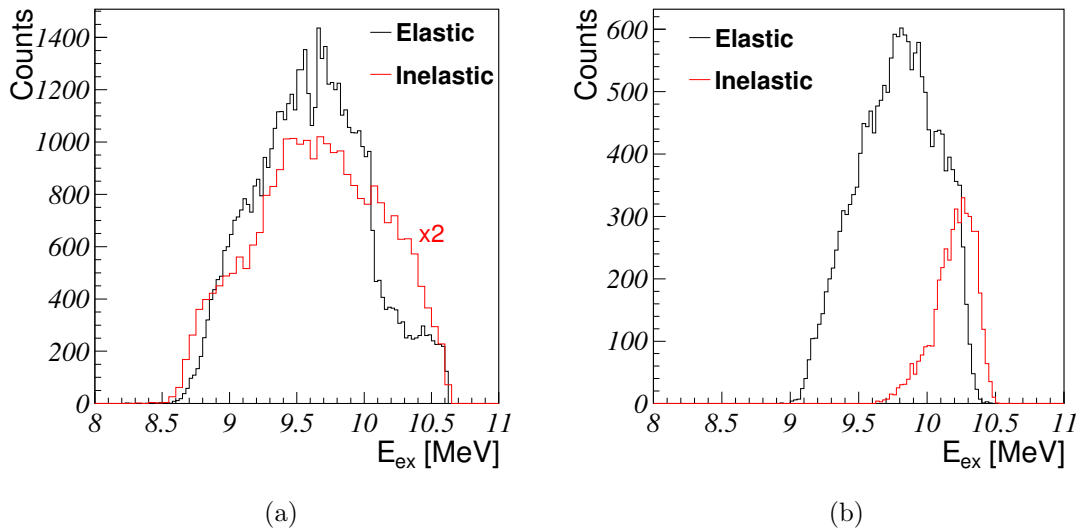


Figure 4.18: The ^{10}B excitation spectra for (a) particles identified by the DSSDs and (b) particles identified by the Maya detectors. The black histogram indicates the elastic events, the red histogram the inelastic events. In Figure (a), the red histogram was magnified three times for clarity.

different. Once more this is due to the efficiency issues related to the geometry and reaction kinematics. At high excitation energies, the spectrum based on the elastic events detected in the DSSDs shows a roughly constant number of counts. Then, at around 10 MeV, a sharp increase can be seen. This sharp increase coincides with the start of the padplane. Revisiting Figure 4.11, it can be understood that again the number of detected events is suppressed before the start of the padplane because the tracks of particles scattered at large angles can not be detected. At energies lower than 9.5 MeV, a decrease counts is observed. Compared to the spectra discussed in Section 4.6.1, this decrease is less sharp. Geometrically, it is expected that particles with a larger scattering angle can be detected if the scattering occurs deeper into the gas chamber. On the other hand, from the kinematics it is known that if the nuclei scatter at larger angles, they have less kinetic energy. Consequently, deeper into the chamber, the detection of particles scattered at smaller angles becomes more favorable. A competition between the two effects explains the slower decrease in counts towards smaller excitation energies. At excitation energies below the lowest observed energy, there might still be particles which could in principle still reach the DSSDs. However, the vertices of these events cannot be used when the tracks start in the area defined for the $\Delta E-E$ plots (revisit Figure 4.7). This way, the starting point of the spectrum is moved to higher energies.

Looking at the inelastic events for particles detected by the DSSDs, it can be seen that there is no longer a sharp increase around 10 MeV. Rather, the increase is slower. For inelastic scattering, the scattering angles for both particles are smaller such that are more easily detected if the scattering occurs before the padplane. The overall increase in this energy range is once more due to the geometrical effects discussed before. The overall decrease towards the lower excitation energies can also be explained by the competition between the geometrical and kinematic effects. Around an energy of 9 MeV, the decrease

suddenly seems to become less. This might be due to a resonance and will be discussed below.

The particles detected in the Maya detectors typically have scattering angles between 30° and 55° . These angles are smaller than the typical scattering angle of the α particle when an elastic reaction occurs and the ${}^6\text{Li}$ scatters at forward angles (see Figure 4.11). The consequence is that events with a vertex position which is less than about 20 mm into the chamber can not be observed. On the other hand, the limitation in the detection efficiency due to the position of the padplane is less severe compared to the events detected by the DSSDs. The result is that the maximally observed energy is somewhat less than in the previously discussed cases, but there is an immediate rise in efficiency towards lower energies. The minimally observed energy is also higher than before. This is because when the particles scatter with larger angles, they have less energy. Hence, the maximally observed vertex position is smaller than before. The other efficiency related aspects of the plot are similar as before.

The last spectrum, related to the inelastic events for particles detected in the Maya detectors looks has a significantly higher minimal observed energy. The maximal vertex position is smaller because the particles have about 2 MeV less kinetic energy. The other efficiency related aspects are similar as before. Because of the severe efficiency issues, not a lot of useful information can be extracted from the spectrum. Therefore, this spectrum will not be discussed in detail. It can be expected that the efficiency issues specific to this case will become less severe for higher beam energies.

In all of the spectra it is clear that the structure is less rich compared to the case discussed in Section 4.6.1. Two peaks at around 9.55 and 9.70 MeV can be seen in the spectrum related to the elastic events detected by the DSSDs. The two peaks are also observed in the inelastic case. However, the 9.55 MeV peak seems to have shifted about 50 keV. Two papers by Marion *et al.* [99, 100] report the study of the (p, n) reaction. In these studies evidence was found for a broad resonance (several hundred keV) near energies of 9.5 and 9.7 MeV. The state was found at 9.7 MeV by Gibbons *et al.* via the same reaction [101]. Reference [100] reports also the $(p, \alpha\gamma)$ reaction on the same target. Once more the state was observed at 9.7 MeV. The latter reaction suggest a non negligible α decay width for the state. The peak at 9.70 MeV observed in the present case might be related to the state reported in those studies. Reference [98] reported a state at 9.58 MeV which could be related to the second peak observed in the two spectra. In that study, the state was only observed through the $\alpha + {}^6\text{Li}(3^+)$ decay channel. The authors also argue that the state is strongly related to the inherent structure to ${}^{10}\text{B}$ which makes the populations of the state through the reaction considered in this thesis unlikely. The spectrum related to the inelastic events show next to the two peaks an elevation of the number of counts near 8.9 MeV which can not easily be explained by the efficiency issues. In this region, a doublet of states at 8.889 and 8.894 MeV has been found [21]. The former state has been reported in the studies of References [98, 100, 101]. Additionally, the state was observed by Kiss *et al.* through the $(p, \alpha\gamma)$ reaction on ${}^9\text{Be}$. The latter state was also reported in Reference [98, 102]. It should be noted however that both states have an isospin $T = 1$. Because of this, it is not likely that the states can be populated through elastic scattering or inelastic scattering to the first excited state of ${}^6\text{Li}$. Based on the spectrum alone, it is thus not clear whether really a resonance is present. At an energy of about 10.07 MeV a small peak seems to be present. Only Reference [98] reported a resonance nearby, around 10.14 MeV. In that study, the state could however not be confirmed definitively.

The spectrum related to the elastic events detected by the Maya detectors shows a broad peak near 9.8 MeV. Additionally a peak at 9.93 MeV might be present. These two peaks could be the same as observed in the other two spectra. If this is the case, the peaks are somehow shifted to larger excitation energies. It is unlikely that the shift is due to the uncertainty in the gas composition. In that case, shifts in the other spectra would also be expected. Moreover, larger shifts in the ${}^6\text{Li}$ excitation spectra would be expected (see Figure 4.15(a)). A clear explanation for the shift could not be found. A small peak at around 10.08 MeV might be present. If this is a real peak, it is likely the same one observed at 10.07 MeV in the previously discussed spectrum.

Chapter 5

Conclusion

In the summer of 2015 there was an experiment in which the ${}^6\text{Li} + \alpha$ reaction in inverse kinematics was studied. This experiment used a prototype detector, ACTAR TPC. The goal of this experiment was to gain more information about the possible cluster nature of ${}^{10}\text{B}$. This thesis concerned the analysis of the data from this experiment. The scope was however limited to the reconstruction of the ${}^{10}\text{B}$ excitation spectrum. No definitive answer about the cluster nature of the nucleus could be given.

The experiment was done at six different beam energies, namely 11.5, 14, 16.5, 19, 21 and 23 MeV. Several slits and the magnetic spectrometer Bacchus [67] have been used to reduce the beam intensity. The ACTAR TPC demonstrator was filled with a 95:5 He:CO₂ gas mixture. The helium content of the gas mixture served as the reaction target. The gas as a whole could be used or the detection of particle tracks. These tracks resulted in information about the reaction kinematics. Additional silicon detectors were installed on the sides of the gas chamber such that particles leaving the gas medium could be detected.

The data analysis consisted of several steps. The first step was the calibration of the detector setup. In total 2316 electronic channels had to be calibrated separately. In the case of the silicon detectors a true energy calibration has been done. There was the need to use a function which could deal with the low-energy background of measured peaks of the calibration source [87, 88]. In the case of the pads of the MICROMESH, only an alignment of the gains was done. The resolution of the strips on the backside of the DSSDs seemed to be worse compared to the strips on the front side. Differences between the four DSSDs were also observed. The Maya detectors on the right side of the chamber showed to have an overall better resolution compared to those on the left side.

The fitting of the tracks involved the iteration over all separate pads of the MICROMESH. When multiple tracks were present on one side of the detector, they could easily be treated as long as they do not emerge from more or less the same vertex position. If this was not the case, special treatments had to be used. These treatments involved the comparison of the timing characteristics and the charge profile of the multiple tracks. Technical problems limited the quality of the fits of the tracks. In some cases some of the pads did not record the charge correctly. Also, stray fields from the silicon detectors disturbed the tracks in some areas of the padplane. The new detector design should take account of these problems and deal with them in a proper way.

Based on the measured energy in the silicon detectors and the collected charge from the pads, $\Delta E - E$ plots could be constructed. The ${}^6\text{Li}$ and α particles have been identified via both the DSSDs and the Maya detectors. Due to problems with the charge collection,

especially in the left halve of the detector, the quality of the plots based on the DSSDs was degraded. For these silicon detectors, the line of the deuterons was obscured and no identification of these particles was possible. The identification of the deuterons was however possible with the Maya detectors. In this case the problems with the charge collection were less severe. Other problems were present however. An additional masked area caused a doubling of the line related to the α particles detected by the right Maya detectors. Problems were observed in the detection signals of the left Maya detectors. The result of this is that specific energy ranges could not properly be treated. In the final detector design, these problems should be treated such that more events can be recovered, increasing the statistics in the subsequent analysis steps.

Reconstruction of the kinematics has shown that for particles detected by the DSSDs, agreement is found with the theoretical results. This agreement is less good in the case of particles detected by the Maya detectors. The angles seemed to be overestimated consistently. No evidence was found of this when individual tracks were analyzed. A definitive explanation of this behavior could thus not be found.

The ${}^6\text{Li}$ excitation spectra for two beam energies, 11.5 and 16.5 MeV have been discussed in detail. In the former case, only elastic events could be recovered. The spectra based on particles detected by the DSSDs showed an asymmetry of the peak related to the groundstate. An explanation was found in the inconsistent quality of the fitting procedure of the short ${}^6\text{Li}$ tracks. An attempt to correct for this, resulted in a peak for which the symmetry was regained. For both this spectrum and the one related to particles identified by the Maya detectors showed a shift towards lower energies. The uncertainty of the gas mixture could not explain this effect. The spectra for the 16.5 MeV beam energy showed two peaks related to the ground and first excited states of ${}^6\text{Li}$. In the case of the DSSDs the peaks were found at the correct energies. A background related to the breakup α particles was present. In the case of the Right Maya detectors only the ground state peak was observed, at the correct energy. In the case of the left Maya detectors, most events resulted in a shifted Q -value towards lower energies. This is due to the consistent overestimation of the scattering angle. The ability to reconstruct the ${}^6\text{Li}$ for most beam energies serves as a proof-of-principle for the detector.

The ${}^{10}\text{B}$ excitation spectrum was reconstructed for the 11.5 and 16.5 beam energies. All spectra showed significant efficiency issues related to the geometry and kinematics of the reaction. For the 11.5 MeV beam energy, multiple peaks could be observed for the spectrum based on the DSSDs. Assignments of the individual peaks was possible, but a coherent assignment for all peaks at once proved difficult. The spectrum was corrected. Peaks were observed at 6.76, 6.94, 7.30, 7.67 and 7.97 MeV. After a global shift of roughly 100 keV, these peaks could be related to known states at 6.87 [60, 92, 93], 7.002 [59–61], 7.43 [92, 94], 7.75 [94–97] and 8.07 [98] MeV. The spectrum based on the Maya detectors only showed a single peak at 7.67 MeV. After a similar shift in energy, this peak can be related to the state at 7.75 MeV. The spectra for the 16.5 MeV beam energy showed less features. Peaks could be observed at 9.55 and 9.70 MeV. The latter peak could be related to the 9.7 MeV state reported by References [99–101]. The 9.55 MeV could be related to a state at 9.58 MeV, although the population of this state should be suppressed [98]. Some indications for states at 8.9 MeV could be found in the inelastic channel. However the population of these states should also be suppressed [21, 98, 100, 102].

Appendix A

Spectra of the other beam energies

In Chapter 4 the ${}^6\text{Li}$ and ${}^{10}\text{B}$ excitation spectra for only two beam energies, 11.5 and 16.5 MeV have been presented and discussed in detail. For completeness, in this appendix the ${}^6\text{Li}$ and ${}^{10}\text{B}$ excitation spectra are given for the beam energies of 14, 19, 21 and 23 MeV. They will however not be discussed in detail.

A.1 The ${}^6\text{Li}$ excitation spectra

Below, the reconstructed ${}^6\text{Li}$ spectra are presented. In case of the spectra created from particles detected by the DSSDs, the histograms recovered from detected ${}^6\text{Li}$ and α particles are shown in red and blue respectively. In case of the spectra created from particles detected by the Maya detectors, all counts come from detected α particles. The histograms based on the left and right Maya detectors are given in blue and red respectively. The histogram in black each time gives the total number of counts.

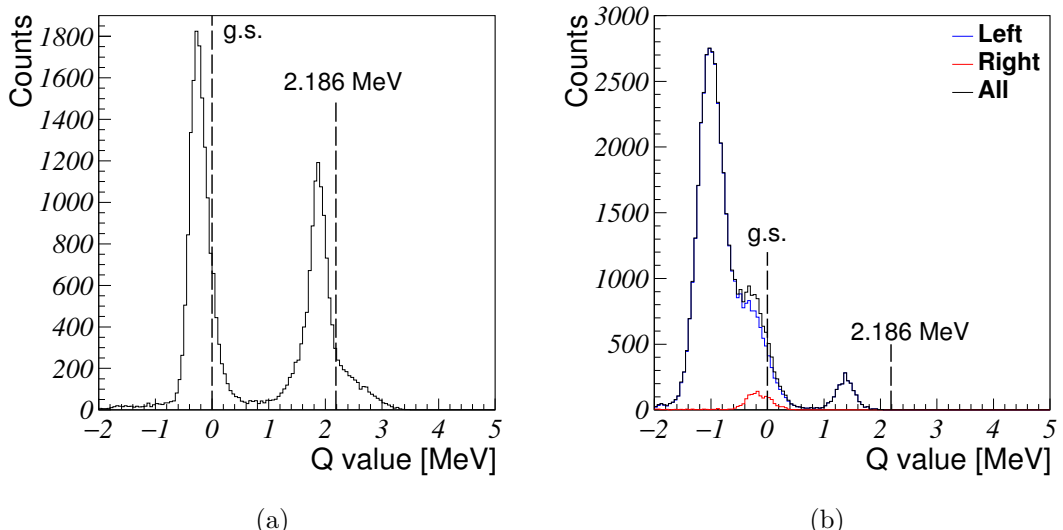


Figure A.1: The ${}^6\text{Li}$ spectra based on the 14 MeV runs. The results based on the DSSDs are shown in (a), the results based on the Maya detectors in (b). Note that for this energy no ${}^6\text{Li}$ nuclei could be detected by the silicon detectors.

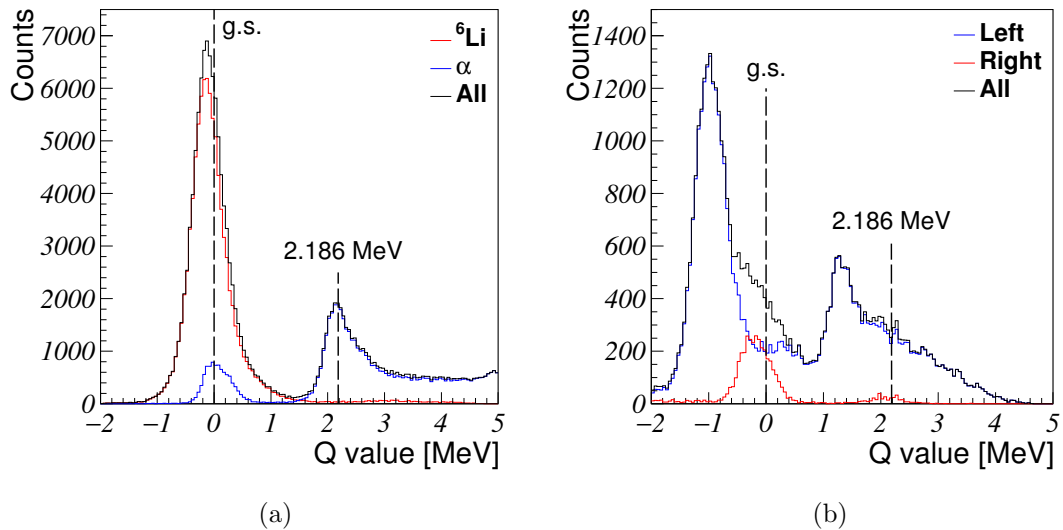


Figure A.2: The ${}^6\text{Li}$ spectra based on the 19 MeV runs. The results based on the DSSDs are shown in (a), the results based on the Maya detectors in (b).

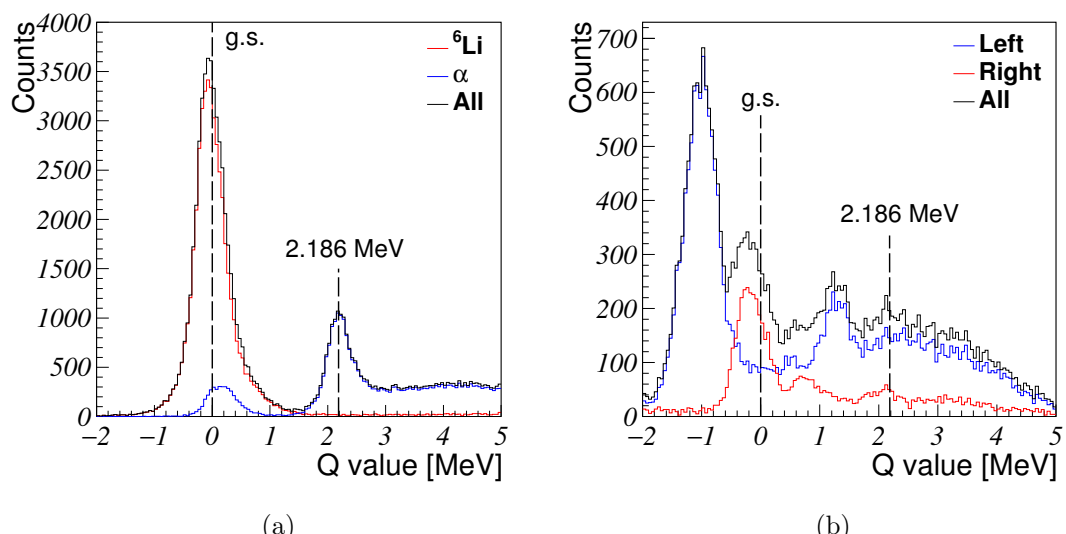


Figure A.3: The ${}^6\text{Li}$ spectra based on the 211 MeV runs. The results based on the DSSDs are shown in (a), the results based on the Maya detectors in (b).

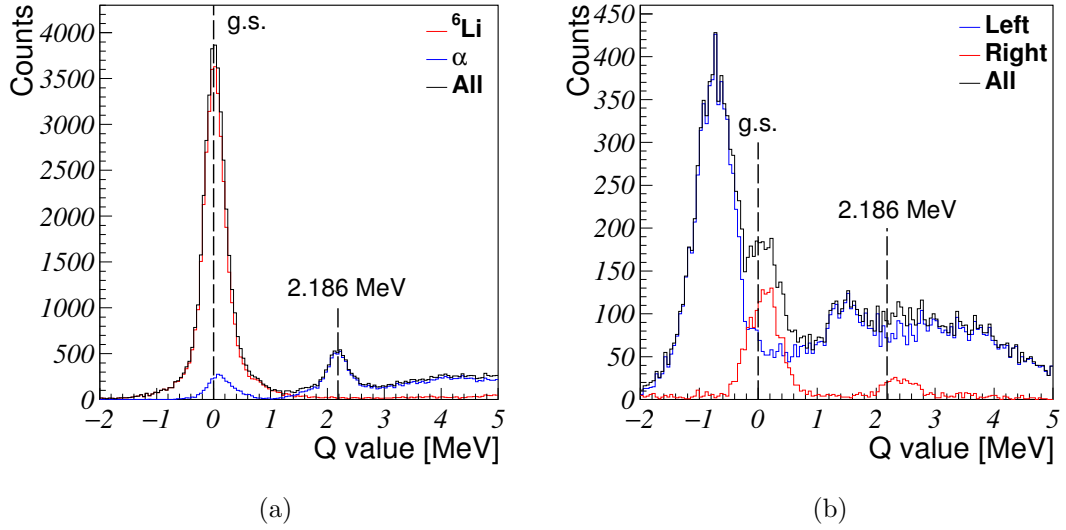


Figure A.4: The ^6Li spectra based on the 23 MeV runs. The results based on the DSSDs are shown in (a), the results based on the Maya detectors in (b).

A.2 The ^{10}B excitation spectra

Below, the reconstructed ^{10}B spectra are presented. In case of the spectra created from particles detected by the DSSDs, the histograms recovered from elastic and inelastic events are shown in black and red respectively. The same color code is used for the particles detected by the Maya detectors.

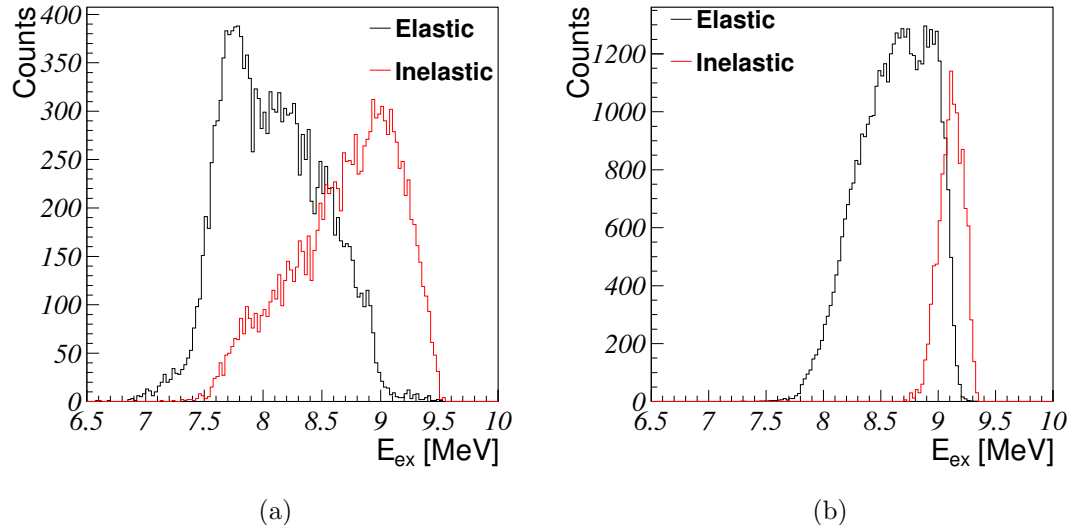


Figure A.5: The ^{10}B spectra based on the 14 MeV runs. The results based on the DSSDs are shown in (a), the results based on the Maya detectors in (b).

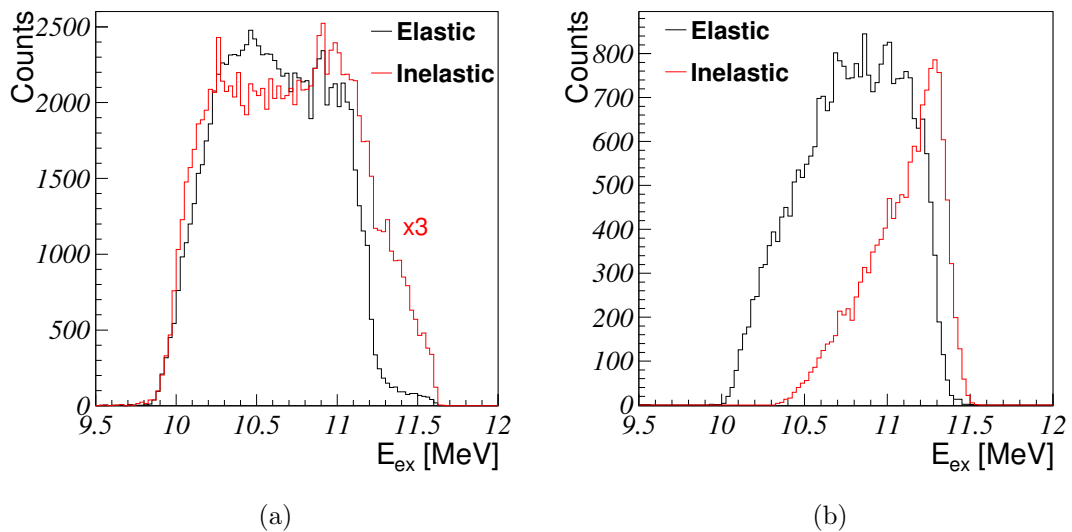


Figure A.6: The ^{10}B spectra based on the 19 MeV runs. The results based on the DSSDs are shown in (a), the results based on the Maya detectors in (b).

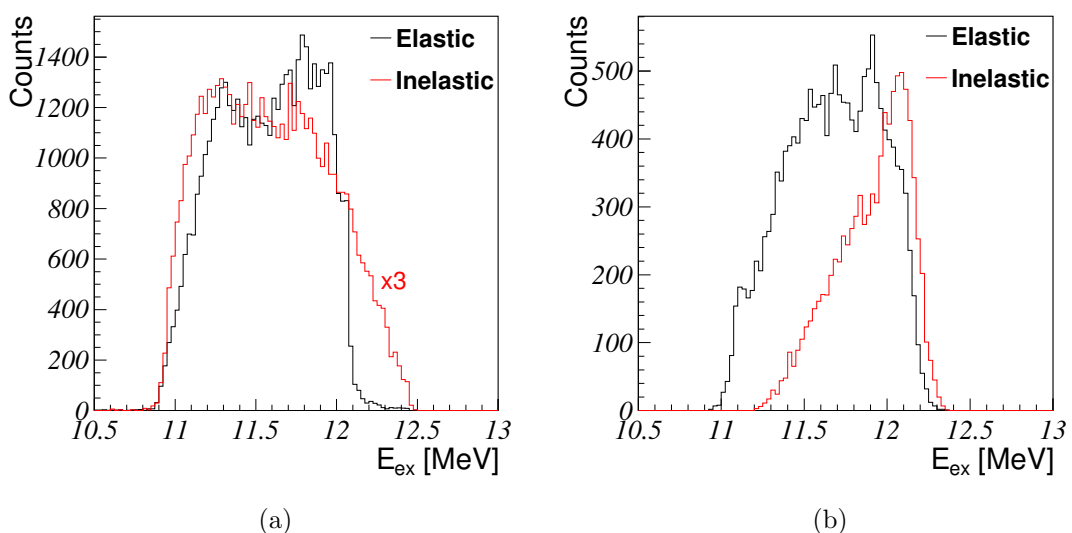


Figure A.7: The ^{10}B spectra based on the 21 MeV runs. The results based on the DSSDs are shown in (a), the results based on the Maya detectors in (b).

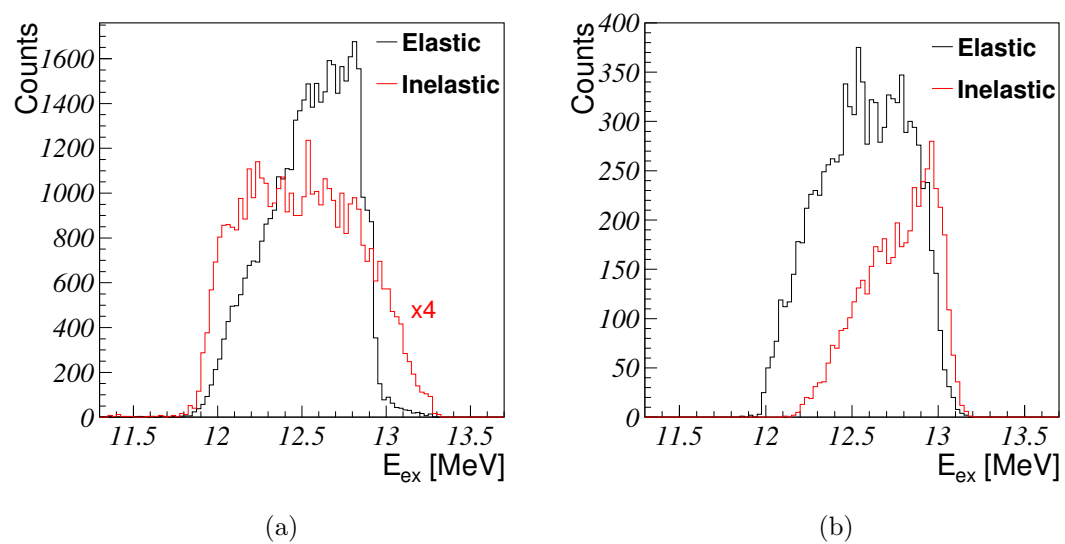


Figure A.8: The ^{10}B spectra based on the 23 MeV runs. The results based on the DSSDs are shown in (a), the results based on the Maya detectors in (b).

Bibliography

1. Erler, J. *et al.* The limits of the nuclear landscape. *Nature* **486**, 509–512 (2012).
2. Krane, K. S. *Introductory Nuclear Physics* (John Wiley & Sons, 1987).
3. Grawe, H. in *The Euroschool Lectures on Physics with Exotic Beams, Vol. I* 33–75 (Springer, 2004).
4. Otsuka, T. Exotic nuclei and nuclear forces. *Physica Scripta* **2013**, 014007 (2013).
5. Mayer, M. G. On Closed Shells in Nuclei. II. *Phys. Rev.* **75**, 1969–1970 (12 1949).
6. Haxel, O. *et al.* On the ‘Magic Numbers’ in Nuclear Structure. *Phys. Rev.* **75**, 1766–1766 (11 1949).
7. Eisenberg, J. M. & Greiner, W. *Nuclear theory* (North-Holland Pub. Co., 1976).
8. Basdevant, J.-L. & Dalibard, J. *Quantum Mechanics* (Springer, 2005).
9. Ragnarsson, I. & Nilsson, S. G. *Shapes and Shells in Nuclear Structure* (Cambridge University Press, 2005).
10. Otsuka, T. *et al.* Evolution of Nuclear Shells due to the Tensor Force. *Physical Review Letters* **95**, 232502 (2005).
11. Steppenbeck, D. *et al.* Evidence for a new nuclear ‘magic number’ from the level structure of ^{54}Ca . *Nature* **502**, 207–10 (2013).
12. Casten, R. *Nuclear Structure from a Simple Perspective* (Oxford University Press, 2000).
13. Caurier, E. *et al.* Intrinsic vs Laboratory Frame Description of the Deformed Nucleus ^{48}Cr . *Physical Review Letters* **75**, 2466–2469 (1995).
14. Nilsson, S. G. Binding states of individual nucleons in strongly deformed nuclei. *Dan. Mat. Fys. Medd.* **29**, 1–69 (1955).
15. Freer, M. The clustered nucleus-cluster structures in stable and unstable nuclei. *Reports on Progress in Physics* **70**, 2149 (2007).
16. Gaffney, L. P. *et al.* Studies of pear-shaped nuclei using accelerated radioactive beams. *Nature* **497**, 199–204 (2013).
17. Lamarsh, J. R. & Baratta, A. J. *Introduction to Nuclear Engineering* (Prentice Hall, 2001).
18. Tilley, D. R. *et al.* Energy levels of light nuclei $A = 4$. *Nuclear Physics A* **541**, 1–104 (1992).
19. Von Oertzen, W. *et al.* Nuclear clusters and nuclear molecules. *Physics Reports* **432**, 43–113 (2006).

20. Hafstad, L. R. & Teller, E. The Alpha-Particle Model of the Nucleus. *Physical Review* **54**, 681–692 (1938).
21. Tilley, D. R. *et al.* Energy levels of light nuclei A=8, 9, 10. *Nuclear Physics A* **745**, 155–362 (2004).
22. Beck, C. *Clusters in Nuclei* (Springer Science & Business Media, 2012).
23. Kanada-En'yo, Y. *et al.* Structures of ground and excited states in C isotopes. *Journal of Physics: Conference Series* **445**, 012037 (2013).
24. Ikeda, K. *et al.* The Systematic Structure-Change into the Molecule-like Structures in the Self-Conjugate 4n Nuclei. *Progress of Theoretical Physics Supplement* **E68**, 464–475 (1968).
25. Ajzenberg-Selove, F. Energy levels of light nuclei A = 11–12. *Nuclear Physics A* **506**, 1–158 (1990).
26. Tilley, D. R. *et al.* Energy levels of light nuclei A = 16–17. *Nuclear Physics A* **564**, 1–183 (1993).
27. Tilley, D. R. *et al.* Energy levels of light nuclei, A = 20. *Nuclear Physics A* **636**, 249–364 (1998).
28. Pritychenko, B. *et al.* The Nuclear Science References (NSR) database and Web Retrieval System. *Nuclear Instruments and Methods in Physics Research Section A: Accelerators, Spectrometers, Detectors and Associated Equipment* **640**, 213–218 (2011).
29. Von Oertzen, W. Nuclear Clusters and Covalently Bound Nuclear Molecules. *Progress of Theoretical Physics Supplement* **146**, 169–178 (2002).
30. Horiuchi, H. *et al.* Recent Developments in Nuclear Cluster Physics. *Progress of Theoretical Physics Supplement* **192**, 1–238 (2012).
31. Hoyle, F. On Nuclear Reactions Occuring in Very Hot Stars. I. The Synthesis of Elements from Carbon to Nickel. *The Astrophysical Journal Supplement Series* **1**, 121 (1954).
32. Morinaga, H. Interpretation of Some of the Excited States of 4n Self-Conjugate Nuclei. *Phys. Rev.* **101**, 254–258 (1956).
33. Saito, S. Chapter II. Theory of Resonating Group Method and Generator Coordinate Method, and Orthogonality Condition Model. *Progress of Theoretical Physics Supplement* **62**, 11–89 (1977).
34. Kawabata, T. *et al.* $2\alpha + t$ cluster structure in ^{11}B . *Physics Letters B* **646**, 6–11 (2007).
35. Freer, M. *et al.* Relationship between the deformed harmonic oscillator and clustering in light nuclei. *Nuclear Physics A* **587**, 36–54 (1995).
36. Rae, W. D. M. Clustering phenomena and shell effects in nuclear structure and reactions. *International Journal of Modern Physics A* **3**, 1343–1372 (1988).
37. Nazarewicz, W. & Dobaczewski, J. Dynamical symmetries, multiclusering, and octupole susceptibility in superdeformed and hyperdeformed nuclei. *Physical review letters* **68**, 154 (1992).

38. Scharnweber, D. *et al.* The two-center shell model. *Nuclear Physics A* **164**, 257–278 (1971).
39. Brink, D. M. & Castro, J. J. Alpha clustering effects in nuclear matter. *Nuclear Physics A* **216**, 109–124 (1973).
40. Freer, M. in *The Euroschool on Exotic Beams, Vol. IV Lecture Notes in Physics* 879, 1–37 (Springer Berlin Heidelberg, 2014).
41. Davis, J. C. The wave mechanics of atoms, molecules, and ions. An introduction for chemistry students (Schutte, C. J. H.) *Journal of Chemical Education* **46**, 502 (1969).
42. Funaki, Y. *et al.* Description of ${}^8\text{Be}$ as Deformed Gas-Like Two-Alpha-Particle States. *Progress of theoretical physics* **108**, 297–322 (2002).
43. Tohsaki, A. *et al.* Alpha Cluster Condensation in ${}^{12}\text{C}$ and ${}^{16}\text{O}$. *Physical Review Letters* **87**, 192501 (2001).
44. Descouvemont, P. & Dufour, M. in *Clusters in Nuclei, Vol.2 Lecture Notes in Physics* 848, 1–66 (Springer Berlin Heidelberg, 2012).
45. Kanada-En'yo, Y. & Horiuchi, H. Structure of Light Unstable Nuclei Studied with Antisymmetrized Molecular Dynamics. *Progress of Theoretical Physics Supplement* **142**, 205–263 (2001).
46. Kanada-En'yo, Y. & Kimura, M. in, 129–164 (Springer Berlin Heidelberg, Berlin, Heidelberg, 2010).
47. Kanada-En'yo, Y. *et al.* Structure of Li and Be isotopes studied with antisymmetrized molecular dynamics. *Physical Review C* **52**, 628 (1995).
48. Rampho, G. J. & Sofianos, S. A. *Antisymmetrized molecular dynamics and nuclear structure* (INTECH Open Access Publisher, 2012).
49. Itagaki, N. & Okabe, S. Molecular orbital structures in ${}^{10}\text{Be}$. *Physical Review C* **61**, 044306 (2000).
50. Kanada-En'yo, Y. *et al.* Structure of excited states of ${}^{10}\text{Be}$ studied with antisymmetrized molecular dynamics. *Physical Review C* **60**, 064304 (1999).
51. Suhara, T. & Kanada-En'yo, Y. Quadrupole Deformation β and γ Constraint in a Framework of Antisymmetrized Molecular Dynamics. *Progress of Theoretical Physics* **123**, 303–325 (2010).
52. Itagaki, N. *et al.* Triaxial deformation in ${}^{10}\text{Be}$. *Physical Review C* **65**, 044302 (2002).
53. Curtis, N *et al.* Decay angular correlations and spectroscopy for ${}^{10}\text{Be}^* \rightarrow {}^4\text{He} + {}^6\text{He}$. *Physical Review C* **64**, 044604 (2001).
54. Freer, M. *et al.* $\alpha:2n:\alpha$ Molecular Band in ${}^{10}\text{Be}$. *Physical Review Letters* **96**, 042501 (2006).
55. Suzuki, D. *et al.* Resonant α scattering of ${}^6\text{He}$: Limits of clustering in ${}^{10}\text{Be}$. *Physical Review C* **87**, 054301 (2013).
56. Nishioka, H. Two-alpha-particle-plus-dinucleon-cluster model for ${}^{10}\text{B}$ and ${}^{10}\text{Be}$. *Journal of Physics G: Nuclear Physics* **10**, 1713 (1984).

57. Fujiwara, Y. & Tang, Y. C. Multiconfiguration Resonating-Group Study of the 10-Nucleon System. *Progress of Theoretical Physics* **93**, 357–372 (1995).
58. Kanada-En'yo, Y. *et al.* Proton and neutron correlations in ^{10}B . *Phys. Rev. C* **91**, 054323 (5 2015).
59. Balakrishnan, M. *et al.* States in ^{10}B from Elastic Scattering of Alphas by ^6Li . *Il Nuovo Cimento A (1965-1970)* **1**, 205–216 (2007).
60. Young, F. C. *et al.* Spin-parity determinations of ^{10}B levels by $^{11}\text{B}(^3\text{He}, \alpha)^{10}\text{B}(\alpha_0)^6\text{Li}$ correlations. *Nuclear Physics A* **176**, 289–298 (1971).
61. Oelert, W. *et al.* Four-nucleon pickup from ^{14}N . *Physical Review C* **19**, 1747 (1979).
62. Ajzenberg-Selove, F. Energy levels of light nuclei A= 5-10. *Nuclear Physics A* **490**, 1–225 (1988).
63. Blieden, H. *et al.* A study of the $\text{Be}^9(p, \alpha)\text{Li}^6$ reaction from 3.5 to 12.5 MeV. *Nuclear Physics* **49**, 209–238 (1963).
64. Raabe, R. *ACTAR: An Active Target detector for the study of extremely exotic nuclei* tech. rep. (GANIL, 2009).
65. Essabaa, S. *et al.* The radioactive beam facility ALTO. *Nuclear Instruments and Methods in Physics Research Section B: Beam Interactions with Materials and Atoms. XVIth International Conference on ElectroMagnetic Isotope Separators and Techniques Related to their Applications, December 2–7, 2012 at Matsue, Japan* **317, Part B**, 218–222 (2013).
66. IPN Orsay. *The ALTO facility* <http://ipnwww.in2p3.fr/Installation-ALTO>, 5. Accessed: 11/04/2016.
67. Roussel, P. *et al.* Reconstitution of heavy ion trajectories on a magnetic spectrometer. *Nuclear Instruments and Methods* **153**, 111–119 (1978).
68. The ACTAR collaboration. *EXP-N-SI78: Search for cluster states in ^{10}B using the ACTAR TPC* Proposal for the experiment.
69. Suzuki, D. *ACTAR-Bacchus campaign round two: ^6Li* . Slides presented right before the experiment.
70. Ziegler, J. F. *et al.* SRIM – The stopping and range of ions in matter (2010). *Nuclear Instruments and Methods in Physics Research Section B: Beam Interactions with Materials and Atoms* **268**, 1818–1823 (2010).
71. Knoll, G. F. *Radiation Detection and Measurement* (John Wiley & Sons, 2010).
72. Demonchy, C. E. *et al.* MAYA: An active-target detector for binary reactions with exotic beams. *Nuclear Instruments and Methods in Physics Research Section A: Accelerators, Spectrometers, Detectors and Associated Equipment* **583**, 341–349 (2007).
73. Giomataris, Y. *et al.* MICROMEGAS: a high-granularity position-sensitive gaseous detector for high particle-flux environments. *Nuclear Instruments and Methods in Physics Research Section A: Accelerators, Spectrometers, Detectors and Associated Equipment* **376**, 29–35 (1996).
74. Leo, W. R. *Techniques for nuclear and particle physics experiments: a how-to approach* (Springer Science & Business Media, 2012).

75. Poenaru, D. N. & Greiner, W. *Experimental techniques in nuclear physics* (Walter de Gruyter, 1997).
76. Takeda, S. *et al.* Double-sided silicon strip detector for x-ray imaging. *SPIE Newsroom* (2008).
77. The ACTAR collaboration. *ACTAR: Conceptual design report* tech. rep. (2012), 53.
78. Pollacco, E. *et al.* GET: A Generic Electronic System for TPCs for Nuclear Physics Experiments. *Physics Procedia. Proceedings of the 2nd International Conference on Technology and Instrumentation in Particle Physics (TIPP 2011)* **37**, 1799–1804 (2012).
79. The ACTAR collaboration. *ACTAR: Electronics report* tech. rep. (2012).
80. Baron, P. & Delagnes, E. *AGET, a Front End ASIC for Active Time Projection Chamber* tech. rep. (2013).
81. Satchler, G. *Introduction to Nuclear Reactions* (Macmillan Press, 1980).
82. Hodgson, P. E. *Nuclear reactions and nuclear structure* (Clarendon Press, 1971).
83. Burcham, W. E. *Nuclear Physics: An Introduction* (McGraw-Hill, 1963).
84. Jackson, D. F. *Nuclear reactions* (Methuen, 1970).
85. Sakurai, J. J. & Napolitano, J. *Modern Quantum Mechanics* (Addison-Wesley, 2011).
86. Breit, G. & Wigner, E. Capture of slow neutrons. *Physical review* **49**, 519 (1936).
87. Bortels, G. & Collaers, P. Analytical function for fitting peaks in alpha-particle spectra from Si detectors. *International Journal of Radiation Applications and Instrumentation. Part A. Applied Radiation and Isotopes* **38**, 831–837 (1987).
88. Pommé, S. & Caro Marroyo, B. Improved peak shape fitting in alpha spectra. *Applied Radiation and Isotopes* **96**, 148–153 (2015).
89. Jacquelin, J. *Regressions et Trajectoires en 3D* 2011. Paper freely available on the web (last viewed 28/04/16): <https://www.scribd.com/doc/31477970/Regressions-et-trajectoires-3D>.
90. Roger, T. *et al.* Tracking algorithms for the active target MAYA. *Nuclear Instruments and Methods in Physics Research Section A: Accelerators, Spectrometers, Detectors and Associated Equipment* **638**, 134–142 (2011).
91. Meyer, V. *et al.* Excited states in ^{10}B from the reaction $^6\text{Li}(\alpha, \alpha)^6\text{Li}$. *Nuclear Physics A* **101**, 321–332 (1967).
92. Auwärter, W. & Meyer, V. Excited states of ^{10}B from the $^6\text{Li}(\alpha, \gamma)$ and $^9\text{Be}(p, \gamma)$ reactions. *Nuclear Physics A* **242**, 129–140 (1975).
93. Sierk, A. J. & Tombrello, T. A. The $^9\text{Be}(p, \alpha)$ and (p, d) cross sections at low energies. *Nuclear Physics A* **210**, 341–354 (1973).
94. Hornyak, W. F. *et al.* Energy levels of B^{10} . *Nuclear Physics* **50**, 424–449 (1964).
95. Mo, T. & Hornyak, W. F. B^{10} Levels from Elastic Scattering of Protons by Be^9 . *Physical Review* **187**, 1220–1233 (1969).

96. Mozer, F. S. Elastic Scattering of Protons by Beryllium. *Physical Review* **104**, 1386–1398 (1956).
97. Weber, G. *et al.* (p, d) and (p, α) Reactions in Be^9 . *Physical Review* **104**, 1307 (1956).
98. Leask, P. J. *et al.* Breakup measurements of particle unbound states in ^{10}B . *Physical Review C* **63** (2001).
99. Marion, J. B. Excited States in B^{10} . *Physical Review* **103**, 713 (1956).
100. Marion, J. B. & Levin, J. S. Investigation of the $\text{Be}^9(p,n)\text{B}^9$ and $\text{Be}^9(p,\alpha\gamma)\text{Li}^6$ Reactions. *Physical Review* **115**, 144 (1959).
101. Gibbons, J. H. & Macklin, R. L. Total neutron yields from light elements under proton and alpha bombardment. *Physical Review* **114**, 571 (1959).
102. Kiss, A. *et al.* Levels of ^{10}B from the $^9\text{Be}(p,\alpha_2\gamma)^6\text{Li}$ and $^9\text{Be}(p,p)^9\text{Be}$ reactions at $E_p = 2.56$ MeV. *Nuclear Physics A* **282**, 44–52 (1977).

DEPARTEMENT NATUURKUNDE EN STERRENKUNDE

Celestijnenlaan 200d bus 2412

3001 HEVERLEE, BELGIË

tel. + 32 16 32 71 24

fys.kuleuven.be

